

The chiral and deconfinement aspects of the QCD transition

A. Bazavov^a, T. Bhattacharya^b, M. Cheng^c, C. DeTar^d, H.-T. Ding^a, Steven Gottlieb^e, R. Gupta^b,
P. Hegde^a, U.M. Heller^f, F. Karsch^{a,g}, E. Laermann^g, L. Levkova^d, S. Mukherjee^a, P. Petreczky^a,
C. Schmidt^{g,h}, R.A. Soltz^c, W. Soeldnerⁱ,
R. Sugar^j, D. Toussaint^k, W. Unger^l and P. Vranas^c

(HotQCD Collaboration)

^a *Physics Department, Brookhaven National Laboratory,
Upton, NY 11973, USA*

^b *Theoretical Division, Los Alamos National Laboratory,
Los Alamos, NM 87545, USA*

^c *Physics Division, Lawrence Livermore National Laboratory,
Livermore CA 94550, USA*

^d *Department of Physics and Astronomy,
University of Utah, Salt Lake City, UT 84112, USA*

^e *Physics Department, Indiana University,
Bloomington, IN 47405, USA*

^f *American Physical Society,
One Research Road, Ridge, NY 11961, USA*

^g *Fakultät für Physik, Universität Bielefeld,
D-33615 Bielefeld, Germany*

^h *Frankfurt Institute for Advanced Studies,
J.W.Goethe Universität Frankfurt,
D-60438 Frankfurt am Main, Germany*

ⁱ *Institut für Theoretische Physik,
Universität Regensburg, D-93040 Regensburg, Germany*

^j *Physics Department, University of California,
Santa Barbara, CA 93106, USA*

^k *Physics Department, University of Arizona,
Tucson, AZ 85721, USA*

^l *Institut für Theoretische Physik,
ETH Zürich, CH-8093 Zürich, Switzerland*

We present results on the chiral and deconfinement properties of the QCD transition at finite temperature. Calculations are performed with $2 + 1$ flavors of quarks using the p4, asqtad and HISQ/tree actions. Lattices with temporal extent $N_\tau = 6, 8$ and 12 are used to understand and control discretization errors and to reliably extrapolate estimates obtained at finite lattice spacings to the continuum limit. The chiral transition temperature is defined in terms of the phase transition in a theory with two massless flavors and analyzed using $O(N)$ scaling fits to the chiral condensate and susceptibility. We find consistent estimates from the HISQ/tree and asqtad actions and our main result is $T_c = 154 \pm 9$ MeV.

November 27, 2024

PACS numbers: 11.15.Ha, 12.38.Gc

I. INTRODUCTION

It was noted even before the advent of Quantum Chromodynamics (QCD) as the underlying theory of strongly interacting elementary particles, that nuclear matter cannot exist as hadrons at an arbitrarily high temperature or density. The existence of a limiting temperature was formulated in the context of the Hagedorn resonance gas model [1]. This phenomenon has been interpreted in the framework of QCD as a phase transition [2] separating ordinary hadronic matter from a new phase of strongly interacting matter — the quark gluon plasma [3]. Today, the structure of the QCD phase diagram and the transition temperature in the presence of two light and a heavier strange quark is being investigated using high precision simulations of lattice QCD.

Understanding the properties of strongly interacting matter at high temperatures has been a central goal of numerical simulations of lattice QCD ever since the first investigations of the phase transition and the equation of state in a purely gluonic SU(2) gauge theory [4–6]. Early work showed that chiral symmetry and its spontaneous breaking at low temperatures play an important role in understanding the phase diagram of strongly interacting matter.

Chiral symmetry breaking introduces a length scale, and the possibility that it may be independent of deconfinement phenomena was discussed [7, 8]. Similarly, the consequences of the existence of an exact global symmetry in the chiral limit of QCD, the spontaneous breaking of this $O(4)$ symmetry, the influence of the explicit breaking of the axial $U_A(1)$ symmetry and the presence of a heavier strange quark for the QCD phase diagram were analyzed [9]. The possibilities that the strange quark mass could be light enough to play a significant role in the QCD transition, and/or an effective restoration of axial symmetry may trigger a first order phase transition in QCD for even nonzero light quark masses were also discussed. Neither of these situations seems to be realized in QCD for physical light and strange quark masses. Based on recent high precision calculations, the QCD transition at nonzero temperature and vanishing chemical potentials is observed to be an analytic crossover [10–12].

In this paper we focus on understanding the universal properties of the QCD phase transition in the chiral limit and extract the behavior of QCD at physical quark masses using an $O(N)$ scaling analysis. We also calculate quantities that probe the deconfinement aspects of the QCD transition: quark number susceptibilities and the renormalized Polyakov loop. It is expected that for temperatures below the transition temperature these quantities should be well described by the hadron resonance gas (HRG) model which is very successful in describing thermodynamics at low temperature and the basic features of the matter produced in relativistic heavy ion collisions [13]. It is, therefore, interesting to quantify the interplay between the universal properties of the chiral transition and the physics of the HRG model. Some of these issues will be addressed in a separate publication.

Investigations of QCD at finite temperature are carried out using a number of different lattice formulations of the Dirac action. While studies based on the Wilson [14, 15] or chiral fermion formulations [16] are, at present, constrained to a regime of moderately light quark masses ($m_l/m_s \gtrsim 0.2$), calculations exploiting staggered fermion discretization schemes [10, 11, 17–24] can be performed with an almost realistic spectrum of dynamical light and strange quarks. Today, high statistics calculations, performed at a number of values of the lattice cutoff and quark masses, allow for a detailed analysis of discretization errors and quark mass effects.

Recent studies of QCD thermodynamics with two degenerate light quarks and the heavier strange quark have been performed with several staggered fermion actions that differ in the way improvements are incorporated to reduce the effects of known sources of discretization errors. These include the asqtad, p4 and stout actions. The results at $a \sim 0.1$ fm show differences not only in the determination of relevant scales, such as the transition temperature, but also in the temperature dependence of thermodynamic observables. Because estimates of all observables ought to agree in the continuum limit, discretization errors and the dependence on light quark masses require careful analysis. Furthermore, since QCD for physical quark masses does not display a genuine phase transition, the definition of the transition temperature itself requires care. A proper definition of a pseudocritical temperature should be related to the chiral phase transition in the massless limit of QCD and reduce to it in that limit. The aim of this paper is to study chiral and deconfinement aspects of the QCD transition at sufficiently small lattice spacing as to give control over the continuum extrapolation, and demonstrate the consistency of the results obtained with different actions. Furthermore, for the first time we provide a determination of the chiral transition temperature in the continuum limit that makes close connection with the critical behavior of QCD for massless light quarks.

This paper extends earlier calculations, performed with the asqtad and p4 actions on lattices with temporal extent $N_\tau = 8$ and light to strange quark mass ratio $m_l/m_s = 0.1$, in several ways. We have added calculations for $m_l/m_s = 0.05$ on $N_\tau = 8$ lattices and performed new calculations with the asqtad action at smaller lattice spacing, *i.e.*, for $N_\tau = 12$ with $m_l/m_s = 0.05$. More importantly, we have performed thermodynamic calculations with the highly improved staggered quark action (HISQ) [25] on lattices with temporal extent $N_\tau = 6, 8$ and 12 to quantify discretization errors. Preliminary versions of the results given in this paper have been presented in Refs. [26–34].

This paper is organized as follows. In the next section, we discuss thermodynamics calculations with improved staggered fermion actions, in particular, emphasizing the HISQ formulation which has been exploited in this context for the first time. We analyze the so-called taste symmetry violations in different improved staggered actions. Details of the simulation parameters used in our calculations are also given in this section. In Sec. III, we introduce the basic observables used in the analysis of the QCD transition and discuss their sensitivity to the expected critical behavior in the chiral limit. We present our numerical results for chiral observables in Sec. IV. In Sec. V, we discuss the universal properties of the chiral transition and the determination of the pseudocritical temperature. The deconfining aspect of the QCD transition, which is reflected in the temperature dependence of the quark number susceptibilities and the renormalized Polyakov loop, is discussed in Sec. VI. Finally, Sec. VII contains our conclusions. Details of the simulations, data and analysis are given in the appendices.

II. THERMODYNAMICS WITH STAGGERED FERMION ACTIONS

A. Staggered fermion actions

All staggered discretization schemes suffer from the well known fermion doubling problem, *i.e.*, a single staggered field describes four copies of Dirac quarks. These extra degrees of freedom are called taste and the full taste symmetry (degeneracy of the four tastes) is realized only in the continuum limit. At nonzero lattice spacing a taste symmetry is broken and only a taste non-singlet axial $U(1)$ symmetry survives. Consequently, in the chiral limit there is a single Goldstone meson, and the other 15 pseudoscalar mesons have masses of order $\alpha_s a^2$. For lattice spacings accessible in current numerical studies, the effects of taste breaking can produce significant distortions of the hadron spectrum. In thermodynamic calculations, these effects are expected to be most significant at low temperatures where the equation of state is governed by the spectrum of hadrons [35]. Current lattice calculations show that the distortion of the spectrum accounts for a large part of the deviations of the QCD equation of state from a hadron resonance gas estimate [35–38].

Several improvements to the staggered fermion formulation have been proposed to reduce the $\mathcal{O}(a^2)$ taste symmetry breaking effects. These improvements involve using smeared gauge fields or the so-called fat links [39] by including paths up to length seven in directions orthogonal to the link being fattened. With these improvements it is possible to completely cancel taste symmetry breaking effects at order $\alpha_s a^2$ [40]. Such an action is called asqtad and has been studied extensively [41]. Fat links are the sum of $SU(3)$ matrices corresponding to different paths on the hyper-cubic lattice, and are not elements of the $SU(3)$ group. It has been shown that projecting the fat links back to $SU(3)$ [42, 43] or even to the $U(3)$ group [44] greatly improves the taste symmetry. Projected fat links are being used in simulations with the stout action [22–24] and HISQ action [25, 45, 46]. In this paper, we confirm that this projection results in reductions of taste symmetry violations and a much better reproduction of the physical hadron spectrum in calculations starting at moderately coarse lattice spacing, *i.e.*, $a \sim 0.15$ fm.

In the generation of background gauge configurations, the reduction of the number of tastes from four to one for each flavor uses the so-called rooting procedure, *i.e.*, the fermion determinant in the QCD path integral is replaced by its fourth root. Effectively this amounts to averaging over the non-degenerate spectra of mesons and baryons, *e.g.*, over the non-degenerate spectrum of sixteen taste pions. The validity of this procedure is still a subject of debate [47, 48]. (For a more detailed summary of the issues, see Ref. [41].) Reducing taste symmetry violations is, in any case, important for making the rooted staggered theory a good approximation to a single flavor physical theory.

In the context of thermodynamic calculations, it is also important to control cutoff effects that manifest themselves as distortions of the high temperature ideal gas and perturbative high temperature limits. To reduce these $\mathcal{O}(a^2)$ effects we use improved staggered fermion actions that include three-link terms in the discretization of partial derivatives in the Dirac action. These three-link terms remove the tree-level $\mathcal{O}(a^2)$ discretization effects, which are the dominant ones at high temperatures [49, 50], as can be seen by considering the free energy density in the ideal gas limit calculated on four dimensional lattices with varying temporal extent N_τ . This free energy density of a quark gas divided by the corresponding result in the continuum limit ($N_\tau \rightarrow \infty$) is shown in Fig. 1. For the unimproved staggered fermion action with 1-link discretization, there is a significant cutoff dependence for $N_\tau < 16$. Including three-link terms in the action (p4 and Naik) reduces cutoff effects to a few percent even for $N_\tau = 8$. The Naik action with straight three-link terms is the building block for both the asqtad and HISQ actions; however, projection of fat links to $U(3)$ to further reduce taste violations is done only in the HISQ action. The stout action, on the other hand, uses just the standard 1-link discretization scheme with stout smeared links that include projection to $SU(3)$.

The HISQ action improves both taste symmetry breaking [25] and cutoff effects in the hadron spectrum which, as mentioned above, are of particular relevance to thermodynamic calculations at low temperatures. The construction of the projected fat link action proceeds in three steps. In the first step, a fat7 link is constructed; *i.e.*, a fat link which includes all the paths in orthogonal directions up to length seven. This step is common to the asqtad action. In step two, the sum of the product of $SU(3)$ matrices along these paths is projected to $U(3)$. In the third step, these projected fat links are used in the conventional asqtad Dirac operator without tadpole improvement. Thus, from the point of view of reducing taste symmetry breaking at order $\mathcal{O}(\alpha_s a^2)$ the asqtad and the HISQ actions are equivalent, but differ at higher orders. Unfortunately, these higher order terms are large in the asqtad action as discussed in Sec. IID where we show that the projection of fat links to $U(3)$ in the HISQ formulation significantly reduces the distortion of the spectrum at low temperatures. The straight three-link Naik term in the asqtad and HISQ actions eliminates the tree-level $\mathcal{O}(a^2)$ discretization effects, consequently, their behavior at high temperatures is equivalent.

For the HISQ calculations presented here, we use a tree-level improved Symanzik gauge action that is also common to the p4 and stout formulations. We refer to this combination of the gauge and 2+1 HISQ quark actions as the HISQ/tree action to distinguish it from the HISQ action used by the MILC collaboration in their large scale zero-temperature 2+1+1 flavor simulations with a dynamical charm quark [45, 46]. In the 2+1+1 HISQ action, in addition to the 1-loop tadpole improved version of the Symanzik gauge action, the 1-loop and mass dependent corrections are

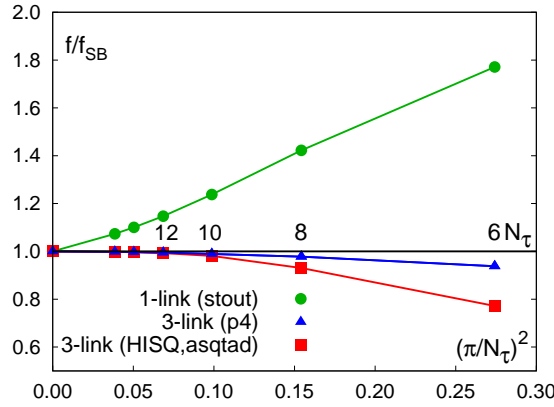


Figure 1: The free energy density of an ideal quark gas calculated for different values of the temporal extent N_τ divided by the corresponding value for $N_\tau = \infty$.

included in the Naik term for the charm quark.

B. Lattice Parameters and Simulation Details

A summary of the run parameters, statistics, and data for the p4, asqtad, and HISQ/tree actions analyzed in this paper is given in Appendix A. We have previously presented the equation of state and other thermodynamic quantities using the p4 and asqtad actions on lattices with temporal extent $N_\tau = 4, 6$, and 8 in Refs. [18–21]. Here, we extend these studies in the following three ways:

- Additional asqtad calculations for $N_\tau = 8$ with $m_l/m_s = 0.2$ and 0.05 . (See Table III in Appendix A.)
- New simulations with the asqtad action in the transition region on lattices with temporal extent $N_\tau = 12$ and light to strange quark mass ratio $m_l/m_s = 0.05$. (See Table IV in Appendix A.)
- New results with the HISQ/tree action on $N_\tau = 6$ lattices with $m_l/m_s = 0.2, 0.05$ and 0.025 ; on $N_\tau = 8$ lattices with $m_l/m_s = 0.05$ and 0.025 ; and on $N_\tau = 12$ lattices with $m_l/m_s = 0.05$. (See Tables V, VI and VII in Appendix A.)

As described in previous studies, the first step is to determine the line of constant physics (LCP) by fixing the strange quark mass to its physical value m_s at each value of the gauge coupling β [20, 21]¹. In practice, we tune m_s until the mass of the fictitious $\eta_{s\bar{s}}$ meson matches the lowest order chiral perturbation theory estimate $m_{\eta_{s\bar{s}}} = \sqrt{2m_K^2 - m_\pi^2}$ [19, 21]. Having fixed m_s , between one and three values of the light quark mass, $m_l/m_s = 0.2, 0.1, 0.05$ and 0.025 are investigated at each N_τ and used to obtain estimates at the physical point $m_l/m_s = 0.037$ by a scaling analysis discussed in Sections III and IV.

All simulations use the rational hybrid Monte-Carlo (RHMC) algorithm [51, 52]. The length of the RHMC trajectory is 0.5 in molecular dynamics (MD) time units (TU) for the p4 action and 1.0 for the asqtad action. The statistics, therefore, are given in terms of TUs in Tables II–VII in Appendix A. For each value of the input parameters, we accumulated several thousand TUs for zero-temperature ensembles and over ten thousand TUs for finite temperature runs. The RHMC algorithm for the HISQ action is discussed in Refs. [46, 53]. In the calculations with the HISQ/tree action, the length of the RHMC trajectory is typically one TU. For smaller values of β (coarse lattices) we used trajectories with length of $1/2$ and $1/3$ TU since frequent spikes in the fermion force term [53] reduce the acceptance rate for longer evolution times.

To control finite size effects, the ratio of spatial to temporal lattice size is fixed at $N_\sigma/N_\tau = 4$ in most of our finite temperature simulations. The exception is $N_\tau = 6$ runs at $m_l/m_s = 0.2$, which were done on lattices of size $16^3 \times 6$.

¹ In the case of the p4 action and for gauge couplings β close to the transition region, the bare quark masses were not varied with β to facilitate the Ferrenberg-Swendsen re-weighting procedure.

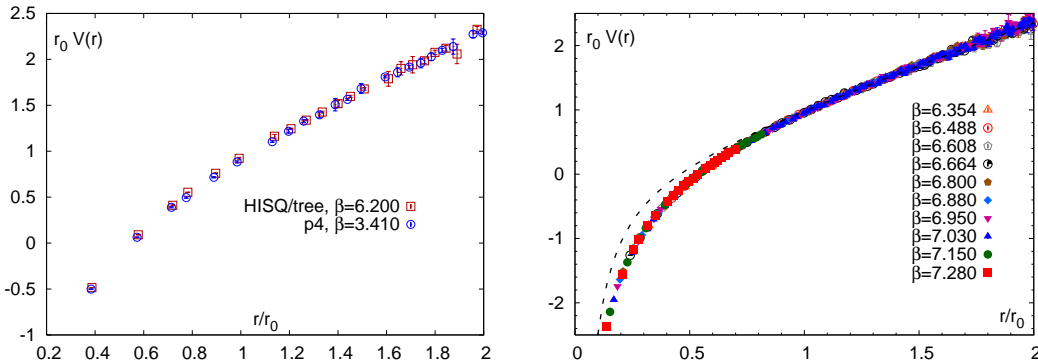


Figure 2: The static potential calculated for the HISQ/tree action with $m_l = 0.2m_s$ (left) and $m_l = 0.05m_s$ (right) in units of r_0 . In the plot on the left, we compare the HISQ/tree and p4 results obtained at a similar value of the lattice spacing. The dashed line in the plot on the right is the string potential $V_{string}(r) = -\pi/(12r) + \sigma r$ matched to the data at $r/r_0 = 1.5$.

Zero-temperature calculations have been performed for different lattice volumes (see Table VI in Appendix A) such that the spatial extent of the lattice L satisfies $LM_\pi > 3$, except for the smallest lattice spacings where $LM_\pi \simeq 2.6$.

The construction of renormalized finite temperature observables requires performing additive and multiplicative renormalizations. We implement these by subtracting corresponding estimates obtained at zero-temperature. These matching zero-temperature calculations have been performed at several values of the parameters and then fit by smooth interpolating functions over the full range of temperatures investigated.

In the following two subsections, we discuss the determination of the lattice spacing and the LCP for the HISQ/tree action, and the effect of taste symmetry breaking on the hadron spectrum.

C. The static potential and the determination of the lattice spacing

The lattice spacing is determined using the parameters r_0 and r_1 , which are fixed by the slope of the static quark anti-quark potential evaluated on zero-temperature lattices as [54]

$$\left(r^2 \frac{dV_{\bar{q}q}(r)}{dr} \right)_{r=r_0} = 1.65, \quad \left(r^2 \frac{dV_{\bar{q}q}(r)}{dr} \right)_{r=r_1} = 1.0, \quad (1)$$

and set the scale for all thermodynamic observables discussed in this work. The calculation of the static potential, r_0 and r_1 for the p4 action was discussed in Refs. [19, 21]. In particular, it was noticed that for the values of β relevant for the finite temperature crossover on $N_\tau = 8$ lattices, the parameter r_0 is the same, within statistical errors, for $m_l = 0.1m_s$ and $m_l = 0.05m_s$. Therefore, we use the interpolation formula for r_0 given in Ref. [19] to set the temperature scale for the p4 data. The calculation of the static potential and r_1 for the asqtad action was discussed in Ref. [41]. In Appendix B, we give further details on the determination of r_1 . Here we note that the statistical errors in the r_1/a determination are about 0.2% for gauge couplings relevant for the $N_\tau = 8$ calculations and about 0.1% for the $N_\tau = 12$ calculations. We also reevaluate systematic errors in the determination of r_1/a and find that these errors are smaller than 1% on $N_\tau = 12$ and about 1% on $N_\tau = 8$ lattices. These uncertainties will impact the precision with which the chiral transition temperature is estimated.

The static quark potential for the HISQ/tree action is calculated using the correlation functions of temporal Wilson lines of different length evaluated in the Coulomb gauge. The ratio of these correlators, calculated for two different lengths, was fit to a constant plus exponential function from which the static potential is extracted. To remove the additive UV divergence, we add a β -dependent constant $c(\beta)$ defined by the requirement that the potential has the value $0.954/r_0$ at $r = r_0$. This renormalization procedure is equivalent to the normalization of the static potential to the string potential $V_{string}(r) = -\pi/(12r) + \sigma r$ at $r = 1.5r_0$ [20]. The renormalized static potential, calculated for the HISQ/tree action for $m_l/m_s = 0.05$, is shown in Fig. 2(right) and we find no significant dependence on β (cutoff). We conclude that discretization errors, including the effects of taste symmetry violations, are much smaller in the static potential compared to other hadronic observables. Furthermore, for approximately the same value of r_0/a , the static potentials calculated with the HISQ/tree and p4 actions agree within the statistical errors as shown in Fig. 2(left).

To determine the parameters r_0 and r_1 , we fit the potential to a functional form that includes Coulomb, linear, and

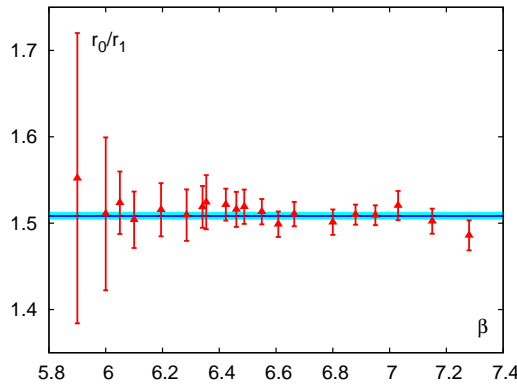


Figure 3: The ratio r_0/r_1 for the HISQ/tree action. Fitting all the data at $\beta \geq 6.423$ by a constant gives $r_0/r_1 = 1.508(5)$ as our best estimate of the continuum extrapolated value.

constant terms [41, 55]:

$$V(r) = C + \frac{B}{r} + \sigma r + \lambda \left(\frac{1}{r} \Big|_{lat} - \frac{1}{r} \right). \quad (2)$$

In this Ansatz, the Coulomb part is corrected for tree-level lattice artifacts by introducing a fourth parameter λ . The term proportional to λ reduces systematic errors in the determination of r_0 and r_1 due to the lack of rotational symmetry on the lattice at distances comparable to the lattice spacing. The resulting fit has a χ^2/dof close to unity for $r/a > \sqrt{3}$, except for the coarsest lattices corresponding to the transition region on $N_\tau = 6$ lattices. Consequently, we can determine r_0/a reliably for β corresponding to the transition region for $N_\tau = 8$ and $N_\tau = 12$ lattices. On lattices corresponding to the transition region for $N_\tau = 6$ we use a three parameter fit (Coulomb, linear and constant) with lattice distance replaced by tree-level improved distance, $r \rightarrow r_I$. Following Ref. [56], r_I was determined from the Coulomb potential on the lattice. Neither the three-parameter nor the four-parameter fit gives acceptable χ^2 ; however, the difference in the r_0 values obtained from these fits is of the order of the statistical errors. We use this difference as an estimate of the systematic errors on coarse lattices.

One can, in principle, extract r_0/a and r_1/a by using any functional form that fits the data in a limited range about these points to calculate the derivatives defined in Eq. (1). We use the form given in Eq. (2), but perform separate fits for extracting r_0/a and r_1/a for each ensemble. The fit range about r_0/a (or r_1/a) is varied keeping the maximum number of points that yield $\chi^2/\text{dof} \approx 1$. The variation in the estimates with the fit range is included in the estimate of the systematic error.

The value of r_1/a is more sensitive to the lattice artifacts in the potential at short distances than r_0/a . Only for lattice spacings corresponding to the transition region on $N_\tau = 12$ lattices are the lattice artifacts negligible. Again, we used the difference between four and three parameter fits to estimate the systematic error in r_1/a .

The lattice artifacts due to the lack of rotational symmetry play a more pronounced role in the determination of r_1/a , and are significantly larger for the HISQ/tree than for the asqtad action. This is presumably due to the lack of tadpole improvement in the gauge part of the HISQ/tree action. For this reason, we use r_0 on coarser lattices and r_1 on fine lattices and connect the two using the continuum estimate of r_0/r_1 for estimating the scale. Further details of this matching are given in Appendix B. As noted above, these effects are no longer manifest for the crossover region for $N_\tau = 12$ lattices.

Having calculated r_0/a , r_1/a and r_0/r_1 at a number of values of β , we estimate the continuum limit value for the ratio r_0/r_1 . In Fig. 3 we plot the data for the HISQ/tree action. It shows no significant variation with β , so we make two constant fits to study the dependence on the range of points included. The first fit includes all points with $\beta \geq 6.423$ and the second with $\beta \geq 6.608$. We take $r_0/r_1 = 1.508(5)$ from the first fit as our best estimate since it has a better $\chi^2/\text{dof} = 0.32$, includes more points and matches the estimate from a fit to all points. This estimate is higher than the published MILC collaboration estimate using the asqtad action: $r_0/r_1 = 1.474(7)(18)$ [55]. A more recent unpublished analysis, including data at smaller lattice spacings, gives $r_0/r_1 = 1.50(1)$ for the asqtad action [57], consistent with the HISQ/tree estimate. We will, therefore, quote $r_0/r_1 = 1.508(5)$ as our final estimate.

Finally, to extract the values of r_1 or r_0 in physical units, one has to calculate these quantities in units of some observable with a precisely determined experimental value. We use the result $r_1 = 0.3106(8)(18)(4)$ fm obtained by the MILC collaboration using f_π to set the lattice spacing [58]. This estimate is in good agreement with, and more precise than, the recent values obtained by the HPQCD collaboration: $r_1 = 0.3091(44)$ fm using bottomonium

splitting, $r_1 = 0.3157(53)$ fm using the mass splitting of D_s and η_c mesons, and $r_1 = 0.3148(28)(5)$ fm using $f_{s\bar{s}}$, the decay constant of the fictitious pseudoscalar $s\bar{s}$ meson [59]. To set the scale using r_0 , we use the above result for r_0/r_1 to convert from r_1 to r_0 . This gives $r_0 = 0.468(4)$ fm, which is consistent with the estimates $r_0 = 0.462(11)(4)$ fm by the MILC collaboration [55] and $r_0 = 0.469(7)$ fm by the HPQCD collaboration [60].

There are two reasons why we prefer to use either r_0 or r_1 to set the lattice scale. First, these are purely gluonic observables and therefore not affected by taste symmetry breaking inherent in hadronic probes. Second, as discussed above, r_0 (and r_1) do not show a significant dependence on m_l/m_s and thus one can extract reliable estimates for the physical LCP from simulations at $m_l/m_s = 0.05$. Nevertheless, we will also analyze the data using f_K to set the scale and discuss its extraction in Sec. IID.

D. Hadron masses and taste symmetry violation

Precision calculations of the hadron spectrum have been carried out with the asqtad action in Refs. [41, 55, 61]. Details of the calculations of hadron correlators and hadron masses used in this paper are given in Appendix C. For completeness, we also list there the masses of baryons estimated at the same lattice parameters.

As described in Sec. IIB, the strange quark mass is fixed by setting the mass of the lightest $s\bar{s}$ pseudoscalar to $\sqrt{2M_K^2 - M_\pi^2} = 686$ MeV [59]. Masses of all other pseudoscalar mesons should then be constant along the lines of constant physics defined by $m_l/m_s = 0.2$ and 0.05 . Fits to the data give

$$r_0 M_\pi = 0.3813(12), \quad r_0 M_K = 1.1956(33), \quad r_0 M_{\eta_{s\bar{s}}} = 1.6488(46), \quad m_l = 0.05 m_s, \quad (3)$$

$$r_0 M_\pi = 0.7373(14), \quad r_0 M_K = 1.2581(23), \quad r_0 M_{\eta_{s\bar{s}}} = 1.6206(30), \quad m_l = 0.20 m_s. \quad (4)$$

Using the value of r_0 determined in Sec. IIC, we find that the variation in $M_{\eta_{s\bar{s}}}$ over the range of β values simulated on the LCP is up to 2% for the HISQ/tree action. We neglect the systematic effect introduced by this variation in the rest of the paper as it is of the same order as the statistical errors. The LCP for the asqtad action, however, corresponds to a strange quark mass that is about 20% heavier than the physical value. We will comment on how we account for this deviation from the physical value in Sec. V.

Lattice estimates of hadron masses should agree with the corresponding experimental values in the continuum limit ²; however, at the finite lattice spacings used in thermodynamic calculations there are significant discretization errors. In staggered formulations, all physical states have taste partners with heavier masses that become degenerate only in the continuum limit. The breaking of the taste symmetry, therefore, introduces additional discretization errors, in particular, in thermodynamic observables at low temperatures where the degrees of freedom are hadrons. These artifacts have been observed in the deviations between lattice results and the hadron resonance gas model in the trace anomaly [20] and in fluctuations of conserved charges [36]. In this subsection, we will quantify these taste symmetry violations in the asqtad, stout and HISQ/tree actions and show that they are the smallest in the HISQ action [46].

To discuss the effects of taste symmetry violations, we analyze all sixteen pseudoscalar mesons that result from this four-fold doubling, and are classified into eight multiplets with degenerate masses. These are labeled by their taste index $\Gamma^F = \gamma_5, \gamma_0\gamma_5, \gamma_i\gamma_5, \gamma_0, \gamma_i, \gamma_i\gamma_0, \gamma_i\gamma_j, 1$ [62]. There is only one Goldstone boson, $\Gamma^F = \gamma_5$, that is massless in the chiral limit and the masses of the other fifteen pseudoscalar mesons vanish only in the chiral and continuum limits. The difference in the squared mass of the non-Goldstone and Goldstone states, $M_\pi^2 - M_G^2$, is the largest amongst mesons and their correlators have the best statistical signal; therefore, it is a good measure of taste symmetry violations. For different staggered actions, these violations, while formally of order $\alpha_s^n a^2$, are large as discussed below ³.

The taste splittings, $M_\pi^2 - M_G^2$, have been studied in detail for the asqtad and p4 actions [40, 55, 63]. The conclusion is that at a given β they are, to a good approximation, independent of the quark mass. Therefore, for the HISQ/tree action we calculate them on $16^3 \times 32$ lattices with $m_l/m_s = 0.2$ (see Table V), and on four 32^4 ensembles with $m_l = 0.05 m_s$ for sea quarks and $m_l/m_s = 0.2$ for valence quarks. (The lattice parameters for these ensembles at $\beta = 6.664, 6.8, 6.95$, and 7.15 are given in Table VI.) The corresponding results, plotted in Fig. 4, show the expected $\alpha_s^2 a^2$ scaling, similar to that observed previously with the HISQ action in the quenched approximation [25] and in full QCD calculations with four flavors [45, 46]. In this analysis, following Ref. [55], we use $\alpha_V(q = 3.33/a)$ from

² For the nucleon and Ω -baryon this has been demonstrated in Ref. [41].

³ For the unimproved staggered fermion action as well as for the stout action the quadratic pseudoscalar meson splittings are formally of order $\alpha_s a^2$, while for the asqtad and the HISQ actions they are of order $\alpha_s^2 a^2$. Projecting fat links to $U(3)$ reduces the coefficients of the $\alpha_s^2 a^2$ taste violating terms.

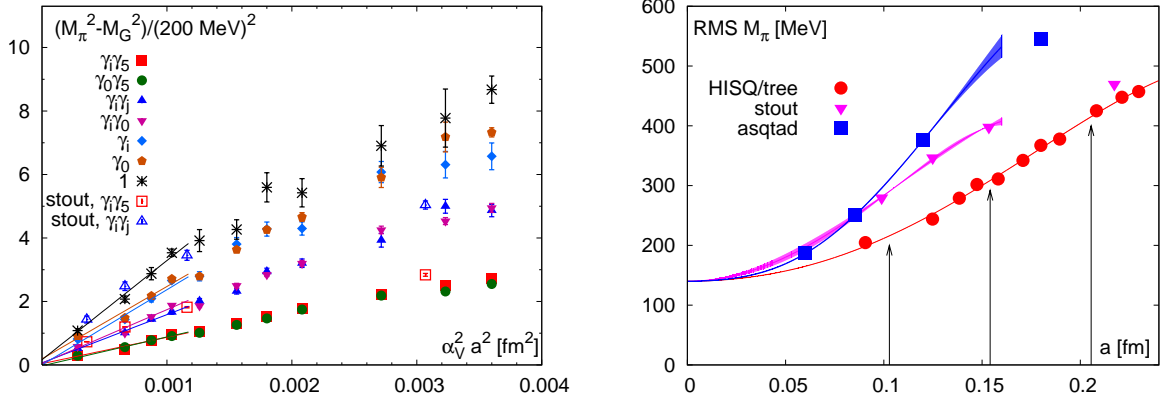


Figure 4: The splitting $M_\pi^2 - M_G^2$ of pseudoscalar meson multiplets calculated with the HISQ/tree and stout actions as a function of $\alpha_s^2 a^2$ (left). The right panel shows the RMS pion mass with $M_G = 140 \text{ MeV}$ as a function of the lattice spacing for the asqtad, stout and HISQ/tree actions. The band for the asqtad and stout actions shows the variation due to removing the fourth point at the largest a in the fit. These fits become unreliable for $a \gtrsim 0.16 \text{ fm}$ and are, therefore, truncated at $a = 0.16 \text{ fm}$. The vertical arrows indicate the lattice spacing corresponding to $T \approx 160 \text{ MeV}$ for $N_\tau = 6, 8$ and 12 .

the potential as an estimate of α_s . Linear fits in $\alpha_s^2 a^2$ to the four points at the smallest lattice spacings shown in Fig. 4(left) extrapolate to zero within errors in the continuum limit. The data also show the expected approximate degeneracies between the multiplets that are related by the interchange γ_i to γ_0 in the definition of Γ^F as predicted by staggered chiral perturbation theory [62].

The splittings for the stout action, taken from Ref. [23], for $\Gamma^F = \gamma_i \gamma_5$ and $\gamma_i \gamma_j$ are also shown in Fig. 4 with open symbols. We find that they are larger than those with the HISQ/tree action for comparable lattice spacings.

To further quantify the magnitude of taste-symmetry violations, we define, in MeV, the root mean square (RMS) pion mass as

$$M_\pi^{RMS} = \sqrt{\frac{1}{16} \left(M_{\gamma_5}^2 + M_{\gamma_0 \gamma_5}^2 + 3M_{\gamma_i \gamma_5}^2 + 3M_{\gamma_i \gamma_j}^2 + 3M_{\gamma_i \gamma_0}^2 + 3M_{\gamma_i}^2 + M_{\gamma_0}^2 + M_1^2 \right)}, \quad (5)$$

and plot the data in Fig. 4(right) with M_G tuned to 140 MeV . The data for the asqtad and stout actions were taken from Ref. [55] and Ref. [24], respectively. As expected, the RMS pion mass is the largest for the asqtad action and smallest for the HISQ/tree action. However, for lattice spacing $a \sim 0.104 \text{ fm}$, which corresponds to the transition region for $N_\tau = 12$, the RMS pion mass becomes comparable for the asqtad and stout actions. The deviations from the physical mass, $M_\pi = 140 \text{ MeV}$, become significant above $a = 0.08 \text{ fm}$ even for the HISQ/tree action. For the lattice spacings $\sim 0.156 \text{ fm}$ ($a \sim 0.206 \text{ fm}$), corresponding to the transition region on $N_\tau = 8$ ($N_\tau = 6$) lattices, the RMS mass is a factor of two (three) larger.

Next, we analyze the HISQ/tree data for pion and kaon decay constants, given in Appendix C, for $m_l/m_s = 0.05$. We also analyze the fictitious $\eta_{s\bar{s}}$ meson following Ref. [59]. In Fig. 5, we show our results in units of r_0 and r_1 determined in Sec. II C as a function of the lattice spacing together with a continuum extrapolation assuming linear dependence on a^2 . We vary the range of the lattice spacings used in the fit and take the spread in the extrapolated values as an estimate of the systematic errors. These extrapolated values agree with the experimental results within our estimated errors (statistical and systematic errors are added in quadrature) as also shown in Fig. 5. This consistency justifies having used the continuum extrapolated value of $f_\pi r_1$ from Ref. [58] to convert r_1 to physical units as discussed in Sec. II C. The deviation from the continuum value in the region of the lattice spacings corresponding to our finite temperature calculations is less than 8% for all the decay constants. We use these data to set the f_K scale and analyze thermodynamic quantities in terms of it and to make a direct comparison with the stout action data [22–24].

Finally, in Fig. 6 we show the masses of ϕ and K^* mesons given in Appendix C as a function of the lattice spacing. (The rho meson correlators are very noisy, so we do not present data for the rho mass.) Using extrapolations linear in a^2 we obtain continuum estimates, and by varying the fit interval, we estimate the systematic errors and add these to the statistical errors in quadrature. These estimates, in units of r_0 and r_1 , are plotted with the star symbol in Fig. 6. The experimental values along with error estimates are shown as horizontal bands and agree with lattice estimates, thereby providing an independent check of the scale setting procedure. The slope of these fits indicates that discretization errors are small and confirms the findings in [46] that taste symmetry violations are much smaller in the HISQ/tree action compared to those in the asqtad action. For the range of lattice spacings relevant for the

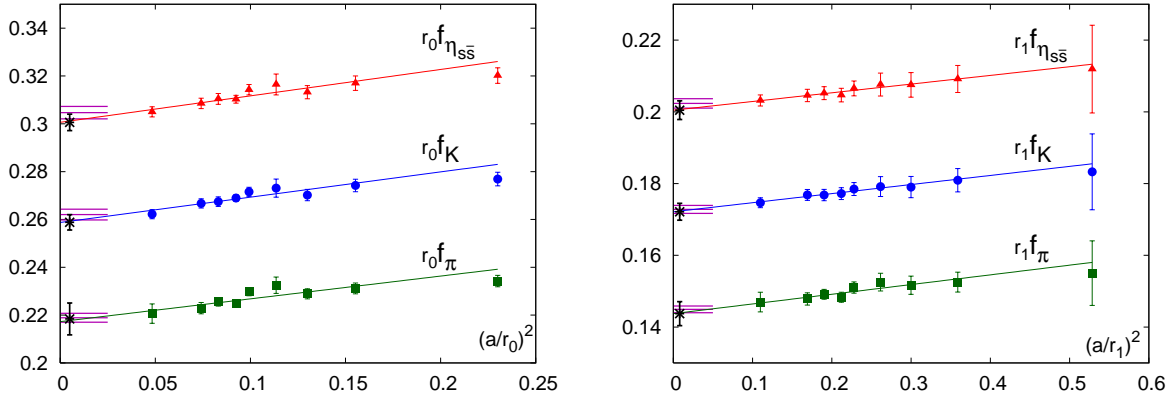


Figure 5: The decay constants of η_{ss} , K and π mesons with the HISQ/tree action at $m_l = 0.05m_s$ measured in units of r_0 (left) and r_1 (right) are shown as a function of the lattice spacings. The black points along the y -axis are the result of a linear extrapolation to the continuum limit. The experimental results are shown as horizontal bands along the y -axis with the width corresponding to the error in the determination of r_0 and r_1 , respectively. We use the HPQCD estimate for $f_{\eta_{ss}}$ [59] as the continuum value.

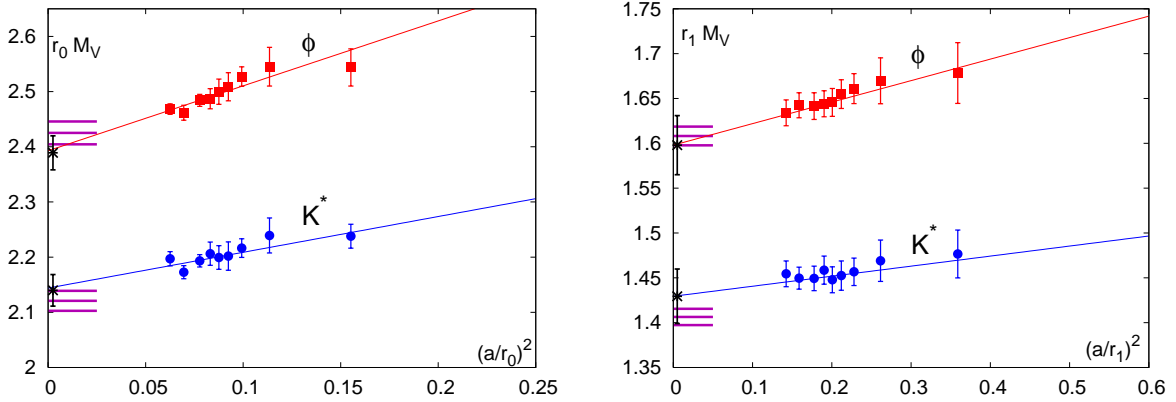


Figure 6: The masses of the ϕ and K^* mesons with the HISQ/tree action at $m_l = 0.05m_s$ measured in units of r_0 (left) and r_1 (right) are shown as a function of the lattice spacing. The lines show a linear continuum extrapolation and the black crosses denote the extrapolated values. The experimental results are shown as horizontal bands along the y -axis with the width corresponding to the error in the determination of r_0 and r_1 , respectively.

finite temperature transition region on $N_\tau = 6-12$ lattices, the discretization errors in the vector meson masses are less than 5%.

III. UNIVERSAL SCALING IN THE CHIRAL LIMIT AND THE QCD PHASE TRANSITION

In the limit of vanishing light quark masses and for sufficiently large values of the strange quark mass, QCD is expected to undergo a second order phase transition belonging to the universality class of three dimensional $O(4)$ symmetric spin models [9]. Although there remains the possibility that a fluctuation-induced first order transition may appear at (very) small values of the quark mass, it seems that the QCD transition for physical values of the strange quark mass is, indeed, second order when the light quark masses are reduced to zero. An additional complication in the analysis of the chiral phase transition in lattice calculations arises from the fact that the exact $O(4)$ symmetry is difficult to implement at nonzero values of the lattice spacing. Staggered fermions realize only a remnant of this symmetry; the staggered fermion action has a global $O(2)$ symmetry. The restoration of this symmetry at high temperatures is signaled by rapid changes in thermodynamic observables or peaks in response functions, which define pseudocritical temperatures. For these observables to be reliable indicators for the QCD transition, which becomes a true phase transition only in the chiral limit, one must select observables which, in the chiral limit, are dominated by

contributions arising from the singular part of the QCD partition function $Z(V, T)$, or more precisely from the free energy density, $f = -TV^{-1} \ln Z(V, T)$. A recent analysis of scaling properties of the chiral condensate, performed with the p4 action on coarse lattices, showed that critical behavior in the vicinity of the chiral phase transition is well described by $O(N)$ scaling relations [64] which give a good description even in the physical quark mass regime.

In the vicinity of the chiral phase transition, the free energy density may be expressed as a sum of a singular and a regular part,

$$f = -\frac{T}{V} \ln Z \equiv f_{sing}(t, h) + f_{reg}(T, m_l, m_s). \quad (6)$$

Here t and h are dimensionless couplings that control deviations from criticality. They are related to the temperature T and the light quark mass m_l , which couples to the symmetry breaking (magnetic) field, as

$$t = \frac{1}{t_0} \frac{T - T_c^0}{T_c^0}, \quad h = \frac{1}{h_0} H, \quad H = \frac{m_l}{m_s}, \quad (7)$$

where T_c^0 denotes the chiral phase transition temperature, *i.e.*, the transition temperature at $H = 0$. The scaling variables t, h are normalized by two parameters t_0 and h_0 , which are unique to QCD and similar to the low energy constants in the chiral Lagrangian. These need to be determined together with T_c^0 . In the continuum limit, all three parameters are uniquely defined, but depend on the value of the strange quark mass.

The singular contribution to the free energy density is a homogeneous function of the two variables t and h . Its invariance under scale transformations can be used to express it in terms of a single scaling variable

$$z = t/h^{1/\beta\delta} = \frac{1}{t_0} \frac{T - T_c^0}{T_c^0} \left(\frac{h_0}{H} \right)^{1/\beta\delta} = \frac{1}{z_0} \frac{T - T_c^0}{T_c^0} \left(\frac{1}{H} \right)^{1/\beta\delta} \quad (8)$$

where β and δ are the critical exponents of the $O(N)$ universality class and $z_0 = t_0/h_0^{1/\beta\delta}$. Thus, the dimensionless free energy density $\tilde{f} \equiv f/T^4$ can be written as

$$\tilde{f}(T, m_l, m_s) = h^{1+1/\delta} f_s(z) + f_r(T, H, m_s), \quad (9)$$

where the regular term f_r gives rise to scaling violations. This regular term can be expanded in a Taylor series around $(t, h) = (0, 0)$. In all subsequent discussions, we analyze the data keeping m_s in Eq. (9) fixed at the physical value along the LCP. Therefore, the dependence on m_s will, henceforth, be dropped.

We also note that the reduced temperature t may depend on other couplings in the QCD Lagrangian which do not explicitly break chiral symmetry. In particular, it depends on light and strange quark chemical potentials μ_q , which in leading order enter only quadratically,

$$t = \frac{1}{t_0} \left(\frac{T - T_c^0}{T_c^0} + \sum_{q=l,s} \kappa_q \left(\frac{\mu_q}{T} \right)^2 + \kappa_{ls} \frac{\mu_l}{T} \frac{\mu_s}{T} \right). \quad (10)$$

Derivatives of the partition function with respect to μ_q are used to define the quark number susceptibilities.

The above scaling form of the free energy density is the starting point of a discussion of scaling properties of most observables used to characterize the QCD phase transition. We will use this scaling Ansatz to test to what extent various thermodynamic quantities remain sensitive to universal features of the chiral phase transition at nonzero quark masses when chiral symmetry is explicitly broken and the singular behavior is replaced by a rapid crossover characterized by pseudocritical temperatures (which we label T_c) rather than a critical temperature.

A good probe of the chiral behavior is the 2-flavor light quark chiral condensate

$$\langle \bar{\psi}\psi \rangle_l^{n_f=2} = \frac{T}{V} \frac{\partial \ln Z}{\partial m_l}. \quad (11)$$

Following the notation of Ref. [64], we introduce the dimensionless order parameter M_b ,

$$M_b \equiv \frac{m_s \langle \bar{\psi}\psi \rangle_l^{n_f=2}}{T^4}. \quad (12)$$

Multiplication by the strange quark mass removes the need for multiplicative renormalization constants; however, M_b does require additive renormalization. For a scaling analysis in h at a fixed value of the cutoff, this constant plays no role. Near T_c^0 , M_b is given by a scaling function $f_G(z)$

$$M_b(T, H) = h^{1/\delta} f_G(t/h^{1/\beta\delta}) + f_{M,reg}(T, H), \quad (13)$$

and a regular function $f_{M,reg}(T, H)$ that gives rise to scaling violations. We consider only the leading order Taylor expansion of $f_{M,reg}(T, H)$ in H and quadratic in t ,

$$\begin{aligned} f_{M,reg}(T, H) &= a_t(T)H \\ &= \left(a_0 + a_1 \frac{T - T_c^0}{T_c^0} + a_2 \left(\frac{T - T_c^0}{T_c^0} \right)^2 \right) H \end{aligned} \quad (14)$$

with parameters a_0 , a_1 and a_2 to be determined. The singular function f_G is well studied in three dimensional spin models and has been parametrized for the $O(2)$ and $O(4)$ symmetry groups [65–68]. Also, the exponents β , γ , δ and ν used here are taken from Table 2 in Ref. [68].

Response functions, derived from the light quark chiral condensate, are sensitive to critical behavior in the chiral limit. In particular, the derivative of $\langle \bar{\psi}\psi \rangle_l^{n_f=2}$ with respect to the quark masses gives the chiral susceptibility

$$\chi_{m,l} = \frac{\partial}{\partial m_l} \langle \bar{\psi}\psi \rangle_l^{n_f=2}. \quad (15)$$

The scaling behavior of the light quark susceptibility, using Eq. (13), is

$$\begin{aligned} \frac{\chi_{m,l}}{T^2} &= \frac{T^2}{m_s^2} \left(\frac{1}{h_0} h^{1/\delta-1} f_\chi(z) + \frac{\partial f_{M,reg}(T, H)}{\partial H} \right), \\ \text{with } f_\chi(z) &= \frac{1}{\delta} [f_G(z) - \frac{z}{\beta} f'_G(z)]. \end{aligned} \quad (16)$$

The function f_χ has a maximum at some value of the scaling variable $z = z_p$. For small values of h this defines the location of the pseudocritical temperature T_c as the maximum in the scaling function $f_G(z)$. Approaching the critical point along h with z fixed, *e.g.*, $z = 0$ or $z = z_p$, $\chi_{m,l}$ diverges in the chiral limit as

$$\chi_{m,l} \sim m_l^{1/\delta-1}. \quad (17)$$

Similarly, the mixed susceptibility

$$\chi_{t,l} = -\frac{T}{V} \frac{\partial^2}{\partial m_l \partial t} \ln Z, \quad (18)$$

also has a peak at some pseudocritical temperature and diverges in the chiral limit as

$$\chi_{t,l} \sim m_l^{(\beta-1)/\beta\delta}. \quad (19)$$

One can calculate $\chi_{t,l}$ either by taking the derivative of $\langle \bar{\psi}\psi \rangle$ with respect to T or by taking the second derivative with respect to μ_l , *i.e.*, by calculating the coefficient of the second order Taylor expansion for the chiral condensate as a function of μ_l/T [69]. The derivative of $\langle \bar{\psi}\psi \rangle$ with respect to T is the expectation value of the chiral condensate times the energy density, which is difficult to calculate in lattice simulations, as additional information on temperature derivatives of temporal and spatial cutoff parameters is needed. Taylor expansion coefficients, on the other hand, are well defined and have been calculated previously, although their calculation is computationally intensive. This mixed susceptibility has been used to determine the curvature of the chiral transition line for small values of the baryon chemical potential [69].

Other thermodynamic observables analyzed in this paper are the light and strange quark number susceptibilities defined as

$$\frac{\chi_q}{T^2} = \frac{1}{VT^3} \frac{\partial^2 \ln Z}{\partial (\mu_q/T)^2}, \quad q = l, s. \quad (20)$$

These are also sensitive to the singular part of the free energy since the reduced temperature t depends on the quark chemical potentials as indicated in Eq. (10). However, unlike the temperature derivative of the chiral condensate, *i.e.*, the mixed susceptibility $\chi_{t,l}$, the temperature derivative of the light quark number susceptibility does not diverge in the chiral limit. Its slope at T_c^0 is given by

$$\frac{\partial \chi_q}{\partial T} \sim c_r + A_\pm \left| \frac{T - T_c^0}{T_c^0} \right|^{-\alpha}, \quad (21)$$

and has the contribution c_r from the regular part of the free energy, while its variation with temperature is controlled by the singular part. The critical exponent α is negative for QCD since the chiral transition is expected to belong to the universality class of three-dimensional $O(N)$ models. In short, while χ_q is sensitive to the critical behavior, it does not diverge in the thermodynamic limit. Consequently, it has been extremely difficult to extract reliable information on T_c^0 or T_c from scaling fits to χ_q . Even in high statistics $O(N)$ model calculations [70] the structure of the subleading term in Eq. (21) could only be determined after using results for the dominant contribution c_r extracted from other observables. We, therefore, consider quark number susceptibilities as a good indicator of the transition in QCD, but not useful for extracting precise values for the associated pseudocritical temperature.

Finally, we consider the expectation value of the Polyakov loop L ,

$$L(\vec{x}) = \frac{1}{3} \text{Tr} \prod_{x_0=1}^{N_\tau} U_0(x_0, \vec{x}) , \quad (22)$$

which is the large distance limit of the static quark correlation function,

$$L^2 \equiv \lim_{|\vec{x}| \rightarrow \infty} \langle L(0) L^\dagger(\vec{x}) \rangle . \quad (23)$$

$L \equiv \langle L(\vec{x}) \rangle$ is a good order parameter for deconfinement in the limit of infinitely heavy quarks. In that limit, it can be related to the singular structure of the partition function of the pure gauge theory and can be introduced as a symmetry breaking field in the action. In QCD with light quarks, in particular in the chiral limit, L is no longer an order parameter due to the explicit breaking of the $Z(3)$ center symmetry by the quark action. It does not vanish for $T \leq T_c^0$, but is determined by the value of the free energy of a static quark F_Q in the confined phase. This free energy can be well approximated by the binding energy of the lightest static-light meson, which is of order Λ_{QCD} . Similarly, $T_c \sim \Lambda_{QCD}$; consequently $L \sim \exp(-F_Q/T) \sim 1/e$ is not small in the confined phase. The data for QCD with light quarks show that L varies significantly with temperature in the transition region, reflecting the rapid change in screening properties of an external color charge. Thus, the Polyakov loop is sensitive to the transition but it has no demonstrated relation to the singular part of the QCD partition function. We, therefore, do not use it to determine an associated pseudocritical temperature.

IV. CHIRAL OBSERVABLES

In this section, we present results for observables related to chiral symmetry restoration at finite temperatures and discuss the cutoff dependence of these quantities. To set the normalization of different quantities we express them in terms of the staggered fermion matrix $D_q = m_q \cdot 1 + D$ with $q = l, s$, as in Ref. [20]. In what follows, $\langle \bar{\psi}\psi \rangle_{q,\tau}$ will denote the one-flavor chiral condensate, *i.e.*,

$$\langle \bar{\psi}\psi \rangle_{q,x} = \frac{1}{4} \frac{1}{N_\sigma^3 N_\tau} \text{Tr} \langle D_q^{-1} \rangle, \quad q = l, s , \quad (24)$$

where the subscript $x = \tau$ and $x = 0$ will denote the expectation value at finite and zero temperature, respectively. The chiral susceptibility defined in Sec. III is the sum of connected and disconnected Feynman diagrams defined as

$$\chi_{m,l}(T) = 2 \frac{\partial \langle \bar{\psi}\psi \rangle_{l,\tau}}{\partial m_l} = \chi_{l,disc} + \chi_{l,con} , \quad (25)$$

$$\chi_{m,s}(T) = \frac{\partial \langle \bar{\psi}\psi \rangle_{s,\tau}}{\partial m_s} = \chi_{s,disc} + \chi_{s,con} , \quad (26)$$

with

$$\chi_{q,disc} = \frac{n_f^2}{16 N_\sigma^3 N_\tau} \left\{ \langle (\text{Tr} D_q^{-1})^2 \rangle - \langle \text{Tr} D_q^{-1} \rangle^2 \right\} , \quad (27)$$

and

$$\chi_{q,con} = -\frac{n_f}{4} \text{Tr} \sum_x \langle D_q^{-1}(x, 0) D_q^{-1}(0, x) \rangle , \quad q = l, s. \quad (28)$$

Here $n_f = 2$ for light quark susceptibilities, and $n_f = 1$ for the strange quark susceptibilities. The disconnected part of the light quark susceptibility describes the fluctuations in the light quark condensate and is directly analogous to the fluctuations in the order parameter of an $O(N)$ spin model. The second term ($\chi_{q,con}$) arises from the explicit quark mass dependence of the chiral condensate and is the expectation value of the volume integral of the correlation function of the (isovector) scalar operator $\bar{\psi}\psi$.

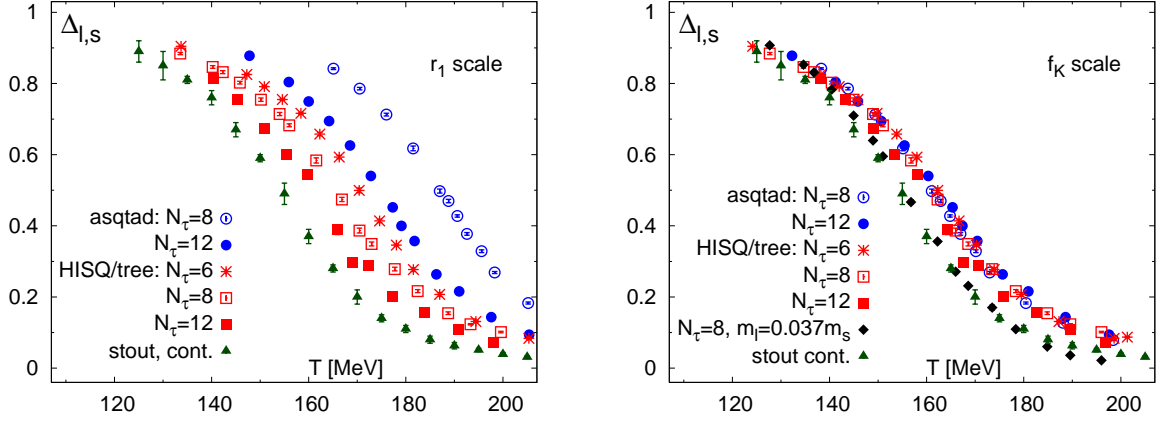


Figure 7: The subtracted chiral condensate for the asqtad and HISQ/tree actions with $m_l = m_s/20$ is compared with the continuum extrapolated stout action results [24] (left panel). The temperature T is converted into physical units using r_1 in the left panel and f_K in the right. We find that the data collapse into a narrow band when f_K is used to set the scale. The black diamonds in the right panel show HISQ/tree results for $N_\tau = 8$ lattices after an interpolation to the physical light quark mass using the $m_l/m_s = 0.05$ and 0.025 data.

A. The chiral condensate

The chiral condensate $\langle \bar{\psi}\psi \rangle$ requires both multiplicative and additive renormalizations at finite quark masses. The leading additive renormalization is proportional to (m_q/a^2) .⁴ To remove these UV divergences, we consider the subtracted chiral condensate introduced in Ref. [19],

$$\Delta_{l,s}(T) = \frac{\langle \bar{\psi}\psi \rangle_{l,\tau} - \frac{m_l}{m_s} \langle \bar{\psi}\psi \rangle_{s,\tau}}{\langle \bar{\psi}\psi \rangle_{l,0} - \frac{m_l}{m_s} \langle \bar{\psi}\psi \rangle_{s,0}}. \quad (29)$$

Our results for the HISQ/tree and asqtad actions at $m_l = 0.05m_s$ are shown in Fig. 7(left) and compared to the continuum estimate obtained with the stout action [24]. The temperature scale is set using r_0 and r_1 as discussed in Section II C and Appendix B. The asqtad results obtained on $N_\tau = 8$ lattices deviate significantly from the stout results as observed previously [20]. The new data show that these differences are much smaller for $N_\tau = 12$ ensembles. More important, the discretization effects and the differences from the stout continuum results are much smaller for the HISQ/tree data.

In Fig. 7(right), we analyze the data for $\Delta_{l,s}$ using the kaon decay constant f_K to set the lattice scale. For the HISQ/tree action, we use the values of f_K discussed in Sec. II C, while for the asqtad action, we use f_K from staggered chiral fits (see the discussion in appendix B). We note that for $m_l/m_s = 1/20$ all the data obtained with the HISQ/tree and asqtad actions on different N_τ lattices collapse into one curve, indicating that $\Delta_{l,s}$ and f_K have similar discretization errors. The remaining difference between the stout and our estimates, as shown next, is due to the difference in the quark masses—calculations with the stout action were done with $m_l = 0.037m_s$ whereas our calculations correspond to $m_l = 0.05m_s$.

For a direct comparison with stout results, we extrapolate our HISQ/tree data in the light quark mass. This requires estimating the quark mass dependence of the chiral condensate at both zero and non-zero temperatures. For the $T = 0$ data, we perform a linear extrapolation in the quark mass using the HISQ/tree lattices at $m_l = 0.05m_s$ and $0.20m_s$. For the non-zero T data, we use the $O(N)$ scaling analysis, described in Sec. V, which gives a good description of the quark mass dependence in the temperature interval $150\text{MeV} < T < 200\text{ MeV}$. The resulting $N_\tau = 8$ HISQ/tree estimates at the physical quark mass are shown in Fig. 7(right) as black diamonds and agree with the stout action results [22–24] plotted using green triangles.

We can also remove the multiplicative renormalization factor in the chiral condensate by considering the renormalization group invariant quantity $r_1^4 m_s \langle \bar{\psi}\psi \rangle_l$, where m_s is the strange quark mass. The additive divergences can be

⁴ There is also a logarithmic divergence proportional to m_q^3 , which we neglect.

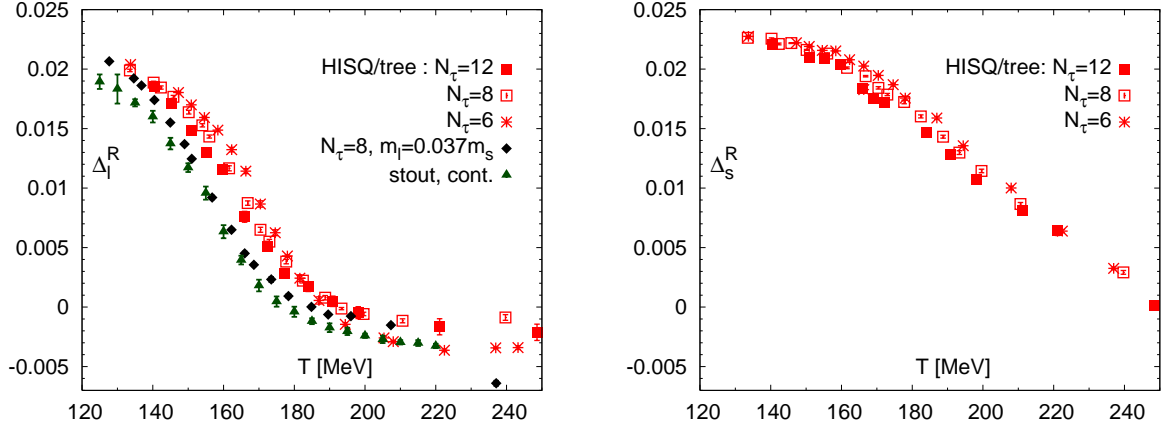


Figure 8: The renormalized chiral condensate Δ_l^R for the HISQ/tree action with $m_l/m_s = 0.05$ is compared to the stout data. In the right panel, we show the renormalized strange quark condensate Δ_s^R for the HISQ/tree action. The temperature scale in both figures is set using r_1 . The black diamonds in the left panel show the $N_\tau = 8$ HISQ/tree estimates using the f_K scale and after an interpolation to the physical light quark mass $m_l/m_s = 0.037$ as discussed in the text.

removed by subtracting the zero temperature analogue, *i.e.*, we consider the quantity

$$\Delta_l^R = d + 2m_s r_1^4 (\langle \bar{\psi}\psi \rangle_{l,\tau} - \langle \bar{\psi}\psi \rangle_{l,0}). \quad (30)$$

Note that Δ_l^R is very similar to the renormalized chiral condensate $\langle \bar{\psi}\psi \rangle_R$ introduced in Ref. [24], but differs by the factor $(m_l/m_s)/(r_1^4 m_\pi^4)$ and d . A natural choice for d is the value of the chiral condensate in the zero light quark mass limit times $m_s r_1^4$. In this limit Δ_l^R should vanish above the critical temperature. To estimate d , we use the zero temperature estimate $\langle \bar{\psi}\psi \rangle_l(\overline{MS}, \mu = 2\text{GeV}) = 242(9)^{(+5)}_{(-17)}(4) \text{ MeV}^3$ determined in the chiral limit using $SU(2)$ staggered chiral perturbation theory by the MILC collaboration [41] and the corresponding strange quark mass $m^{MS}(\bar{\mu} = 2\text{GeV}) = 88(5) \text{ MeV}$. We get $d = 0.0232244$.

We show Δ_l^R for the HISQ/tree action and the stout continuum results in Fig. 8(left)⁵. To compare with the stout continuum results, we need to extrapolate the HISQ/tree data both to the continuum limit and to the physical quark mass. To perform the continuum extrapolation we convert Δ_l^R to the f_K scale in which discretization errors, as already noted for $\Delta_{l,s}$, are small. We then interpolate these $N_\tau = 8$ data at $m_l/m_s = 0.05$ and 0.025 to the physical quark mass $m_l/m_s = 0.037$. These estimates of the continuum HISQ/tree Δ_l^R are shown in Fig. 8(left) as black diamonds and are in agreement with the stout results (green triangles) [24].

Lastly, in Fig. 8(right), we show the subtracted renormalization group invariant quantity, Δ_s^R , which is related to the chiral symmetry restoration in the strange quark sector. We find a significant difference in the temperature dependence between Δ_l^R and Δ_s^R , with the latter showing a gradual decrease rather than a crossover behavior.

B. The chiral susceptibility

As discussed in Sec. III, the chiral susceptibility $\chi_{m,l}$ is a good probe of the chiral transition in QCD as it is sensitive to the singular part of the free energy density. It diverges in the chiral limit, and the location of its maximum at nonzero values of the quark mass defines a pseudocritical temperature T_c that approaches the chiral phase transition temperature T_c^0 as $m_l \rightarrow 0$.

For sufficiently small quark masses, the chiral susceptibility is dominated by the disconnected part, therefore, T_c can also be defined as the location of the peak in the disconnected chiral susceptibility defined in Eq. (27). As we will show later, $\chi_{q,disc}$ does not exhibit an additive ultraviolet divergence but does require a multiplicative renormalization⁶.

⁵ We multiply the stout results by $(m_s/m_l) = 27.3$ and by $r_1^4 m_\pi^4 = 0.0022275$. For the latter factor, we use the physical pion mass and the value of r_1 determined in [58] and discussed in Sec. II C.

⁶ It is easy to see that at leading order in perturbation theory, *i.e.*, in the free theory, the disconnected chiral susceptibility vanishes and thus is non-divergent. Our numerical results at zero temperature do not indicate any quadratic divergences in the disconnected chiral susceptibility, but logarithmic divergences are possible.

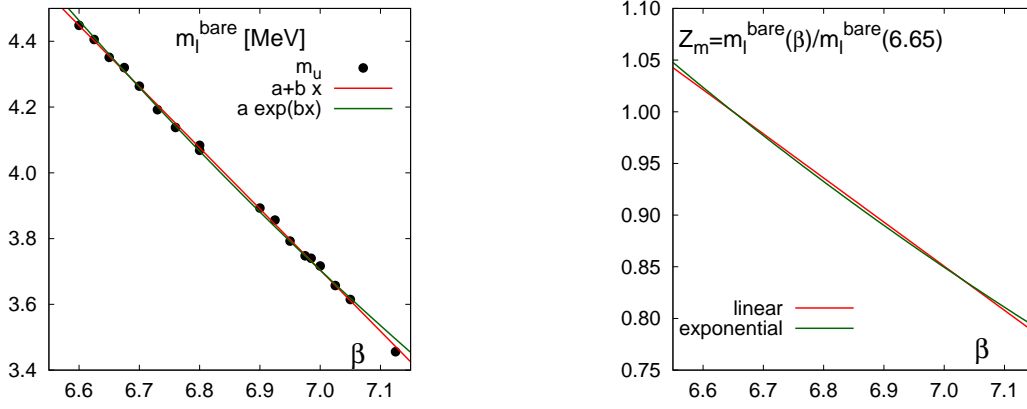


Figure 9: Value of the bare light quark mass, in MeV using r_1 to set the scale, on the line of constant physics for the asqtad action *vs.* the lattice gauge coupling β . The right hand part of the figure shows the change of the renormalization constants with β , *i.e.*, with the cutoff, relative to the arbitrarily chosen renormalization point $\beta = 6.65$.

1. Disconnected chiral susceptibility

The multiplicative renormalization factors for the chiral condensate and the chiral susceptibility can be deduced from an analysis of the line of constant physics for the light quark masses, $m_l(\beta)$. The values of the quark mass for the asqtad action, converted to physical units using r_1 , are shown in Fig. 9(left). The variation with β gives the scale dependent renormalization of the quark mass (its reciprocal is the renormalization factor for the chiral condensate). What $m_l(\beta)$ does not fix is the renormalization scale, which we choose to be $r_0/a = 3.5$ (equivalently $r_1/a = 2.37$ or $a = 0.134$ fm), and the “scheme”, which we choose to be the asqtad action. For the asqtad action, this scale corresponds to the coupling $\beta = 6.65$ which is halfway between the peaks in the chiral susceptibility on $N_\tau = 8$ and 12 lattices. This specification, $Z_m(\text{asqtad}) = 1$ at $r_0/a = 3.5$, is equivalent to choosing, for a given action, the renormalization scale Λ which controls the variation of Z_m with coupling β as shown in Fig. 9(right) for the asqtad action.

A similar calculation of Z_m is performed for the p4 and HISQ/tree actions. It is important to note that choosing the same reference point $r_0/a = 3.5$ and calculating $Z_m(\beta)$ for each of the actions leaves undetermined a relative renormalization factor between the actions, *i.e.*, the relation between the corresponding Λ ’s of the different schemes. This relative factor between any two actions is also calculable and given by the ratio of the (bare) quark mass along the physical LCP at $r_0/a = 3.5$. At this scale our data give

$$\frac{m(\text{asqtad})}{m(\text{HISQ/tree})} = 0.97828. \quad (31)$$

Recall, however, that along the LCP the quark masses, m_s and therefore m_l , for the asqtad action are about 20% heavier than the physical values. Noting that the lattice scale at a given β is set using a quark-mass independent procedure, we correct $m(\text{asqtad})$ by the factor $(M_\pi r_0)^2|_{\text{HISQ/tree}}/(M_\pi r_0)^2|_{\text{asqtad}}$. Then, at $r_0/a = 3.5$

$$\frac{m(\text{asqtad})}{m(\text{HISQ/tree})} = 0.782 \quad \text{i.e.} \quad \frac{Z_m(\text{asqtad})}{Z_m(\text{HISQ/tree})} = 1.2786. \quad (32)$$

Given $Z_m(\beta)$ we get $Z_{\bar{\psi}\psi} \equiv Z_S = 1/Z_m$ and $Z_\chi = 1/Z_m^2$. A similar calculation of Z_m has been carried out for the p4 action.

The systematics of the quark mass and cutoff dependence of the disconnected part of the chiral susceptibility is analyzed in more detail for the p4 and asqtad actions in Fig. 10. The data show a rapid rise in $\chi_{l,\text{disc}}/T^2$ with decreasing quark mass at low temperatures and in the transition region. This mass dependence can be traced back to the leading thermal correction to the chiral condensate. At finite temperature and for sufficiently small quark masses, the chiral order parameter can be understood in terms of the 3-dimensional $O(N)$ models. A dimensional reduction is applicable because the Goldstone modes are light in this region. Based on the $O(N)$ model analysis, the quark mass dependence of the chiral condensate is expected to have the form [71–74]

$$\langle \bar{\psi}\psi \rangle_l(T, m_l) = \langle \bar{\psi}\psi \rangle_l(0) + c_2(T)\sqrt{m_l} + \dots, \quad (33)$$

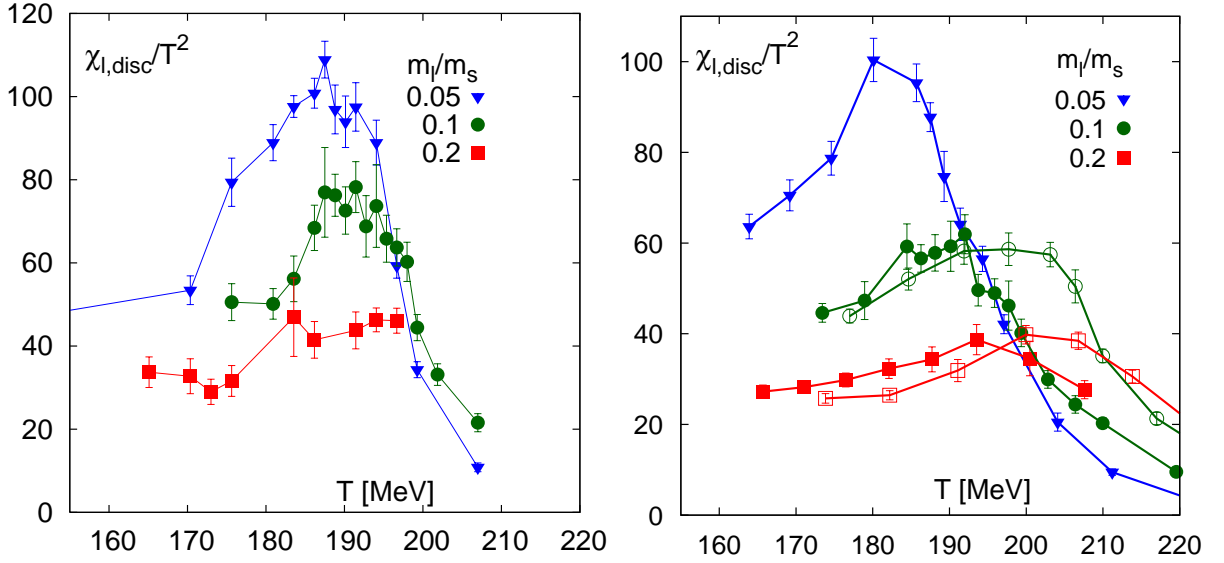


Figure 10: The disconnected part of the chiral susceptibility, including multiplicative renormalization, calculated on $N_\tau = 8$ lattices for the p4 (left) and asqtad (right) actions at three light quark masses. The figure on the right also shows asqtad data from $N_\tau = 6$ lattices as open symbols.

as has been confirmed in numerical simulations with the p4 action on $N_\tau = 4$ lattices [64]. Consequently for $T < T_c^0$, there is a $m_l^{-1/2}$ singularity in the chiral susceptibility in the limit of zero quark mass which explains the rise in $\chi_{l, \text{disc}}/T^2$.

A second feature of the data is shown in Fig. 10(right) which compares data for the asqtad action on lattices of different N_τ at $m_l/m_s = 0.2$ and 0.1 . Open (filled) symbols denote data on $N_\tau = 6$ ($N_\tau = 8$) lattices. The data show a shift towards smaller temperature values of both the peak and the rapidly dropping high temperature part when the lattice spacing is reduced. The data also show that the variation of the shape of the susceptibility above the peak is weakly dependent on the quark mass. This is expected as χ_l is the derivative of the chiral condensate with respect to the mass which, as shown in Fig. 8, is almost linear in the quark mass in this temperature regime. Thirdly, the data in Fig. 10(right) show that the height of the multiplicatively renormalized disconnected chiral susceptibility at fixed m_l/m_s is similar for $N_\tau = 6$ and $N_\tau = 8$ lattices. This lack of increase in height with N_τ supports the hypothesis that there are no remaining additive divergent contributions in the disconnected part of the chiral susceptibility.

In Fig. 11, we compare, for $m_l/m_s = 0.05$, the disconnected part of the chiral susceptibility including the multiplicative renormalization factor Z_χ . We note three features in the data. First, the variation in the position of the peak for the asqtad action is larger between $N_\tau = 8$ and 12 than for the HISQ/tree action between $N_\tau = 6$ and 8 . Second, the peak height increases for the HISQ/tree data and decreases for the asqtad data with N_τ . Lastly, the agreement in the location of the peak for the two actions and the data above the peak is much better when f_K is used to set the scale as shown in Fig. 11(right). Note that the peak height for the two actions is not expected to match since the quark masses on the LCP for the asqtad data are about 20% heavier than for the HISQ/tree data.

2. Connected chiral susceptibilities

The connected part of the chiral susceptibility, Eq. (28), is the volume integral of the scalar, flavor nonsinglet meson correlation function. At large distances, where its behavior is controlled by the lightest scalar, nonsinglet screening mass, the correlation function drops exponentially as this state has a mass gap, *i.e.*, $\chi_{l, \text{con}}$ can diverge in the thermodynamic limit only if the finite temperature screening mass in this channel vanishes. This, in turn, would require the restoration of the $U_A(1)$ symmetry, which is not expected at the QCD transition temperature. In fact, the scalar screening masses are known to develop a minimum at temperatures above, but close to, the transition temperature [75]. One therefore expects that even in the chiral limit, the connected part of the chiral susceptibility will only exhibit a maximum above the chiral transition temperature.

There are two subtle features of the connected part of the susceptibility calculated at nonzero lattice spacings that require further discussion. First, taste symmetry violations in staggered fermions introduce an additional divergence of the form $a^2/\sqrt{m_l}$ for $T < T_c^0$. It also arises due to the long distance fluctuations of Goldstone pions, as explained

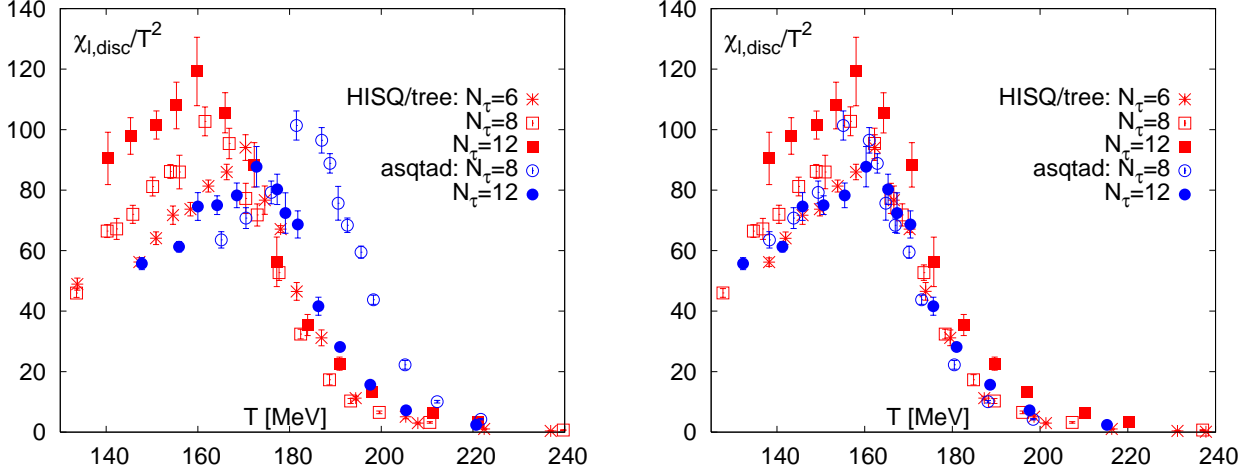


Figure 11: The disconnected part of the chiral susceptibility for the asqtad and HISQ/tree actions, including the multiplicative renormalization constant discussed in the text, is shown for $m_l = m_s/20$ and different N_τ . In the right panel, the same data are plotted using f_K to set the scale. Plotted this way they show much smaller variation with N_τ .

in Eq. (33), however, unlike the divergence in the disconnected part which is physical, this term is proportional to the $O(a^2)$ taste breaking. Note that in the two-flavor theory there are no such divergences due to Goldstone modes in the continuum limit [73, 74]. Thus, we expect to observe a strong quark mass dependence at low temperatures in $\chi_{l, \text{con}}$. Second, there is a large reduction in the $U_A(1)$ symmetry breaking in the transition region, consequently there will be a significant quark mass dependence of scalar screening masses and of $\chi_{l, \text{con}}$.

We have calculated $\chi_{l, \text{con}}$ for the p4, asqtad and HISQ/tree actions. Results at different light quark masses from $N_\tau = 8$ lattices are shown in Fig. 12 for the p4 and asqtad actions with the multiplicative renormalization performed in the same way as for $\chi_{l, \text{disc}}$. A strong dependence on the quark mass is seen in both the p4 and asqtad data. This, as conjectured above, is due to a combination of the artifacts that are due to taste symmetry breaking and the variations with temperature of the scalar, flavor nonsinglet screening mass at and above the crossover temperatures.

In Fig. 13, we show the connected chiral susceptibility for the asqtad and HISQ/tree actions at fixed $m_l = 0.05m_s$ for different N_τ . In Sec. IV A, we noted the presence of an additive quadratic divergence, proportional to m_q/a^2 , in the chiral condensate, which will give rise to a mass-independent quadratic divergence in the chiral susceptibility. We find that the absolute value of the data grows with N_τ as expected. Since this divergent contribution is the same for light and strange susceptibilities, it can be eliminated by constructing the difference $\chi_{l, \text{con}} - 2\chi_{s, \text{con}}$. The resulting data are shown in Fig. 13(right), and we find that the peak occurs at slightly higher T as compared to the disconnected chiral susceptibility shown in Fig. 11. Also, we find that the height of the peak decreases with N_τ and the position of the peak is shifted to smaller temperatures on decreasing the lattice spacing, which is most evident when comparing the $N_\tau = 8$ and $N_\tau = 12$ asqtad data.

3. Renormalized two-flavor chiral susceptibility

Lastly, we compare our estimates for the two-flavor chiral susceptibility, defined in Eqs. (27) and (28), with results obtained with the stout action [22]. To remove the additive ultraviolet divergence discussed above, we now subtract the zero temperature rather than the strange quark chiral susceptibility. Furthermore, to get rid of the multiplicative renormalization, this combination is multiplied by m_s^2 , i.e., the following quantity is considered

$$\frac{\chi_R(T)}{T^4} = \frac{m_s^2}{T^4} (\chi_{m, l}(T) - \chi_{m, l}(T=0)). \quad (34)$$

This construct has the advantage of being renormalization group invariant and, unlike the definition in Ref. [22], it does not vanish in the chiral limit. In Fig. 14(left), we show data for the stout, HISQ/tree and asqtad actions with the scale set by r_1 . The stout data have been taken from Ref. [22] and multiplied by $(m_s/m_l)^2 = (27.3)^2$ to conform to Eq. (34) [22, 23]. The HISQ/tree results on $N_\tau = 12$ lattices are not shown as the corresponding zero temperature calculations are not yet complete. We find that the large difference between the continuum stout and $N_\tau = 8$ asqtad results is significantly reduced by $N_\tau = 12$. Second, the cutoff dependence for the HISQ/tree data is much smaller

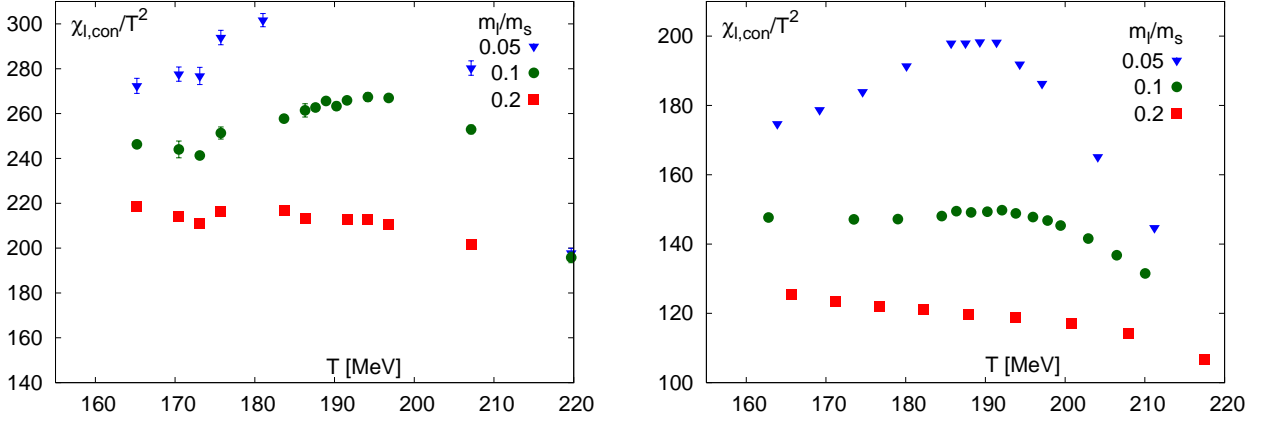


Figure 12: The connected part of the chiral susceptibility for the p4 (left) and asqtad (right) actions for different quark masses on $N_\tau = 8$ lattices.

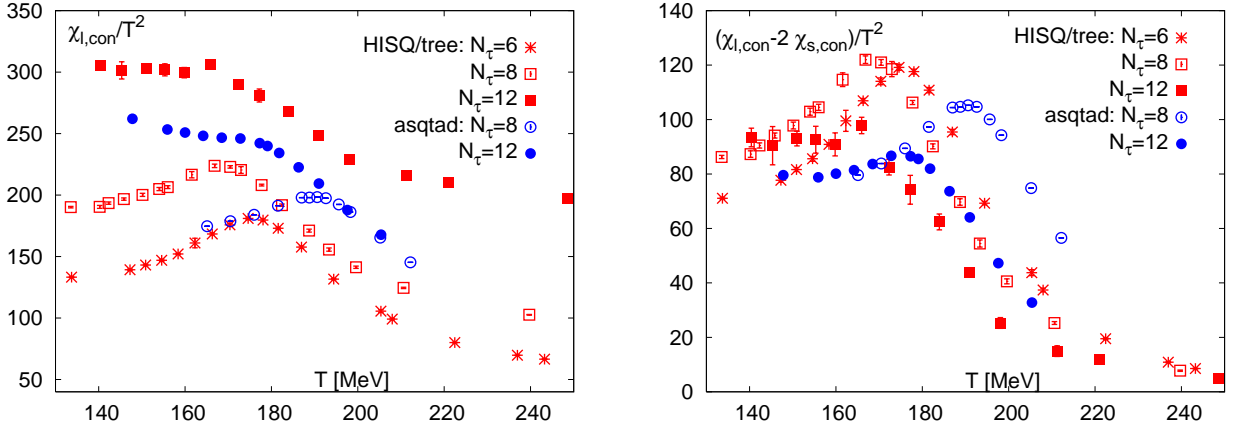


Figure 13: The connected part of the chiral susceptibility for the asqtad and HISQ/tree actions on the LCP defined by $m_l = 0.05m_s$. In the right hand figure, we show the difference of the light and strange quark connected susceptibilities in which the divergent additive artifact cancels.

than for the asqtad data. A similar behavior was also observed in the case of the chiral condensate, as discussed in Sec. IV A.

The cutoff dependence between the HISQ/tree, asqtad and continuum stout data is significantly reduced when f_K is used to set the scale as shown in Fig. 14(right). The change in the HISQ/tree data is small as the scales determined from r_1 and f_K are similar. The difference in the scales from the two observables is larger for the asqtad action at these lattice spacings and using f_K mostly shifts the $N_\tau = 8$ data. The difference in the position of the peak between the three actions also decreases, whereas the height of the peak and the value in the low temperature region show significant differences between the stout and HISQ/tree (or asqtad) actions. Since $\chi_R(T)/T^4$ is a renormalization group invariant quantity, the only reason for the difference should be the different values of the light quark mass: $m_l/m_s = 0.05$ for the HISQ/tree estimates versus 0.037 for the stout data. $O(N)$ scaling, discussed in Sec. III, suggests that the peak height should scale as $h^{1/\delta-1} \sim m_l^{-0.8}$. Applying this factor to the stout data reduces the peak height from ~ 40 to ~ 31.5 . Similarly, two corrections need to be applied to the asqtad data. First, a factor of $1/1.44$ to undo the multiplication by a heavier m_s^2 and the second, a multiplication by a factor of 1.2 to scale the susceptibility to the common light quark mass. After making these adjustments to normalize all three data sets to $m_l/m_s = 0.05$, we find that the HISQ/tree, asqtad and stout data are consistent.

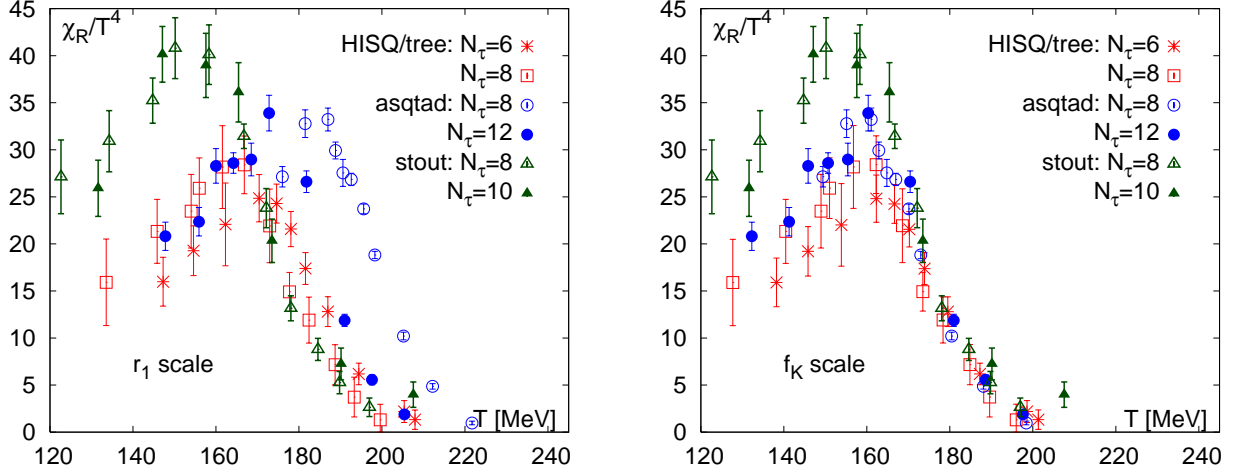


Figure 14: The renormalized two-flavor chiral susceptibility χ_R for the asqtad and HISQ/tree actions obtained at $m_l = 0.05m_s$ and compared with the stout action results [22]. The temperature scale is set using r_1 (f_K) in the left (right) panels.

V. $O(N)$ SCALING AND THE CHIRAL TRANSITION TEMPERATURE

A. The transition temperature using the p4 action

In this section, we use the universal properties of the chiral transition to define the transition temperature and its quark mass dependence for sufficiently small quark masses, as discussed in Sec. III. The scaling analysis of the chiral condensate leads to a parameter free prediction for the shape and magnitude of the chiral susceptibility. In the vicinity of the chiral limit, the peak in the chiral susceptibility corresponds to the peak in the scaling function $f_\chi(z)$ and the quark mass dependence of the pseudocritical temperature T_c is controlled entirely by the universal $O(N)$ scaling behavior. Keeping just the leading term proportional to a_1 in the regular part, the position of the peak in $\chi_{m,l}$ is determined from Eq. (16) using

$$\frac{\partial}{\partial T} \left(\frac{m_s^2 \chi_{m,l}(t, h)}{T^4} \right) = \frac{1}{h_0 t_0 T_c^0} h^{1/\delta-1-1/\beta\delta} \frac{d}{dz} f_\chi(z) + \frac{a_1}{T_c^0} = 0, \quad (35)$$

which, for zero scaling violation term, *i.e.*, $a_1 = 0$, gives the position of the peak in the scaling function f_χ at $z = z_p$ (see Sec. III). The strange quark mass on the left hand side is included only for consistency as the derivative is taken keeping it constant. For small light quark masses, we can expand $f_\chi(z)$ around z_p :

$$f_\chi(z) = f_\chi(z_p) + A_p(z - z_p)^2. \quad (36)$$

In this approximation, the location of the maximum in the chiral susceptibility varies as

$$z = z_p - \frac{a_1 t_0 h_0}{2A_p} h^{1-1/\delta+1/\beta\delta}, \quad (37)$$

and the variation of the pseudocritical temperature as a function of the quark mass is given by

$$\begin{aligned} T_c(H) &= T_c^0 + T_c^0 \frac{z_p}{z_0} H^{1/\beta\delta} \left(1 - \frac{a_1}{2A_p z_p z_0 h_0^{-1/\delta}} H^{1-1/\delta+1/\beta\delta} \right) \\ &= T_c^0 + T_c^0 \frac{z_p}{z_0} H^{1/\beta\delta} \left(1 - \frac{a_1 t_0^\beta}{2A_p z_p z_0^{1-\beta}} H^{1-1/\delta+1/\beta\delta} \right). \end{aligned} \quad (38)$$

Recall that T_c^0 is the transition temperature in the chiral limit. Thus, to determine the pseudocritical temperatures $T_c(H)$, we need to perform fits to the chiral condensate M_b , defined in Eqs. (12) and (13), to determine the parameters T_c^0 , z_0 , t_0 , a_0 , a_1 and a_2 in the scaling and regular terms. Theoretically, one expects the $O(4)$ Ansatz to describe the

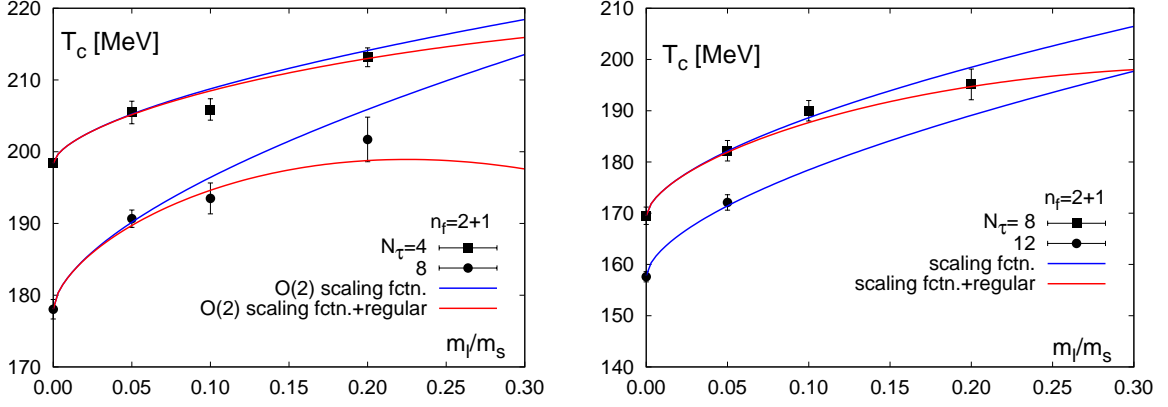


Figure 15: Estimates of pseudocritical temperature determined from the peak in the disconnected susceptibility with the p4 action on lattices of temporal extent $N_\tau = 4$ and 8 (left). Results for $m_s/m_l < 0.05$ will be presented elsewhere. Curves show results obtained from the $O(2)$ scaling fits to the chiral condensate without (blue) and with (red) scaling violation terms included. The right hand figure shows the corresponding analysis for the asqtad action.

critical behavior in the continuum limit; however, $O(2)$ scaling is more appropriate for calculations with staggered fermions at non-zero values of the cutoff. Fits are, therefore, performed using both the $O(2)$ and $O(4)$ scaling functions in all cases.

Performing universal $O(N)$ scaling fits to extract reliable estimates of the chiral transition temperature as a function of the light quark masses requires making choices for the range of data points (temperature values) to include and the number of terms needed to model the regular part. To test these issues numerically, we use the extensive data with the p4 action on lattices with $N_\tau = 4$ and 8 and light quark masses down to $m_l/m_s = 1/80$ [64, 69, 76]. In Fig. 15(left), we compare scaling results for $T_c(H)$ as a function of the light quark mass, $H = m_l/m_s$, with direct determination of the peak in the disconnected part of the chiral susceptibility obtained using Gaussian and cubic fits to the data in the peak region. We find that the scaling fits reproduce the quark mass dependence of $T_c(H)$ for $m_l/m_s \lesssim 1/20$, which covers the physical point $m_l/m_s \simeq 1/27$. For larger quark masses, scaling violation terms have to be taken into account. The range of temperature values included in these fits (defining the scaling window) is 15–20 MeV.

Having demonstrated that the scaling analysis works for the p4 action, we apply this approach to the asqtad and HISQ/tree actions even though the range of quark masses explored is smaller and the coverage of the transition region (values of T simulated) is not as dense, so a larger T range will be used.

B. Scaling analysis for the asqtad and HISQ/tree action

The scaling analysis of the HISQ/tree ($N_\tau = 6, 8$ and 12 lattices) and asqtad actions ($N_\tau = 8$ and 12 lattices) was performed in steps due to the limited number of m_l/m_s and temperature values simulated compared to the p4 action discussed in Sec. V A. In the case of the HISQ/tree action, having data at $m_l/m_s = 1/20$ and $1/40$ on $N_\tau = 6$ and $N_\tau = 8$ lattices allowed us to test the range of validity of the scaling fits in the region bracketing the physical light quark mass. The scaling Ansatz included both the singular and regular parts defined in Eqs. (14) and (35) in terms of the six parameters $T_c^0, z_0, t_0, a_0, a_1$ and a_2 . We find that a best fit to the $m_l/m_s = 1/40$ data for M_b also fits the $m_l/m_s = 1/20$ data; in addition, the chiral susceptibility derived from this fit matches the measurements at $m_l/m_s = 1/20$. We, therefore, conclude that the scaling extends to $m_l/m_s = 1/20$.

To get the value of T_c , we then carried out a simultaneous fit to the chiral condensate at the two values of m_l/m_s and its derivative, the total chiral susceptibility, at $m_l/m_s = 1/20$. (The calculation of the connected part of the susceptibility at $m_l/m_s = 1/40$ is not complete, so we could not include these data.) The range of temperature values selected for the three data sets was independently adjusted to minimize the χ^2/dof and, at the same time, include as many points as possible in the region of the peak in the susceptibility. We also varied the relative weight assigned to points along the two LCPs and for our final fits decreased the weight given to the heavier $m_l/m_s = 1/20$ points by a factor of sixteen in the calculation of the χ^2 . (This was done because the scaling Ansatz with a truncated regular piece is expected to get progressively worse as the mass increases, whereas the statistical errors in M_b are roughly a factor of two smaller at the heavier mass.) In all these fits we find that while the height of the peak in the susceptibility is sensitive to what points are included in the fits and the relative weighting of the points along the two LCP, the

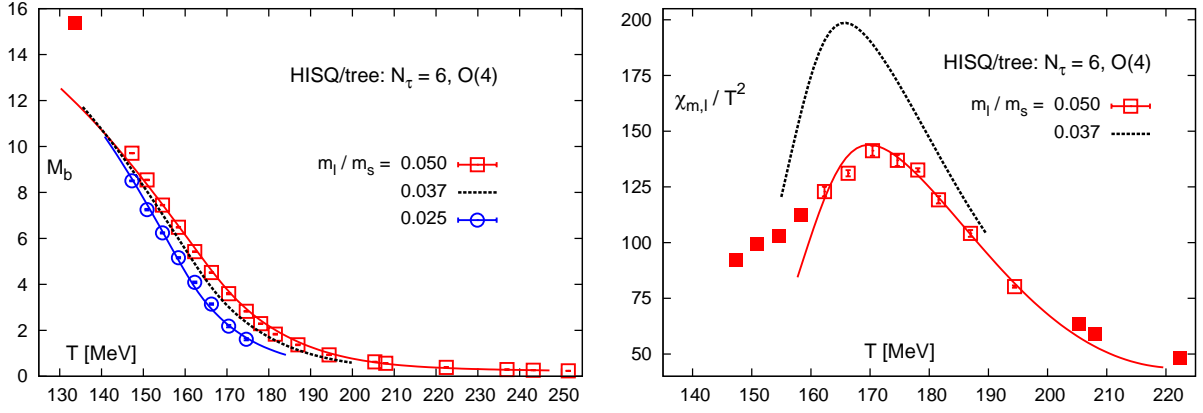


Figure 16: Scaling fits and data for the chiral condensate M_b calculated with the HISQ/tree action on lattices with temporal extent $N_\tau = 6$ (left) and the chiral susceptibility $\chi_{m,l}$ (right). The data for M_b at $m_l/m_s = 0.025$ and for M_b and $\chi_{m,l}$ at $m_l/m_s = 0.05$ are fit simultaneously using the $O(4)$ scaling Ansatz. The fits using the $O(2)$ Ansatz are similar. The points used in the scaling fits are plotted using open symbols. The dotted lines give the data scaled to the physical quark masses.

location of the peak does not vary by more than 0.3 MeV for any reasonable set of choices. Repeating the analysis with just the $m_l/m_s = 1/40$ or the $m_l/m_s = 1/20$ data did not change the estimates of T_c significantly. We therefore conclude that $m_l/m_s = 1/20$ lies within the range of validity of our scaling Ansatz. Confirming that $m_l/m_s = 1/20$ lies within the scaling window is important for our analysis because simulations on the $N_\tau = 12$ lattices have been done only at this LCP for both the HISQ/tree and asqtad actions.

The most challenging part of determining the best fit was including a sufficient number of points below the location of the peak in $\chi_{m,l}$. This is evident from Figs. 16–19 which show that the fits rapidly deviate from the $\chi_{m,l}$ data below the location of the peak. In most cases, only two points below the peak could be included in the fits.

The χ^2/dof of these fits are not good. For the $O(4)$ fits they are 96/12 and 30/12 for the asqtad data on $N_\tau = 8$ and 12 lattices; and 430/28, 125/26 and 70/14 for the $N_\tau = 6, 8$ and 12 HISQ/tree data, respectively. (The χ^2/dof for the $O(2)$ fits is about 20% larger for the $N_\tau = 6$ and 12 HISQ/tree data and comparable for the others.) These large χ^2/dof reflect the fact that the statistical errors in M_b are small and do not include the systematic errors due to fluctuations in points along the LCP coming from less than perfect tuning of m_s (or T), and partly because we have used a truncated form for the regular part of the free energy. We attempted various truncations of the regular part and found that the variation in the location of the peak is negligible and insensitive to the number of parameters included in the fits. Note that the location of the peak and its scaling with m_l/m_s are the only quantities we extract from the fits. Overall, we find that the fits using the $O(4)$ scaling Ansatz are more stable with respect to variation of the fit range. We, therefore, use estimates from the $O(4)$ fits to obtain our final results for T_c which are about 2 MeV lower than those with the $O(2)$ Ansatz. Fits to the HISQ/tree data are shown in Figs. 16, 17 and 18 for $N_\tau = 6, 8$ and 12, respectively.

The above analysis using simultaneous fits to data for the order parameter M_b and the total chiral susceptibility χ was repeated for the asqtad action on $N_\tau = 8$ lattices with the two LCP at $m_l/m_s = 1/20$ and $1/10$. We failed to find a fit that reproduced the data for the chiral susceptibility at the heavier mass. We conclude that $m_l/m_s = 1/10$ is not within the scaling region and restrict the simultaneous fit to just data with $m_l/m_s = 1/20$. Fits to the $N_\tau = 12$ lattices for both the asqtad and HISQ/tree lattices are made at the single value of $m_l/m_s = 1/20$ where simulations were carried out. Our best fits to the $N_\tau = 12$ asqtad data are shown in Fig. 19 for the $O(4)$ Ansatz.

The final value of T_c is calculated by finding the location of the peak in the susceptibility. Errors on T_c for each action and N_τ value are estimated by carrying out the entire analysis for 400 synthetic samples. Each point in these samples is taken from a Gaussian distribution with mean and standard deviation given by the central value and the quoted errors on the data points. Once the scaling function is determined, we can extract T_c at any desired value of m_l/m_s . Our final results at $m_l/m_s = 1/20$ and at the physical quark masses (defined as $m_l/m_s = 0.037$ with m_s tuned to its physical value) are summarized in Table I. For the asqtad data, we extrapolate to $m_l/m_s = 0.0296$ to partially correct for the fact that m_s on the LCP is about 20% heavier than the physical value. Changing the extrapolation point provides estimates at the correct physical light quark mass but does not correct for the heavier strange quark mass, so we expect the asqtad results to overestimate T_c . A final point, these estimates are also consistent with the location of the peak in $\chi_{l, \text{disc}}$ as shown in Figs. 10 and 11 and discussed in Sec. IV B 1.

The last step in the determination of T_c is to extrapolate estimates at the physical value of m_l/m_s obtained at

different N_τ to the continuum limit. With two asqtad data points and three HISQ/tree points, we explored all possible combinations of linear and quadratic fits to the data for each action and combined fits to the asqtad and HISQ/tree data in which the intercept (continuum value) is constrained to be the same for the two actions. The results of individual extrapolations linear in $1/N_\tau^2$ for the asqtad data and quadratic for the HISQ/tree data are given in rows marked ∞ in Table I. The results of a combined quadratic fit are given in the final row marked “ ∞ (asqtad+HISQ/tree)”. Two examples of combined fits are shown in Fig. 20. In Fig. 20(left) we show the result of a combined fit linear in the asqtad data and quadratic in the HISQ/tree data, while the combined quadratic fit to both data sets is shown in Fig. 20(right).

We take the result, $T = 154(8)$ MeV, of the quadratic fit with the $O(4)$ Ansatz to the HISQ/tree data as our best estimate. These fits are less sensitive to variations in the range of temperature selected. The estimate from the $O(2)$ fits is about 2 MeV higher as shown in Table I. Since the quadratic fit to just the HISQ/tree data is identical to the fit shown in Fig. 20(right) we do not show it separately. For both $O(2)$ and $O(4)$ Ansätze, we find that the range of variation of the central value of the various fits is about 5 MeV, so 8 MeV is a conservative estimate of the combined statistical and systematic error and includes the full range of variation. Note that the error estimates, as expected, increase significantly for quadratic fits compared to linear fits, because in this case there are as many parameters as data points. In all these fits χ^2 is much less than one. Furthermore, when the error bars on individual points do not represent normally distributed statistical errors and there are one or zero degrees of freedom, chi-square is not a useful guide for selecting the best fit.

In determining this final estimate, we have mostly used the asqtad data as confirmatory for two reasons. First, the slope of the fits to the asqtad data is 2–2.5 times that in the HISQ/tree fits and the undetermined quadratic term may be large. Note that the large slope confirms our discussion in Sec. II that the discretization errors in the asqtad formulation are larger. Second, the LCP defined by the strange quark mass is $\approx 20\%$ heavier than the physical value, so the asqtad action data overestimate T_c .

In addition to the above error estimate, there is a 1 MeV uncertainty in the setting of the temperature scale as discussed in Sec. II which will shift all estimates. We therefore quote it as an independent error estimate. Thus, our result after continuum extrapolation, and at the physical light quark masses, $m_l/m_s = 1/27$, is $T_c = (154 \pm 8 \pm 1)$ MeV. To obtain an overall single error estimate we add the uncertainty in the scale coming from r_1 to the statistical and systematic errors. Thus, our final estimate is

$$T_c = (154 \pm 9) \text{ MeV}. \quad (39)$$

C. Comparison with previous results

We compare the result in Eq. (39) with three previous 2 + 1 flavor studies that also extrapolated T_c data to the continuum limit and to the physical light quark mass. It should be emphasized that in our previous work [20] such an extrapolation was not carried out.

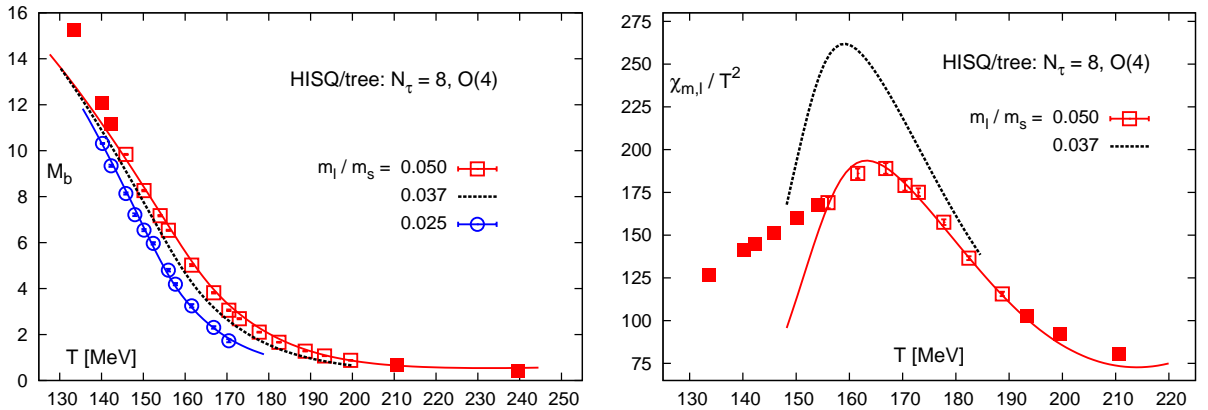


Figure 17: Scaling fits and data for the chiral condensate M_b calculated with the HISQ/tree action on lattices with temporal extent $N_\tau = 8$ (left) and the chiral susceptibility $\chi_{m,l}$ (right). The data for M_b at $m_l/m_s = 0.025$ and for M_b and $\chi_{m,l}$ at $m_l/m_s = 0.05$ are fit simultaneously using the $O(2)$ scaling Ansatz. The fits using the $O(4)$ Ansatz are similar. The points used in the scaling fits are plotted using open symbols. The dotted lines give the data scaled to the physical quark masses.

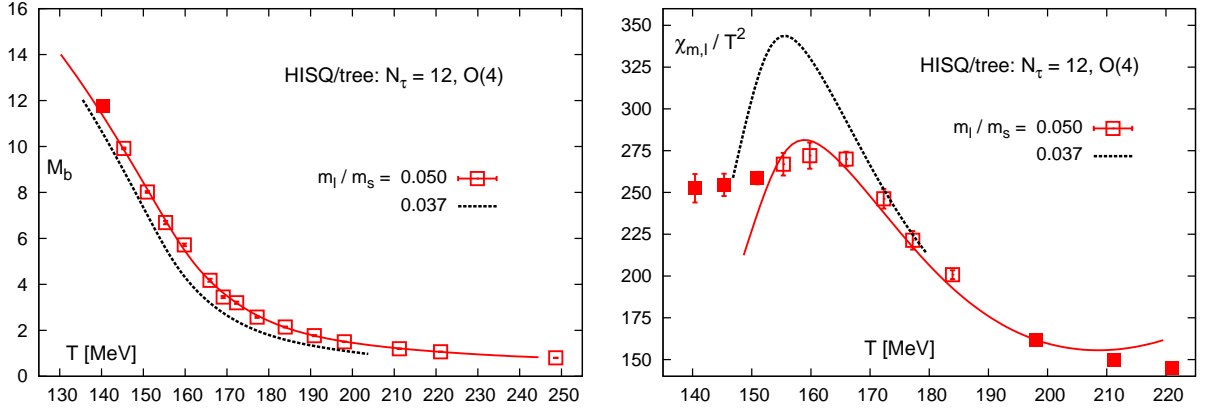


Figure 18: Scaling fits and data for the chiral condensate M_b calculated with the HISQ/tree action on lattices with temporal extent $N_\tau = 12$ (left) and the chiral susceptibility $\chi_{m,l}$ (right). The data for M_b and $\chi_{m,l}$ at $m_l/m_s = 0.05$ are fit simultaneously using the $O(4)$ scaling Ansatz. The fits using the $O(2)$ Ansatz are similar. The points used in the scaling fits are plotted using open symbols. The dotted lines give the data scaled to the physical quark masses.

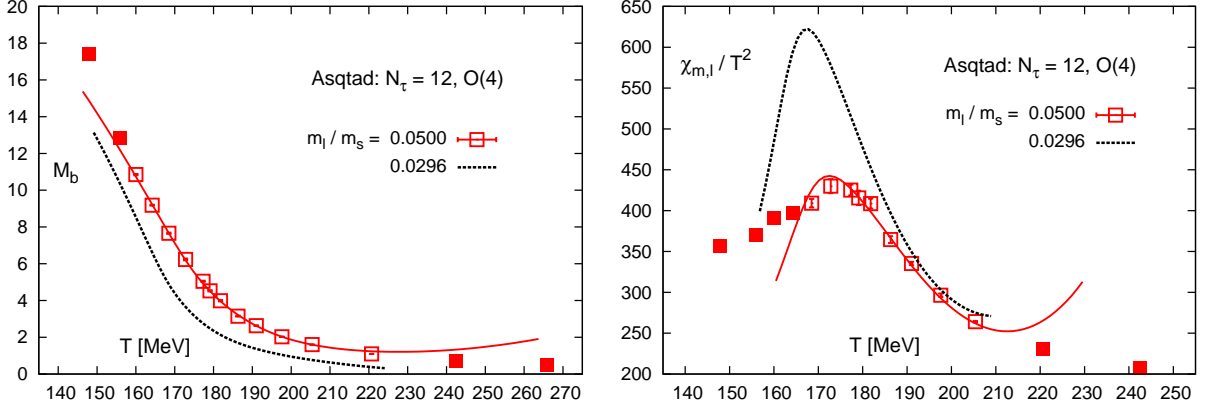


Figure 19: Scaling fits and data for the chiral condensate M_b calculated with the asqtad action on lattices with temporal extent $N_\tau = 12$ (left) and the chiral susceptibility $\chi_{m,l}$ (right). The data for M_b and $\chi_{m,l}$ at $m_l/m_s = 0.05$ are fit simultaneously using the $O(4)$ scaling Ansatz. The fits using the $O(2)$ Ansatz are similar. The points used in the scaling fits are plotted using open symbols. The dotted lines give the data scaled to the physical quark masses.

The 2004 study by the MILC collaboration used the asqtad action [10]. They extrapolated T_c defined as the peak position in the total chiral susceptibility using an expression that incorporated the $O(4)$ critical exponent. They found $T_c = 169(12)(4)$ in the chiral limit, which is just consistent, within errors, with our current result. Note, however, that the present data are more extensive and the scaling analysis is more comprehensive.

The RBC-Bielefeld collaboration studied the p4 action on $N_\tau = 4$ and 6 lattices with several values of the light quark masses [11]. The result of a combined extrapolation in the quark mass and $1/N_\tau^2$ gave $T_c = 192(7)(4)$ MeV. This value is significantly higher than the one given in Eq. (39). Based on analyses done subsequently, and the new data on $N_\tau = 8$ lattices presented here, we find that this discrepancy is due to an underestimate of the slope of the linear fit, T_c vs. $1/N_\tau^2$. The change in the slope between $N_\tau = 4$ and 6 data and $N_\tau = 6$ and 8 data is shown in Fig. 21. To perform a continuum extrapolation of T_c obtained with the p4 action requires new calculations on lattices with $N_\tau \geq 12$. Having demonstrated that the discretization errors are similar for the p4 and asqtad actions and given the consistency between results obtained with the HISQ/tree, asqtad and stout actions, we do not intend to pursue further calculations with the p4 action.

Lastly, the Wuppertal-Budapest collaboration has carried out a continuum extrapolation using the stout action on $N_\tau = 6, 8$, and 10 lattices, and more recently including $N_\tau = 12$ and 16 lattices [22–24]. They work directly at $m_l/m_s = 0.037$ and perform a linear extrapolation in $1/N_\tau^2$ of their data to obtain continuum estimates. From

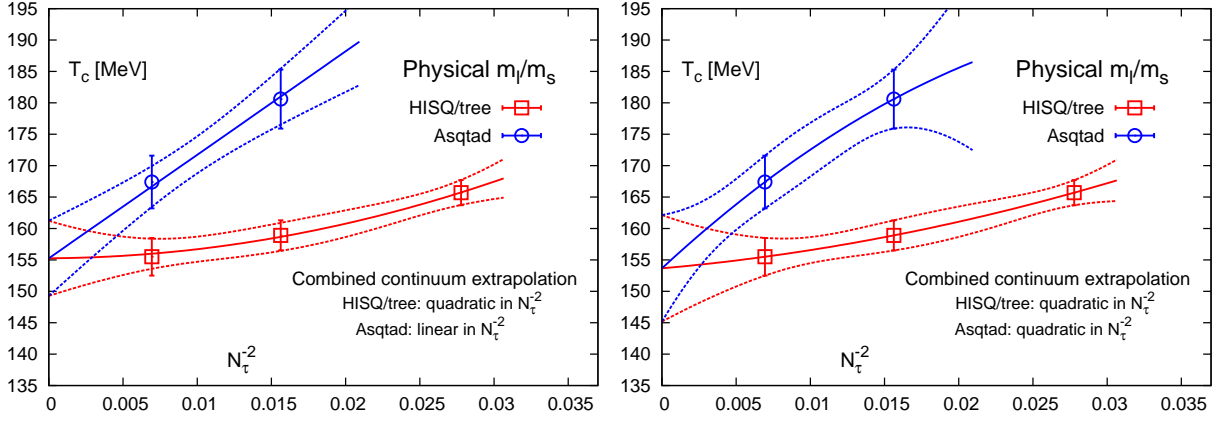


Figure 20: The data and the continuum extrapolation of the transition temperature obtained from the $O(4)$ scaling analysis for m_l/m_s extrapolated to the physical value. The left figure shows a combined fit using a linear extrapolation to the asqtad data and a quadratic to the HISQ/tree data. The right figure shows a combined quadratic fit to both data sets.

N_τ	$T_c, O(4)$ $m_l/m_s = 1/27$	$T_c, O(2)$ $m_l/m_s = 1/27$	$T_c, O(4)$ $m_l/m_s = 1/20$	$T_c, O(2)$ $m_l/m_s = 1/20$
8 (asqtad)	180.6(4.7)	181.9(3.2)	184.5(4.4)	185.0(3.4)
12	167.4(4.2)	170.1(3.1)	172.5(3.9)	174.0(2.9)
∞	156.8(8.4)	160.7(6.1)	162.9(7.9)	165.2(5.9)
6 (HISQ/tree)	165.7(2.0)	167.7(2.3)	169.8(2.0)	171.3(2.1)
8	158.9(2.4)	160.6(1.6)	163.1(2.7)	164.1(1.8)
12	155.5(3.0)	157.4(3.0)	158.9(2.7)	160.9(2.1)
∞	153.7(8.4)	156.0(7.8)	155.9(8.2)	159.5(6.1)
∞ (asqtad + HISQ/tree)	153.7(8)	156.0(8)	155.9(8)	159.5(6)

Table I: Pseudocritical temperature T_c determined from $O(2)$ and $O(4)$ scaling fits to the chiral condensate and the chiral susceptibility. The results are shown at $m_l/m_s = 0.05$ at which simulations have been performed for all three values of N_τ and at the physical value of m_l/m_s . The temperature scale used in the fits is set using r_1 . Rows labeled ∞ give results after a linear extrapolation to the continuum for the asqtad data and quadratic for the HISQ data. The last row gives the results of a combined fit using an extrapolation quadratic in $1/N_\tau^2$, which coincides with the extrapolation of just the HISQ/tree data.

the position of the peak in the renormalized chiral susceptibility they extract $T_c = 147(2)(3)$ MeV. This value is approximately 1σ lower than our result. They also report higher transition temperatures of $T_c = 157(3)(3)$ and $155(3)(3)$ derived from inflection points in $\Delta_{l,s}$ and $\langle\bar{\psi}\psi\rangle_R$ respectively. As discussed in Sec. III and confirmed by the significant difference in their three estimates, using inflection points is a less sensitive probe of the critical behavior, and thus less reliable for extracting T_c . By making simultaneous fits to the chiral condensate and the susceptibility, and defining the transition temperature as the peak in the susceptibility, our analysis overcomes this ambiguity.

VI. QUARK NUMBER SUSCEPTIBILITIES AND THE POLYAKOV LOOP

In this section, we present our results for light and strange quark number susceptibilities as well as the Polyakov loop expectation value. In Sec. III, we stated that we do not use these observables for the determination of the QCD transition temperature because the singular part of the free energy, which drives the chiral transition, is subleading in the quark number susceptibilities and thus difficult to isolate. Similarly, in the case of the Polyakov loop expectation value, a direct relation to the critical behavior has not been established. Nonetheless, we study these observables as they provide important insight into the deconfining aspects of the QCD transition.

The discussion in Sec. III shows that quark number susceptibilities probe whether the relevant degrees of freedom of the system at a given temperature are hadronic or partonic; a rapid rise in the quark number susceptibilities signals the increasing contribution of light (partonic) degrees of freedom. Theoretically, the reduced temperature

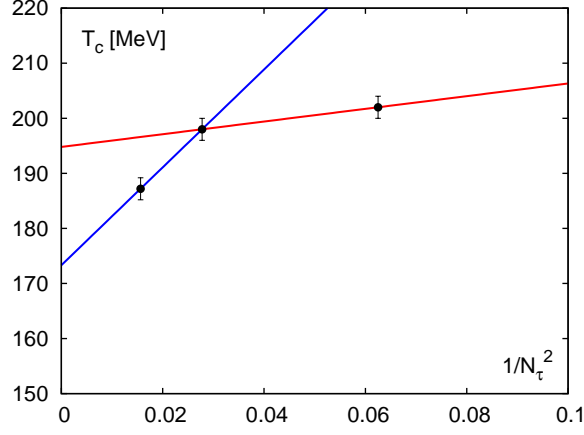


Figure 21: Linear extrapolations to the continuum limit of T_c data for the p4 action. The fit to the $N_\tau = 4$ and 6 data is shown in red, while that to the $N_\tau = 6$ and 8 points is in blue. The two fits illustrate the change in the slope as N_τ is increased.

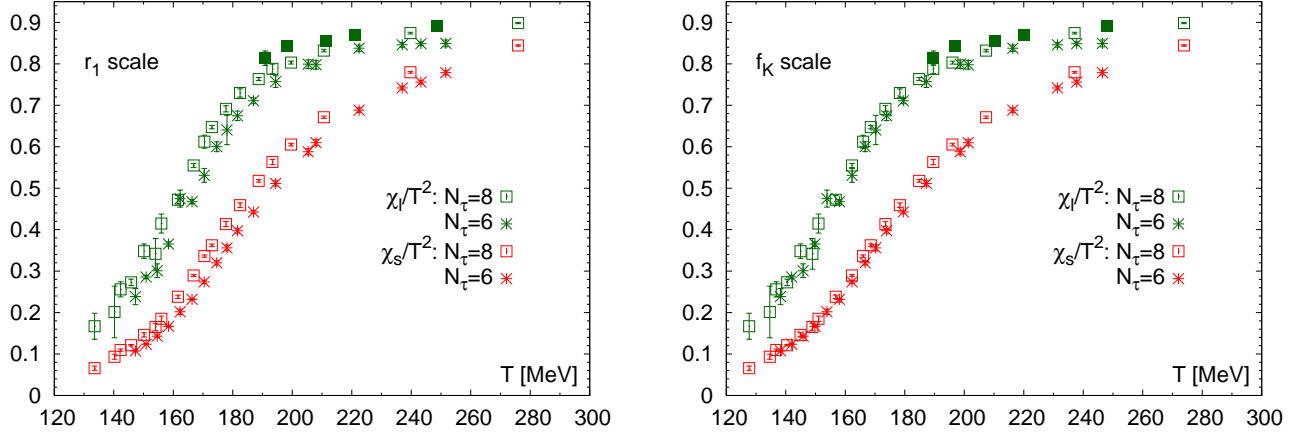


Figure 22: Light quark number susceptibility for the HISQ/tree action with $m_l/m_s = 1/20$ are compared with the strange quark number susceptibility. In the left panel r_1 is used to set the lattice scale, while in the right panel f_K is used. The filled squares correspond to $N_\tau = 12$.

t defined in Eq. (10) is symmetric in the light and strange flavors at leading order, therefore, the structure of the singular contribution to both observables is similar and should differ only in magnitude. We compare the temperature dependence of χ_l and χ_s on $N_\tau = 6$ and 8 lattices in Fig. 22 and find a similar behavior with χ_l exhibiting a more rapid rise at temperatures closer to the chiral transition temperature. From these data, one would be led to conclude that χ_l and χ_s are probing the singular part of the free energy and deduce a higher transition temperature from χ_s than from χ_l . However, in Sec. III we pointed out that the temperature dependence of these observables, even in the chiral limit, is dominated by the regular part of the free energy. This feature is highlighted by the difference in the temperature dependence of χ_l and χ_s versus that of the chiral condensate, shown in Fig. 8, which is dominated by the singular part in the chiral limit. Thus, even though the data in Fig. 22 show a rapid crossover, extracting information about the singular part from them is nontrivial, and consequently the determination of T_c from these observables is less reliable.

In Fig. 22, we also compare the temperature dependence of χ_l and χ_s using r_1 and f_K to set the temperature scale. Both light and strange quark number susceptibilities show a much smaller cutoff dependence when using the f_K scale. A similar behavior was observed for the chiral susceptibility as discussed in Sec. IV B.

In order to analyze further the cutoff dependence and to compare our data with the continuum extrapolated stout results [24], we examine the strange quark number susceptibility, which is statistically under better control. In Fig. 23, we show χ_s/T^2 for $m_l = 0.05m_s$ calculated with the HISQ/tree and asqtad actions. The larger cutoff effects are in the asqtad data. We also plot the data using f_K to set the temperature scale and find that all data collapse into

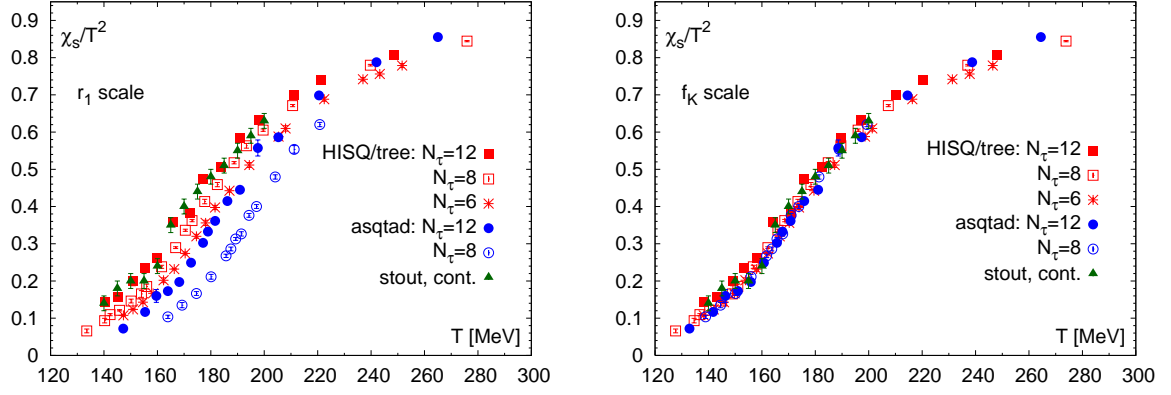


Figure 23: Data for the strange quark number susceptibility for $m_l = 0.05m_s$ with the asqtad and HISQ/tree actions are compared to the continuum extrapolated stout results [24]. In the right panel, we show that all the data collapse to a single curve when f_K is used to set the temperature scale.

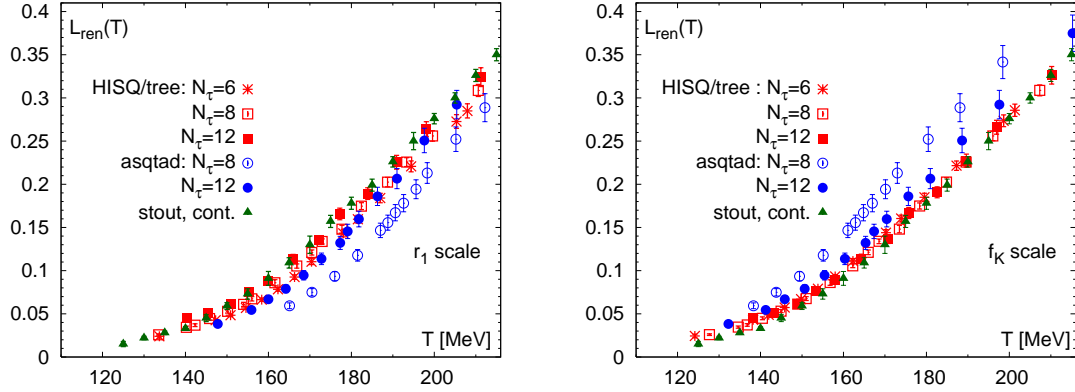


Figure 24: The renormalized Polyakov loop calculated for the asqtad and HISQ/tree actions and compared with the continuum extrapolated stout result [24]. In the right panel, we show the same data using f_K to set the scale.

one curve as shown in Fig. 23(right), suggesting that the discretization errors in χ_s and f_K are very similar. On the basis of this agreement, we conclude that the differences in results for χ_s seen in Fig. 23(left) are accounted for by discretization errors.

The Polyakov loop is a sensitive probe of the thermal properties of the medium even though it is not a good measure of the critical behavior as discussed in Sec. III. After proper renormalization, the square of the Polyakov loop characterizes the long distance behavior of the static quark anti-quark free energy; it gives the excess free energy needed to screen two well separated color charges. The renormalized Polyakov loop $L_{ren}(T)$ has been studied in the past in the pure gauge theory [77, 78] as well as in QCD with two [79], three [80] and two plus one flavors of quarks [19, 20]. Following Ref. [22] $L_{ren}(T)$, for a given N_τ , is obtained from the bare Polyakov loop defined in Eq. (22) as

$$L_{ren}(T) = \exp(-N_\tau c(\beta)/2) L_{bare}, \quad (40)$$

where the renormalization constant $c(\beta)$ is deduced from the heavy quark potential discussed in Sec. II.

We compare results for $L_{ren}(T)$ from the asqtad, HISQ/tree and stout actions in Fig. 24 to determine the cutoff effects in the description of basic thermal properties, *e.g.*, in the asymptotic long distance structure of a heavy quark free energy and the screening of the quark-antiquark force. We find significant cutoff effects in L_{ren} with the asqtad action; however, these are considerably smaller than seen in the other quantities discussed so far. This is partially expected as the Polyakov loop is a purely gluonic observable and is thus less affected by the taste symmetry breaking in the staggered formulations. In Fig. 24(right), we also show the temperature dependence of L_{ren} when f_K is used to set the scale. For the HISQ/tree action, the already small cutoff effects are further reduced and the data move even closer to the continuum extrapolated stout result. For the asqtad data, on the other hand, the N_τ dependence is slightly more pronounced. The more remarkable feature is the switch in the approach to the continuum limit; it is

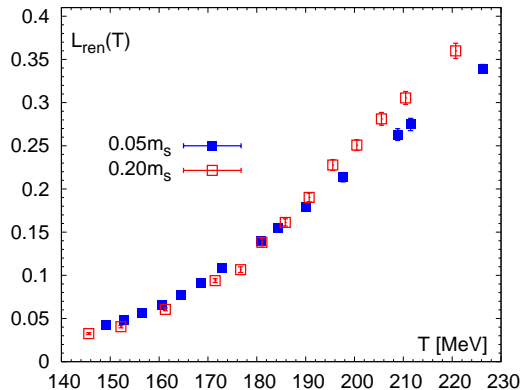


Figure 25: The renormalized Polyakov loop for the HISQ/tree action on $N_\tau = 6$ lattices for two values of the light quark mass $m_l/m_s = 0.05$ and 0.20 .

from above when f_K is used to set the temperature scale and from below when using the r_1 scale. This is similar to what has been observed in calculations with the stout action on coarser lattices [22]. Such behavior is not surprising, as there is no obvious reason for cutoff effects in a hadronic observable like f_K and a gluonic observable like L_{ren} to be related so that there is a cancellation of lattice artifacts in their ratio. Based on these observed changes with N_τ and dependence on whether the scale is set by r_1 or f_K , we expect that the asqtad action will need L_{ren} data on $N_\tau > 12$ lattices to agree with the continuum extrapolated HISQ/tree and stout data. This confirms the statement made in Sec. II that while asqtad and the HISQ actions are equivalent at order $\mathcal{O}(\alpha_s a^2)$ the difference at higher orders makes sizeable contributions below $N_\tau \sim 12$. Overall, we conclude that once discretization effects are accounted for, the Polyakov loop measured using different staggered discretization schemes yields consistent estimates of the thermal properties of the theory.

Lastly, we briefly discuss the quark mass dependence of the Polyakov loop. In Fig. 25, we show the renormalized Polyakov loop for two quark masses $m_l/m_s = 0.05$ and 0.20 on $N_\tau = 6$ HISQ/tree ensembles. The quark mass dependence is small in the transition region, and at higher temperatures the renormalized Polyakov loop rises faster for the heavier quark mass. This dependence on the quark mass is consistent with the results obtained using the p4 action [21]. Previous work suggests that for larger values of the light quark masses, $m_l > 0.2m_s$, the quark mass dependence becomes more significant as L is influenced by the phase transition in the pure gauge theory [80].

VII. CONCLUSIONS

In this paper, we present results for the chiral and deconfinement aspects of the QCD transition using three improved staggered quark actions called p4, asqtad and HISQ/tree. The chiral transition is studied using the chiral condensate and the chiral susceptibility, while the deconfining aspects of the transition have been addressed using the quark number susceptibilities and the renormalized Polyakov loop. By comparing the results obtained at different lattice spacings, we analyze the cutoff dependence of these quantities, in particular, the effects due to taste symmetry breaking. We find that the effects of taste symmetry breaking are significantly reduced in the HISQ/tree action. After demonstrating control over systematic errors, we compare our data with the continuum extrapolated stout results and find agreement for all quantities.

We analyze the chiral transition in terms of universal $O(N)$ scaling functions using simulations performed at several values of the light quark mass and N_τ . We show that for $m_l/m_s < 0.1$ the corrections to scaling are small and determine the critical temperature in the 2-flavor (degenerate u and d quarks) chiral limit. We define the pseudocritical temperature T_c at non-zero values of the light quark mass, in particular the physical value $m_l/m_s = 1/27$, as the peak in the total chiral susceptibility. We find that this definition of the pseudocritical temperature gives estimates consistent with those obtained from the location of the peak in the disconnected chiral susceptibility used in previous studies. Our final result, after extrapolation to the continuum limit and for the physical value of light quarks, $m_l/m_s = 1/27$, is $T_c = (154 \pm 9)\text{MeV}$ based on the analysis summarized in Table I.

The Wuppertal-Budapest collaboration has extracted T_c using the inflection point in the data for the chiral condensate and the peak in the chiral susceptibility. In their most recent publication [24], they quote values ranging from 147 to 157 MeV depending on the chiral observable. While their methods for extracting T_c differ, their values

are, within errors, in agreement with our determination. The consistency of the results obtained with the HISQ/tree, asqtad and stout actions shows that these results represent the continuum limit value for the staggered formulation.

Finally, we also consider it interesting to determine the pseudocritical temperature in terms of other scaling functions, namely the scaling functions related to the mixed susceptibility, Eq. (18), and the specific heat. This would allow estimation of the intrinsic uncertainty in defining the pseudocritical temperature at nonzero values of the light quark mass where, *a priori*, it can depend on the probe used to estimate it. We will address this issue in future work.

Acknowledgments

This work has been supported in part by contracts DE-AC02-98CH10886, DE-AC52-07NA27344, DE-FG02-92ER40699, DE-FG02-91ER-40628, DE-FG02-91ER-40661, DE-FG02-04ER-41298, DE-KA-14-01-02 with the U.S. Department of Energy, and NSF grants PHY08-57333, PHY07-57035, PHY07-57333 and PHY07-03296, the Bundesministerium für Bildung und Forschung under grant 06BI9001, the Gesellschaft für Schwerionenforschung under grant BILAER and the Deutsche Forschungsgemeinschaft under grant GRK881, and the EU Integrated Infrastructure Initiative HadronPhysics2. The numerical simulations have been performed on BlueGene/L computers at Lawrence Livermore National Laboratory (LLNL), the New York Center for Computational Sciences (NYCCS) at Brookhaven National Laboratory, on BlueGene/P computers at NIC, Juelich, US Teragrid (Texas Advanced Computing Center), and on clusters of the USQCD collaboration in JLab and FNAL. We thank Claude Bernard for help with the determination of the scale for the asqtad action using f_K .

β	$m_l = 0.05m_s$			$m_l = 0.10m_s$			$m_l = 0.20m_s$		
	m_l	m_s	$2 \times TU_T$	m_l	m_s	$2 \times TU_T$	m_l	m_s	$2 \times TU_T$
3.4900	0.001450	0.0290	31680	—	—	—	—	—	—
3.5000	0.001265	0.0253	32520	—	—	—	—	—	—
3.5100	0.001300	0.0260	30050	—	—	—	—	—	—
3.5150	0.001200	0.0240	30480	—	—	—	0.00480	0.0240	3510
3.5200	0.001200	0.0240	39990	0.00240	0.0240	11800	0.00480	0.0240	6470
3.5225	0.001200	0.0240	54610	0.00240	0.0240	30620	—	—	—
3.5250	0.001200	0.0240	64490	0.00240	0.0240	31510	—	—	—
3.5275	0.001200	0.0240	65100	0.00240	0.0240	28060	—	—	—
3.5300	0.001200	0.0240	70230	0.00240	0.0240	34420	0.00480	0.0240	24900
3.5325	—	—	—	0.00240	0.0240	27310	—	—	—
3.5350	0.001200	0.0240	39510	0.00240	0.0240	29250	0.00480	0.0240	4850
3.5375	—	—	—	0.00240	0.0240	30320	0.00480	0.0240	4890
3.5400	0.001200	0.0240	56740	0.00240	0.0240	31590	0.00480	0.0240	5190
3.5425	—	—	—	0.00240	0.0240	38520	0.00480	0.0240	4380
3.5450	0.001075	0.0215	20700	0.00240	0.0240	15060	0.00480	0.0240	5300
3.5475	—	—	—	—	—	—	0.00480	0.0240	4630
3.5500	—	—	—	—	—	—	0.00480	0.0240	5530
3.5525	—	—	—	—	—	—	0.00480	0.0240	22540
3.5550	—	—	—	—	—	—	0.00480	0.0240	23420
3.5600	0.001025	0.0205	11660	—	—	—	0.00480	0.0240	21230
3.5700	—	—	—	—	—	—	0.00480	0.0240	9250

Table II: Parameters used in simulations with the p4 action on $N_\tau = 8$ lattices and three lines of constant physics defined by $m_l/m_s = 0.2, 0.1$ and 0.05 . The quark masses are given in units of the lattice spacing a . The finite temperature runs were carried out on $32^3 \times 8$ lattices. The statistics are given in units of trajectories ($2 \times TU_T$) which are of length $\tau_{MD} = 0.5$.

Appendix A: Lattice parameters for p4, asqtad and HISQ/tree simulations

In this appendix, we provide details on the parameters used in the calculations with the p4, asqtad and HISQ/tree actions. These include the gauge couplings, quark masses and lattice sizes at which simulations were carried out and the collected statistics. In the following tables, TU_T stands for the molecular dynamics time units simulated for finite temperature runs and TU_0 for the corresponding zero temperature ones. In Table II, we give the parameters of the simulations with p4 action on $32^3 \times 8$ lattices. In Table III and Table IV, we give the simulation parameters for the asqtad action corresponding to $N_\tau = 8$ and $N_\tau = 12$ lattices, respectively. The parameters for the $N_\tau = 8$ ensemble with $m_l/m_s = 0.1$ runs are given in Ref. [20]. The details on the extraction of r_0 and r_1 are given in Sec. II C and in Appendix B.

For the HISQ/tree action, the $N_\tau = 6$ calculations with $m_l = 0.2m_s$ were done on $16^3 \times 32$ and $16^3 \times 6$ lattices for zero and finite temperature studies, respectively, and the run parameters are summarized in Table V.

The parameters of finite temperature simulations at $m_l = 0.05m_s$ for ensembles with $N_\tau = 6, 8$ and 12 and the corresponding zero temperature calculations are given in Table VI. For the $O(N)$ scaling analysis, we have also used the HISQ/tree data on $N_\tau = 6$ and 8 lattices at $m_l = 0.025m_s$ as summarized in Table VII. These data are part of the ongoing RBC-Bielefeld study of $O(N)$ scaling [76].

Data for the light and strange quark chiral condensate, disconnected and connected chiral susceptibility, the light and strange quark number susceptibility and the bare Polyakov loop on finite temperature ensembles for the asqtad action on $N_\tau = 8$ and 12 lattices are given in Tables VIII and IX. The corresponding data for the HISQ/tree action are given in Tables X, XI and XII for $N_\tau = 6, 8$ and 12 lattices, respectively.

For completeness, we also give the data for the light and strange quark chiral condensate on zero temperature ensembles for the asqtad action on $N_\tau = 8$ and 12 lattices in Table XIII. The corresponding data for the HISQ/tree action are given in Table XIV.

β	$m_l = 0.05m_s$					$m_l = 0.20m_s$			
	m_l	m_s	u_0	TU_0	TU_T	m_l	m_s	u_0	TU_T
6.5500	0.00353	0.0705	0.8594	—	29541	—	—	—	—
6.5750	0.00338	0.0677	0.8605	—	13795	0.01390	0.0684	0.8603	8515
6.6000	0.00325	0.0650	0.8616	3251	25979	0.01330	0.0655	0.8614	12695
6.6250	0.00312	0.0624	0.8626	3815	24442	0.01270	0.0628	0.8624	12695
6.6500	0.00299	0.0599	0.8636	3810	22731	0.01210	0.0602	0.8634	12695
6.6580	0.00295	0.0590	0.8640	3789	32725	—	—	—	—
6.6660	0.00292	0.0583	0.8643	3445	32020	—	—	—	—
6.6750	0.00288	0.0575	0.8646	4840	31067	0.01160	0.0577	0.8645	13695
6.6880	0.00282	0.0563	0.8652	3895	33240	—	—	—	—
6.7000	0.00276	0.0552	0.8656	5475	32324	0.01110	0.0552	0.8655	12695
6.7300	0.00262	0.0525	0.8667	3827	26634	0.01050	0.0526	0.8666	12655
6.7600	0.00250	0.0500	0.8678	4725	30433	0.01000	0.0500	0.8677	10695
6.8000	0.00235	0.0471	0.8692	5710	35690	0.00953	0.0467	0.8692	7905
6.8300	—	—	—	—	—	0.00920	0.0452	0.8702	6910

Table III: Parameters used in simulations with the asqtad action on $N_\tau = 8$ lattices and two lines of constant physics defined by $m_l/m_s = 0.05$ and 0.2 . The quark masses are given in units of the lattice spacing a . The zero and finite temperature runs were carried out on 32^4 and $32^3 \times 8$ lattices, respectively. The number of molecular dynamics time units for zero and finite temperature runs are given in columns labeled by TU_0 and TU_T , respectively.

β	m_l	m_s	u_0	TU_0	TU_T
6.800	0.00236	0.0471	0.8692	2040	29687
6.850	0.00218	0.0436	0.8709	3745	30452
6.875	0.00210	0.0420	0.8718	2025	18814
6.900	0.00202	0.0404	0.8726	3340	33427
6.925	0.00195	0.0389	0.8733	2925	27966
6.950	0.00187	0.0375	0.8741	2890	27734
6.975	0.00180	0.0361	0.8749	—	28464
6.985	0.00178	0.0355	0.8752	—	25191
7.000	0.00174	0.0347	0.8756	3055	25580
7.025	0.00167	0.0334	0.8764	—	21317
7.050	0.00161	0.0322	0.8771	3031	25605
7.085	0.00153	0.0305	0.8781	—	19070
7.125	0.00144	0.0289	0.8793	3100	32640
7.200	0.00128	0.0256	0.8813	4615	31175
7.300	0.00110	0.0220	0.8839	2645	34240
7.400	0.000946	0.0189	0.8863	1611	22805
7.550	0.000754	0.0151	0.8863	1611	26415

Table IV: Parameters used in simulations with the asqtad action on $N_\tau = 12$ lattices and the LCP defined by $m_l/m_s = 0.05$. The quark masses are given in units of the lattice spacing a . The zero and finite temperature runs were carried out on 48^4 and $48^3 \times 12$ lattices respectively.

Appendix B: Setting the lattice spacing in asqtad and HISQ/tree simulations

Three observables, r_0 , r_1 and f_K , were studied to set the lattice scale as discussed in Sec. II. In simulations with the asqtad action, we used the values of r_1 published in Ref. [41] and performed an interpolation using a renormalization group inspired Ansatz [41]

$$\frac{a}{r_1} = \frac{c_0 f(\beta) + c_2 (10/\beta) f^3(\beta) + c_4 (10/\beta)^2 f^3(\beta)}{1 + d_2 (10/\beta) f^2(\beta) + d_4 (10/\beta)^2 f^4(\beta)}, \quad (\text{B1})$$

β	m_l	m_s	TU_0	TU_T
6.000	0.0230	0.115	3,000	6,000
6.038	0.0216	0.108	3,000	6,000
6.100	0.0200	0.100	3,000	6,000
6.167	0.0182	0.091	3,000	6,000
6.200	0.0174	0.087	3,000	6,000
6.227	0.0168	0.084	3,000	6,000
6.256	0.0162	0.081	3,000	6,000
6.285	0.0158	0.079	3,000	6,000
6.313	0.0152	0.076	3,000	6,000
6.341	0.0148	0.074	3,000	6,000
6.369	0.0144	0.072	3,000	6,000
6.396	0.0140	0.070	3,000	6,000
6.450	0.0136	0.068	3,000	6,000
6.800	0.0100	0.050	3,000	—

Table V: Parameters used in simulations with the HISQ/tree action on $N_\tau = 6$ lattices and the LCP defined by $m_l/m_s = 0.2$. The quark masses are given in units of the lattice spacing a . The zero and finite temperature runs were carried out on $16^3 \times 32$ and $16^3 \times 6$ lattices respectively.

$$f(\beta) = (b_0(10/\beta))^{-b_1/(2b_0^2)} \exp(-\beta/(20b_0)), \quad (\text{B2})$$

$$c_0 = c_{00} + (c_{01u}m_l + c_{01s}m_s + c_{02}(2m_l + m_s))/f(\beta) \quad (\text{B3})$$

$$c_2 = c_{20} + c_{21}(2m_l + m_s)/f(\beta). \quad (\text{B4})$$

Here b_0 and b_1 are the coefficients of the universal 2-loop beta functions and for the numerical values of the other coefficients we get

$$\begin{aligned} c_{00} &= 4.574615 \cdot 10^1, c_{01u} = 6.081198 \cdot 10^{-1}, c_{01s} = 2.689340 \cdot 10^{-1}, \\ c_{02} &= -3.591183 \cdot 10^{-3}, c_{20} = -5.368781 \cdot 10^5, c_{21} = 8.756186 \cdot 10^2, \\ c_4 &= 2.930565 \cdot 10^5, d_2 = -3.786570 \cdot 10^3, d_4 = 7.385881 \cdot 10^6. \end{aligned} \quad (\text{B5})$$

To set the lattice scale using f_K , one needs to measure af_K on lattices with large volumes and on high statistics ensembles. The zero temperature asqtad ensembles generated in this study (see Tables III and IV) were primarily for performing subtractions of UV divergences. We, therefore, used the MILC collaboration study of the light meson decay constants and masses [81]. A systematic fit of f_K data, obtained on a large set of ensembles with similar parameters values as in this study, using staggered chiral perturbation theory gives values for $f_K r_1$ at nine β values in the range [6.458, 7.47]. We interpolated these results to obtain $f_K r_1$ at the physical quark mass at the β values used in the $0.05m_s$ LCP study and given in Tables III and IV. With $f_K r_1$ and our parametrization of r_1/a in hand we calculated the temperature associated with each β . The uncertainty in these T values is less than 1% over the range of β values investigated.

In simulations with the HISQ/tree action, we used r_0 , r_1 and f_K to set the lattice spacing. We determined r_0/a and r_1/a values from the static quark anti-quark potential. These values are summarized in Tables XV and XVI for the $m_l = 0.2m_s$ and the $m_l = 0.05m_s$ LCP, respectively. The last column contains the values of the additive renormalization constant $c(\beta)$ defined in Eq. (40) and used in the calculation of the renormalized Polyakov loop.

For the $m_l = 0.2m_s$ LCP, we fit r_0/a values with a form similar to Eq. (B1):

$$\frac{a}{r_0}(\beta)_{m_l=0.2m_s} = \frac{c_0 f(\beta) + c_2(10/\beta) f^3(\beta)}{1 + d_2(10/\beta) f^2(\beta)}, \quad (\text{B6})$$

where $c_0 = 32.83$, $c_2 = 81127$, $d_2 = 1778$ and $\chi^2/\text{dof} = 1.01$. Then we use $r_0 = 0.468$ fm obtained in Sec. II to calculate the lattice spacing in units of fm.

For the $0.05m_s$ ensembles, we preferred to use the r_1 scale, since the value of r_1 in fm is accurately determined by the MILC collaboration [58] and serves as an external input for this work. As one can see from Table XVI, our data set includes coarse lattices where $r_1/a < 2$. Extracting the value of r_1/a at such short distances is problematic due to

β	m_l	m_s	$T = 0$		$N_\tau = 6$	$N_\tau = 8$	$N_\tau = 12$
			$N_s^3 \times N_\tau$	TU_0	TU_T	TU_T	TU_T
5.900	0.00660	0.1320	$24^3 \times 32$	3700	22280	—	—
6.000	0.00569	0.1138	$24^3 \times 32$	5185	12030	—	—
6.025	0.00550	0.1100	$24^3 \times 32$	1345	16420	—	—
6.050	0.00532	0.1064	$24^3 \times 32$	4850	19990	—	—
6.075	0.00518	0.1036	—	—	20470	—	—
6.100	0.00499	0.0998	$28^3 \times 32$	4190	29380	—	—
6.125	0.00483	0.0966	—	—	20320	—	—
6.150	0.00468	0.0936	—	—	11220	—	—
6.175	0.00453	0.0906	—	—	10860	—	—
6.195	0.00440	0.0880	32^4	3175	22330	16520	—
6.215	0.00431	0.0862	—	—	6390	—	—
6.245	0.00415	0.0830	—	—	6400	8560	—
6.260	0.00405	0.0810	—	—	—	10340	—
6.285	0.00395	0.0790	32^4	3560	6750	16900	—
6.315	0.00380	0.0760	—	—	—	7950	—
6.341	0.00370	0.0740	32^4	3160	6590	11990	—
6.354	0.00364	0.0728	32^4	2295	5990	11990	—
6.390	0.00347	0.0694	32^4	4435	—	16120	—
6.423	0.00335	0.0670	32^4	2295	5990	11990	—
6.445	0.00326	0.0652	—	—	—	9000	—
6.460	0.00320	0.0640	$32^3 \times 64$	2610	—	10990	—
6.488	0.00310	0.0620	32^4	2295	8790	11990	—
6.515	0.00302	0.0604	32^4	2520	10430	10100	—
6.550	0.00291	0.0582	32^4	2295	7270	11900	—
6.575	0.00282	0.0564	32^4	2650	7330	14500	—
6.608	0.00271	0.0542	32^4	2295	6560	11990	—
6.664	0.00257	0.0514	32^4	2295	8230	11990	4240
6.700	0.00248	0.0496	—	—	—	—	7000
6.740	0.00238	0.0476	48^4	1350	—	—	6670
6.770	0.00230	0.0460	—	—	—	—	6820
6.800	0.00224	0.0448	32^4	5650	7000	11990	7090
6.840	0.00215	0.0430	—	—	—	—	8410
6.860	0.00210	0.0420	—	—	—	—	2740
6.880	0.00206	0.0412	48^4	1400	—	—	10120
6.910	0.00200	0.0400	—	—	—	—	4630
6.950	0.00193	0.0386	32^4	10830	7480	11990	6700
6.990	0.00185	0.0370	—	—	—	—	5470
7.030	0.00178	0.0356	48^4	1355	—	—	7290
7.100	0.00166	0.0332	—	—	—	—	10300
7.150	0.00160	0.0320	32^4	2295	4770	11990	10390
7.150	0.00160	0.0320	$48^3 \times 64$	1458	—	—	—
7.280	0.00142	0.0284	$48^3 \times 64$	1734	—	—	11620

Table VI: Parameters used in simulations with the HISQ/tree action on $N_\tau = 6, 8$ and 12 lattices and the LCP defined by $m_l/m_s = 0.05$. The quark masses are given in units of the lattice spacing a . The statistics in molecular dynamics time units TU are given for both the zero and finite temperature runs. The lattice sizes used for the $N_\tau = 6, 8$ and 12 finite temperature simulations were $24^3 \times 6$, $32^3 \times 8$ and $48^3 \times 12$, respectively.

β	m_l	m_s	TU_T
$N_\tau = 6$			
6.000	0.0028450	0.1138	3510
6.025	0.0027500	0.1100	3460
6.050	0.0026600	0.1064	3710
6.075	0.0025900	0.1036	3930
6.100	0.0024950	0.0998	3200
6.125	0.0024150	0.0966	4020
$N_\tau = 8$			
6.215	0.0021425	0.0857	860
6.230	0.0021025	0.0841	950
6.245	0.0020750	0.0830	3730
6.260	0.0020250	0.0810	4090
6.285	0.0019750	0.0790	4050
6.300	0.0019300	0.0772	4040
6.315	0.0019000	0.0760	4170
6.330	0.0018650	0.0746	4040
6.341	0.0018500	0.0740	1340
6.354	0.0018200	0.0728	4070
6.365	0.0017900	0.0716	4420
6.390	0.0017350	0.0694	4490
6.423	0.0016750	0.0670	1710

Table VII: Parameters used in simulations with the HISQ/tree action on $N_\tau = 6$ and 8 lattices and the LCP defined by $m_l/m_s = 0.025$. The quark masses are given in units of the lattice spacing a . The finite temperature runs were carried out on $32^3 \times 6$ and $32^3 \times 8$ lattices as part of the RBC-Bielefeld study of $O(N)$ scaling [76].

significant systematic errors. Therefore, we used the following strategy: for coarser lattices we converted r_0/a values into r_1/a using the continuum ratio $(r_0/r_1)_{cont}$ derived in Sec. II and defined as

$$\frac{r_1}{a} \Big|_{m_l=0.05m_s} \equiv \begin{cases} r_0/a/(r_0/r_1)_{cont}, & \beta < \beta_{01}, \\ r_1/a, & \beta \geq \beta_{01}, \end{cases}, \quad (B7)$$

where the optimal value of β_{01} is determined as follows. We fit a/r_1 to the Ansatz:

$$\frac{a}{r_1}(\beta)_{m_l=0.05m_s} = \frac{c_0 f(\beta) + c_2 (10/\beta) f^3(\beta)}{1 + d_2 (10/\beta) f^2(\beta)} \quad (B8)$$

and varied β_{01} in the range $[6.423, 6.608]$ examining the χ^2 of the fit. The minimum of χ^2 is achieved at $\beta_{01} = 6.423$. With this choice of β_{01} the coefficients of the fit are $c_0 = 44.06$, $c_2 = 272102$, $d_2 = 4281$ and $\chi^2/\text{dof} = 0.31$. The data and the fit are shown in Fig. 26.

We also use f_K as an independent observable for scale setting. We fit af_K data to a form similar to (B8):

$$af_K(\beta)_{m_l=0.05m_s} = \frac{c_0^K f(\beta) + c_2^K (10/\beta) f^3(\beta)}{1 + d_2^K (10/\beta) f^2(\beta)}. \quad (B9)$$

In the continuum limit, the product $r_1 f_K$ is fixed:

$$r_1 f_K = \frac{0.3106 \text{ fm} \cdot 156.1/\sqrt{2} \text{ MeV}}{197.3 \text{ fm} \cdot \text{MeV}} \simeq 0.1738. \quad (B10)$$

Taking the ratio of Eqs. (B9) and (B8) one finds

$$r_1 f_K = \frac{c_0^K}{c_0} \Rightarrow c_0^K = 7.66. \quad (B11)$$

β	T MeV	m_s	$2 \times \langle \bar{\psi}\psi \rangle_l$	$2 \times \langle \bar{\psi}\psi \rangle_s$	χ_l^{dis}	χ_l^{con}	χ_s	$3 \times L_{\text{bare}}$
$m_l/m_s = 0.05$								
6.550	165.1	0.0705	0.04306(06)	0.15461(3)	0.915(39)	1.2570(15)	0.1037(45)	0.00578(06)
6.575	170.5	0.0677	0.03698(11)	0.14547(5)	1.035(50)	1.3068(26)	0.1350(70)	0.00730(08)
6.600	176.0	0.0650	0.03111(13)	0.13672(5)	1.179(56)	1.3682(51)	0.1664(51)	0.00910(09)
6.625	181.5	0.0624	0.02531(20)	0.12832(7)	1.536(73)	1.4496(80)	0.2112(64)	0.01146(14)
6.650	187.0	0.0599	0.01979(16)	0.12027(5)	1.490(65)	1.5282(51)	0.2675(45)	0.01428(15)
6.658	188.8	0.0590	0.01837(13)	0.11765(6)	1.381(50)	1.5381(33)	0.2861(51)	0.01515(09)
6.666	190.6	0.0583	0.01681(08)	0.11528(4)	1.183(88)	1.5506(20)	0.3130(38)	0.01627(09)
6.675	192.6	0.0575	0.01490(12)	0.11264(4)	1.024(57)	1.5609(26)	0.3341(51)	0.01735(09)
6.688	195.6	0.0563	0.01313(14)	0.10890(5)	0.912(45)	1.5274(30)	0.3725(38)	0.01893(11)
6.700	198.3	0.0552	0.01123(08)	0.10539(3)	0.687(34)	1.4977(29)	0.4006(38)	0.02078(09)
6.730	205.2	0.0525	0.00843(08)	0.09741(4)	0.344(34)	1.3621(66)	0.4781(38)	0.02465(12)
6.760	212.2	0.0500	0.00671(05)	0.09023(4)	0.163(12)	1.2247(45)	0.5478(32)	0.02830(14)
6.800	221.7	0.0471	0.00526(03)	0.08185(4)	0.069(05)	1.0719(49)	0.6227(38)	0.03365(13)
$m_l/m_s = 0.1$								
6.4580	144.0	0.0820	0.07942(07)		0.531(20)	1.0261(05)		
6.5000	152.4	0.0765	0.06684(06)		0.564(40)	1.0416(06)		
6.5500	162.8	0.0705	0.05359(07)		0.554(25)	1.0623(08)		
6.6000	173.5	0.0650	0.04183(10)		0.668(31)	1.0944(19)		
6.6250	179.0	0.0624	0.03657(09)		0.724(64)	1.1150(19)		
6.6500	184.5	0.0599	0.03116(15)		0.925(78)	1.1433(28)		
6.6580	186.4	0.0590	0.02900(11)		0.891(48)	1.1614(23)		
6.6660	188.2	0.0583	0.02770(14)		0.916(64)	1.1661(31)		
6.6750	190.2	0.0575	0.02579(13)		0.946(88)	1.1763(28)		
6.6830	192.1	0.0567	0.02394(17)		0.996(69)	1.1873(23)		
6.6910	193.8	0.0560	0.02278(15)		0.803(56)	1.1877(22)		
6.7000	196.0	0.0552	0.02108(12)		0.799(51)	1.1881(22)		
6.7080	197.8	0.0544	0.01976(16)		0.759(89)	1.1880(19)		
6.7150	199.4	0.0538	0.01872(13)		0.664(50)	1.1833(16)		
6.7300	202.9	0.0525	0.01648(10)		0.501(33)	1.1675(17)		
6.7450	206.5	0.0512	0.01474(10)		0.414(33)	1.1425(20)		
6.7600	210.0	0.0500	0.01343(07)		0.349(20)	1.1131(13)		
6.8000	219.6	0.0471	0.01054(05)		0.170(11)	1.0200(20)		
6.8500	232.0	0.0437	0.00840(03)		0.058(03)	0.9231(20)		

Table VIII: Data for the light and strange quark chiral condensate, disconnected and connected chiral susceptibility, the strange quark number susceptibility and the bare Polyakov loop for the asqtad action on $N_\tau = 8$ lattices and the two lines of constant physics defined by $m_l/m_s = 0.05$ and $m_l/m_s = 0.1$. The data for the light and strange quark condensate are presented using the 2-flavor normalization.

We, therefore, varied only c_2^K and d_2^K in the Ansatz (B9) and got $c_2^K = 32911$, $d_2^K = 2388$, $\chi^2/\text{dof} = 3.5$. Presumably, the errors on af_K are somewhat underestimated and this results in a high χ^2/dof . However, the fluctuations of the data around the fit are, at worst, 1%; therefore we feel comfortable using the Ansatz in Eq. (B9) for setting the temperature scale. This fit is shown in Fig. 27.

For those ensembles where a/r_1 and af_K measurements are available, we can compare the difference between the lattice spacing defined from r_1 and f_K . We define

$$a_{r_1} \equiv \frac{1}{r_1/a|_{m_l=0.05m_s}} \times 0.3106 \text{ fm}, \quad (\text{B12})$$

$$a_{f_K} \equiv (af_K) \cdot \frac{197.3 \text{ MeV}\cdot\text{fm}}{156.1/\sqrt{2} \text{ MeV}}, \quad (\text{B13})$$

β	T MeV	m_s	$2 \times \langle \bar{\psi}\psi \rangle_l$	$2 \times \langle \bar{\psi}\psi \rangle_s$	χ_l^{dis}	χ_l^{con}	χ_s	$3 \times L_{\text{bare}}$
6.800	147.8	0.0471	0.017823(21)	0.088585(10)	0.4343(155)	1.0215(07)	0.0720(72)	0.000683(21)
6.850	155.9	0.0436	0.014203(27)	0.079482(11)	0.4999(142)	1.0336(11)	0.1152(72)	0.000985(18)
6.875	160.0	0.0420	0.012458(46)	0.075317(17)	0.6227(384)	1.0471(23)	0.1598(86)	0.001218(25)
6.900	164.2	0.0404	0.010962(33)	0.071361(14)	0.6410(265)	1.0602(15)	0.1728(72)	0.001450(20)
6.925	168.5	0.0389	0.009495(45)	0.067657(14)	0.6843(356)	1.0783(28)	0.1973(72)	0.001752(23)
6.950	172.8	0.0375	0.008019(64)	0.064170(26)	0.7850(596)	1.1005(29)	0.2491(86)	0.002124(38)
6.975	177.3	0.0361	0.006741(45)	0.060787(20)	0.7348(458)	1.1088(17)	0.3024(72)	0.002494(29)
6.985	179.1	0.0355	0.006148(47)	0.059361(21)	0.6692(617)	1.1085(16)	0.3326(86)	0.002757(30)
7.000	181.8	0.0347	0.005544(53)	0.057468(22)	0.6432(421)	1.0973(13)	0.3614(72)	0.003048(31)
7.025	186.3	0.0334	0.004544(36)	0.054397(17)	0.3990(286)	1.0665(14)	0.4147(86)	0.003591(34)
7.050	191.0	0.0322	0.003943(28)	0.051647(17)	0.2760(131)	1.0264(25)	0.4450(86)	0.004037(30)
7.085	197.6	0.0305	0.003209(22)	0.047827(21)	0.1585(137)	0.9502(28)	0.5386(86)	0.004993(39)
7.125	205.4	0.0289	0.002672(11)	0.044212(13)	0.0756(047)	0.8793(19)	0.5861(58)	0.005955(37)
7.200	220.7	0.0256	0.002068(08)	0.037549(10)	0.0266(022)	0.7898(22)	0.6984(58)	0.008019(38)
7.300	242.5	0.0220	0.001588(03)	0.030717(07)	0.0057(009)	0.7180(12)	0.7862(58)	0.010999(39)
7.400	265.9	0.0189	0.001286(02)	0.025334(06)	0.0017(003)	0.6785(07)	0.8510(58)	0.014392(84)
7.550	304.7	0.0151	0.000970(03)	0.019278(04)	0.0012(011)	0.6419(12)		

Table IX: Data for the light and strange quark chiral condensate, disconnected and connected chiral susceptibility, the strange quark number susceptibility and the bare Polyakov loop for the asqtad action on $N_\tau = 12$ lattices and the LCP defined by $m_l/m_s = 0.05$. The data for the light and strange quark condensate are presented using the 2-flavor normalization.

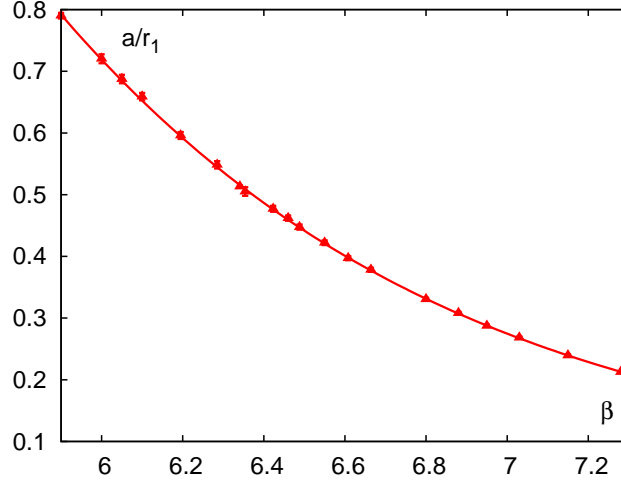


Figure 26: The a/r_1 data, defined in Eq. (B7), together with the smoothing fit for the HISQ/tree action, $m_l = 0.05m_s$ LCP.

and

$$\Delta_a \equiv \frac{|a_{f_K} - a_{r_1}|}{a_{r_1}} \cdot 100\%. \quad (\text{B14})$$

The difference Δ_a is shown in Fig. 28. It is about 8% in the lattice spacings corresponding to the coarsest ensemble and decreases to about 1% for the finest $N_\tau = 12$ ensembles on which f_K was measured. The temperature corresponding to these fine lattices is about 240 MeV.

Appendix C: Hadron spectrum with the HISQ/tree action

This appendix contains results of the calculations of the hadron correlation functions and some details on the extraction of the masses and decay constants. Fits to the correlation functions for mesons and baryons are performed

β	T MeV	am_s	$2 \times \langle \bar{\psi}\psi \rangle_l$	$2 \times \langle \bar{\psi}\psi \rangle_s$	χ_l^{dis}	χ_l^{con}	χ_t	χ_s	$3 \times L_{\text{bare}}$
$m_l/m_s = 0.025$									
6.0000	147.262	0.1138	0.05766(15)	0.17718(8)	1.32(16)				
6.0250	150.876	0.1100	0.05086(23)	0.16948(11)	1.33(23)				
6.0500	154.584	0.1064	0.04525(20)	0.16223(6)	1.61(25)				
6.0750	158.389	0.1036	0.03842(22)	0.15533(8)	1.72(21)				
6.1000	162.292	0.0998	0.03161(29)	0.14777(12)	2.23(18)				
6.1250	166.295	0.0966	0.02511(28)	0.14063(10)	1.48(12)				
6.1500	170.400	0.0936	0.01799(44)	0.13339(14)	1.68(09)				
6.1750	174.610	0.0906	0.01372(41)	0.12671(24)	1.18(11)				
$m_l/m_s = 0.05$									
5.900	133.710	0.1320	0.089873(076)	0.210216(046)	0.5767(237)	0.7967(025)			0.00786(65)
6.000	147.262	0.1138	0.065834(071)	0.177805(037)	0.7307(182)	0.9124(046)	0.239(20)	0.1076(25)	0.01235(14)
6.025	150.876	0.1100	0.059957(105)	0.170305(035)	0.8508(277)	0.9564(048)	0.286(04)	0.1236(17)	0.01367(21)
6.050	154.584	0.1064	0.054023(089)	0.162915(051)	0.9711(409)	0.9448(060)	0.301(17)	0.1429(32)	0.01573(14)
6.075	158.389	0.1036	0.048293(128)	0.156244(044)	1.0169(307)	1.0551(037)	0.365(05)	0.1667(18)	0.01805(16)
6.100	162.292	0.0998	0.041948(105)	0.148575(040)	1.1426(278)	1.1358(273)	0.475(21)	0.2020(65)	0.02098(16)
6.125	166.295	0.0966	0.036062(123)	0.141563(049)	1.2281(366)	1.2068(061)	0.467(05)	0.2319(19)	0.02441(15)
6.150	170.400	0.0936	0.029645(259)	0.134460(098)	1.3652(617)	1.2792(091)	0.531(17)	0.2740(40)	0.02875(36)
6.175	174.610	0.0906	0.024075(159)	0.127619(079)	1.1297(692)	1.3365(081)	0.600(12)	0.3200(54)	
6.195	178.054	0.0880	0.020080(104)	0.122064(051)	1.0001(172)	1.3415(068)	0.640(35)	0.3560(72)	0.03664(29)
6.215	181.568	0.0862	0.016410(172)	0.117038(095)	0.7007(439)	1.3053(074)	0.675(11)	0.3974(58)	0.04057(31)
6.245	186.969	0.0830	0.012735(179)	0.109962(123)	0.4768(400)	1.2076(075)	0.711(07)	0.4424(40)	0.04646(49)
6.285	194.423	0.0790	0.009099(091)	0.100599(080)	0.1752(094)	1.0271(050)	0.757(14)	0.5116(65)	0.05534(40)
6.341	205.355	0.0740	0.006545(101)	0.089489(156)	0.0812(104)	0.8432(088)	0.799(10)	0.5879(72)	0.06806(54)
6.354	207.977	0.0728	0.006011(038)	0.086944(096)	0.0476(049)	0.7958(056)	0.798(10)	0.6098(72)	0.07110(54)
6.423	222.450	0.0670	0.004457(023)	0.075293(079)	0.0174(036)	0.6583(028)	0.838(08)	0.6883(54)	0.08810(38)
6.488	236.960	0.0620	0.003643(019)	0.066299(040)	0.0065(022)	0.5854(017)	0.846(06)	0.7420(43)	0.10367(41)
6.515	243.246	0.0603	0.003387(013)	0.063337(051)	0.0019(012)	0.5632(016)	0.849(05)	0.7560(43)	0.11238(52)
6.550	251.627	0.0581	0.003149(019)	0.059679(031)	0.0003(008)	0.5410(012)	0.849(08)	0.7787(54)	0.12180(61)
6.575	257.777	0.0564	0.002977(011)	0.057089(046)	0.0019(010)				0.12714(58)
6.608	266.106	0.0542	0.002798(011)	0.053897(029)	0.0021(015)				0.13663(63)
6.664	280.807	0.0514	0.002549(017)	0.049855(046)	0.0019(011)	0.4966(009)			0.15203(70)
6.800	319.609	0.0448	0.002101(012)	0.041501(018)	0.0005(007)	0.4669(003)	0.861(04)	0.8248(36)	0.18747(68)
6.950	367.875	0.0386	0.001746(007)	0.034571(012)	0.0004(009)	0.4495(003)	0.864(06)	0.8374(58)	0.22876(74)
7.150	442.160	0.0320	0.001412(010)	0.027810(016)	-0.0025(014)	0.4353(001)	0.849(05)	0.8395(43)	0.28241(73)

Table X: Data for the light and strange quark chiral condensate, disconnected and connected chiral susceptibility, the light and strange quark number susceptibility and the bare Polyakov loop for the HISQ/tree action on $N_\tau = 6$ lattices and the two lines of constant physics defined by $m_l/m_s = 0.025$ and $m_l/m_s = 0.05$. A thousand trajectories were discarded for thermalization.

choosing either the maximum allowed separation, typically $N_t/2 = 16$, or up to a distance where the fractional error exceeds 30%. The minimum distance is varied to estimate the systematic effects due to contamination from excited states. In most cases, the fit function includes the ground state and the opposite parity state that contributes with an alternating sign, and their contribution due to back-propagation. In some cases, the first excited state is also included. To reduce the uncertainty due to auto-correlations in the estimation of statistical errors, we block the data by 10.

The calculation of hadron correlators was done using wall sources. The pseudoscalar meson masses were calculated on most of our zero temperature lattices in order to establish the LCP. The data for the $m_l = 0.2m_s$ LCP are given in Table XVII, and for $0.05m_s$ in Table XVIII. We also calculated the pseudoscalar meson decay constants for different combinations of the quark masses. For these calculations, we used both wall and point sources and performed a simultaneous fit to the two correlators. In most cases, we used one wall source per lattice, but in some cases we used two or four sources. In Table XIX, we give the pseudoscalar meson decay constants in lattice units and specify the

β	T MeV	am_s	$2 \times \langle \bar{\psi}\psi \rangle_l$	$2 \times \langle \bar{\psi}\psi \rangle_s$	χ_l^{dis}	χ_l^{con}	χ_l	χ_s	$3 \times L_{\text{bare}}$
$m_l/m_s = 0.025$									
6.2450	140.227	0.0830	0.03034(07)	0.11810(4)	0.90(07)				
6.2600	142.298	0.0811	0.02812(14)	0.11447(7)	1.09(10)				
6.2850	145.817	0.0790	0.02514(15)	0.10994(8)	0.96(09)				
6.3000	147.970	0.0773	0.02279(19)	0.10643(11)	1.16(11)				
6.3150	150.154	0.0759	0.02105(15)	0.10381(7)	1.30(07)				
6.3300	152.370	0.0746	0.01953(17)	0.10111(8)	1.32(11)				
6.3540	155.983	0.0728	0.01610(20)	0.09688(8)	1.47(07)				
6.3650	157.666	0.0717	0.01427(17)	0.09449(6)	1.44(07)				
6.3900	161.558	0.0695	0.01142(26)	0.09010(9)	1.32(09)				
6.4230	166.837	0.0670	0.00842(20)	0.08503(9)	0.77(10)				
6.4450	170.448	0.0653	0.00646(25)	0.08143(15)	0.72(10)				
$m_l/m_s = 0.05$									
6.1950	133.541	0.0880	0.042262(031)	0.12903(2)	0.3855(121)	0.7987(25)	0.1670(314)	0.0659(51)	0.00289(06)
6.2450	140.227	0.0830	0.035540(065)	0.11837(4)	0.5719(183)	0.8203(52)	0.2016(623)	0.0935(61)	0.00381(07)
6.2600	142.298	0.0811	0.033581(085)	0.11487(4)	0.5822(301)	0.8395(42)	0.2559(183)	0.1095(28)	0.00406(10)
6.2850	145.817	0.0790	0.030407(073)	0.11018(3)	0.6314(262)	0.8638(44)	0.2729(078)	0.1212(19)	0.00489(09)
6.3150	150.154	0.0759	0.026587(105)	0.10415(4)	0.7213(276)	0.8978(56)	0.3481(175)	0.1461(50)	0.00577(06)
6.3410	154.016	0.0740	0.023661(103)	0.09968(4)	0.7739(205)	0.9205(58)	0.3418(370)	0.1651(90)	0.00664(08)
6.3540	155.983	0.0728	0.021917(088)	0.09721(5)	0.7761(500)	0.9320(53)	0.4147(230)	0.1849(64)	0.00734(06)
6.3900	161.558	0.0695	0.017638(160)	0.09054(5)	0.9397(436)	0.9839(55)	0.4721(104)	0.2381(41)	0.00937(18)
6.4230	166.837	0.0670	0.013908(119)	0.08525(5)	0.8828(466)	1.0351(67)	0.5547(051)	0.2895(24)	0.01151(10)
6.4450	170.448	0.0653	0.011433(130)	0.08153(7)	0.7199(464)	1.0390(49)	0.6121(157)	0.3362(29)	0.01325(17)
6.4600	172.952	0.0642	0.010222(097)	0.07919(5)	0.6721(343)	1.0315(65)	0.6473(043)	0.3623(30)	0.01468(11)
6.4880	177.720	0.0620	0.008284(082)	0.07519(5)	0.4976(242)	0.9822(39)	0.6914(074)	0.4134(59)	0.01631(36)
6.5150	182.435	0.0603	0.006738(062)	0.07165(5)	0.3083(153)	0.9126(44)	0.7296(100)	0.4589(58)	0.01937(16)
6.5500	188.720	0.0582	0.005356(051)	0.06722(5)	0.1661(165)	0.8202(54)	0.7632(037)	0.5177(31)	0.02264(38)
6.5750	193.333	0.0564	0.004616(022)	0.06400(3)	0.0994(078)	0.7540(65)	0.7878(114)	0.5632(64)	0.02539(20)
6.6080	199.580	0.0542	0.003944(024)	0.06007(4)	0.0636(043)	0.6891(47)	0.8030(036)	0.6052(32)	0.02907(30)
6.6640	210.605	0.0514	0.003242(020)	0.05494(5)	0.0317(027)	0.6125(26)	0.8318(031)	0.6711(29)	0.03566(28)
6.8000	239.706	0.0448	0.002343(009)	0.04462(2)	0.0068(011)	0.5192(13)	0.8741(021)	0.7796(21)	0.05368(24)
6.9500	275.906	0.0386	0.001855(005)	0.03651(1)	-0.0013(007)	0.4786(06)	0.8984(016)	0.8443(17)	0.07535(24)
7.1500	331.620	0.0320	0.001454(003)	0.02901(1)	0.0001(009)	0.4554(04)	0.9123(014)	0.8829(14)	0.10485(30)

Table XI: Data for the light and strange quark chiral condensate, disconnected and connected chiral susceptibility, the light and strange quark number susceptibility and the bare Polyakov loop for the HISQ/tree action on $N_\tau = 8$ lattices and the two lines of constant physics defined by $m_l/m_s = 0.025$ and $m_l/m_s = 0.05$. Fifteen hundred trajectories were discarded for thermalization.

number of sources per lattice used in the calculations.

We also calculated the vector meson and the baryon (nucleon and Ω) masses on some of the $T = 0$ ensembles. The results are given in Table XX for the $m_l = 0.2m_s$ LCP and in Table XXI for the $m_l = 0.05m_s$ LCP and discussed in Sec. II. To improve the statistics we used 4 sources per lattice for the calculation of vector mesons and nucleon correlation functions. It was sufficient to use one source for the baryon as it is composed of three heavier strange quarks.

Appendix D: Autocorrelations in HISQ/tree simulations

An analysis of autocorrelations in zero-temperature calculations with the HISQ action at the light quark mass $m_l = 0.2m_s$ has been presented in Ref. [46]. Note that the HISQ/tree action used in this paper differs from the HISQ action in Ref. [46] in that it does not include a dynamical charm quark and uses only the tree-level instead of the one-loop improved coefficient for the Symanzik gauge action. We calculate the dimensionless autocorrelation

β	T MeV	am_s	$2 \times \langle \bar{\psi}\psi \rangle_l$	$2 \times \langle \bar{\psi}\psi \rangle_s$	χ_l^{dis}	χ_l^{con}	χ_l	χ_s	$3 \times L_{\text{bare}}$
6.6640	140.403	0.0514	0.011032(61)	0.060172(32)	0.414(57)	0.6697(075)	0.251(57)	0.1440(072)	0.001011(095)
6.7000	145.321	0.0496	0.009642(38)	0.057132(18)	0.437(34)	0.6652(155)	0.310(52)	0.1570(086)	0.001173(110)
6.7400	150.967	0.0476	0.008127(41)	0.053835(28)	0.449(23)	0.6735(060)	0.403(41)	0.1987(115)	0.001434(060)
6.7700	155.329	0.0461	0.006998(78)	0.051354(19)	0.504(42)	0.6748(110)	0.504(37)	0.2362(072)	0.001814(075)
6.8000	159.804	0.0448	0.006157(63)	0.049359(18)	0.543(51)	0.6731(095)	0.520(23)	0.2606(072)	0.002152(030)
6.8400	165.949	0.0430	0.004685(76)	0.046456(35)	0.491(27)	0.6921(068)	0.657(24)	0.3571(072)	0.002821(101)
6.8800	172.302	0.0412	0.003745(59)	0.043759(28)	0.391(39)	0.6592(065)	0.649(19)	0.3816(101)	0.003449(067)
6.9100	177.207	0.0401	0.003099(47)	0.041876(36)	0.253(30)	0.6421(121)	0.757(14)	0.4752(072)	0.004293(106)
6.9500	183.938	0.0386	0.002680(32)	0.039783(26)	0.164(13)	0.6150(067)	0.743(21)	0.5069(086)	0.005024(075)
6.9900	190.893	0.0370	0.002307(36)	0.037522(28)	0.104(16)	0.5743(034)	0.814(17)	0.5832(086)	0.006139(092)
7.0300	198.078	0.0356	0.002036(14)	0.035543(24)	0.062(07)	0.5318(046)	0.842(12)	0.6322(101)	0.007371(036)
7.1000	211.225	0.0333	0.001738(10)	0.032396(16)	0.030(04)	0.5052(046)	0.855(09)	0.6998(101)	0.009511(077)
7.1500	221.080	0.0320	0.001611(08)	0.030768(08)	0.016(03)	0.4955(017)	0.868(05)	0.7387(043)	0.011144(095)
7.2800	248.626	0.0285	0.001361(07)	0.026477(08)	0.012(03)	0.4710(007)	0.891(04)	0.8064(043)	0.016284(077)

Table XII: Data for the light and strange quark chiral condensate, disconnected and connected chiral susceptibility, the light and strange quark number susceptibility and the bare Polyakov loop for the HISQ/tree action on $N_\tau = 12$ lattices and the LCP defined by $m_l/m_s = 0.05$. Two hundred trajectories were discarded for thermalization.

β	m_s	$2 \times \langle \bar{\psi}\psi \rangle_l$	$2 \times \langle \bar{\psi}\psi \rangle_s$
32 ⁴			
6.600	0.0650	0.04102(5)	0.13908(4)
6.625	0.0624	0.03716(6)	0.13127(5)
6.650	0.0599	0.03389(5)	0.12406(4)
6.658	0.0590	0.03266(7)	0.12147(5)
6.666	0.0583	0.03179(6)	0.11944(3)
6.675	0.0575	0.03086(4)	0.11717(3)
6.688	0.0563	0.02936(4)	0.11375(3)
6.700	0.0552	0.02811(5)	0.11071(3)
6.730	0.0525	0.02506(7)	0.10331(4)
6.760	0.0500	0.02260(5)	0.09672(3)
6.800	0.0471	0.01976(5)	0.08896(2)
48 ⁴			
6.800	0.0471	0.01970(3)	0.08886(2)
6.850	0.0436	0.01672(4)	0.07997(3)
6.875	0.0420	0.01539(3)	0.07594(2)
6.900	0.0404	0.01425(2)	0.07213(2)
6.925	0.0389	0.01319(3)	0.06855(2)
6.950	0.0375	0.01218(2)	0.06521(2)
7.000	0.0347	0.01041(2)	0.05888(1)
7.050	0.0322	0.00898(3)	0.05339(2)
7.085	0.0305	0.00815(3)	0.04982(2)
7.125	0.0289	0.00730(2)	0.04640(1)
7.200	0.0256	0.00583(2)	0.03989(1)
7.300	0.0220	0.00447(3)	0.03307(2)
7.400	0.0189	0.00341(3)	0.02748(1)
7.550	0.0151	0.00223(5)	0.02100(2)

Table XIII: Data for the light and strange quark chiral condensate for the asqtad action on $N_\tau = 8$ and 12 zero temperature ensembles with the line of constant physics defined by $m_l/m_s = 0.05$. The data for the light and strange quark condensate are presented using the 2-flavor normalization.

β	m_s	$2 \times \langle \bar{\psi}\psi \rangle_l$	$2 \times \langle \bar{\psi}\psi \rangle_s$
$24^3 \times 32$			
5.900	0.1320	0.09833(6)	0.21164(3)
6.000	0.1138	0.07801(22)	0.18024(10)
6.050	0.1064	0.06890(8)	0.16621(6)
$28^3 \times 32$			
6.100	0.0998	0.06070(7)	0.15300(6)
32^4			
6.195	0.0880	0.04700(14)	0.12983(8)
6.285	0.0790	0.03660(11)	0.11134(3)
6.341	0.0740	0.03128(8)	0.10134(4)
6.354	0.0728	0.03014(8)	0.09900(5)
6.390	0.0695	0.02723(7)	0.09295(4)
6.423	0.0670	0.02499(7)	0.08817(3)
6.488	0.0620	0.02069(9)	0.07906(6)
6.515	0.0603	0.01920(10)	0.07588(5)
6.550	0.0582	0.01744(9)	0.07203(4)
6.575	0.0564	0.01635(4)	0.06908(3)
6.608	0.0542	0.01485(6)	0.06548(5)
6.664	0.0514	0.01281(6)	0.06061(3)
6.800	0.0448	0.00883(6)	0.05008(4)
6.950	0.0386	0.00611(9)	0.04130(3)
7.150	0.0320	0.00366(8)	0.03259(5)
$32^3 \times 64$			
6.460	0.0642	0.02238(5)	0.08269(2)
48^4			
6.740	0.0476	0.01080(4)	0.05445(2)
6.880	0.0412	0.00765(3)	0.04500(1)
7.030	0.0356	0.00544(4)	0.03731(1)
$48^3 \times 64$			
7.150	0.0320	0.00420(5)	0.03255(2)
7.280	0.0285	0.00322(2)	0.02815(1)

Table XIV: Data for the light and strange quark chiral condensate for the HISQ/tree action on $N_\tau = 6, 8$ and 12 zero temperature ensembles with the line of constant physics defined by $m_l/m_s = 0.05$. The data for the light and strange quark condensate are presented using the 2-flavor normalization.

coefficient defined as

$$C_{\Delta t} = \frac{\langle x_i x_{i+\Delta t} \rangle - \langle x_i \rangle^2}{\langle x_i^2 \rangle - \langle x_i \rangle^2} \quad (\text{D1})$$

for several representative ensembles both at zero and finite temperature at $m_l = 0.05m_s$.

The autocorrelation coefficients for the plaquette, light and strange quark chiral condensate and the topological charge are shown in Tables XXII and XXIII. At zero temperature, the autocorrelation coefficient is given at time separation $\Delta t = 5$ for $\beta = 6.000, 6.285$ and 6.460 , and $\Delta t = 6$ for $\beta = 7.280$. At finite temperature, the autocorrelation coefficient is given at time separation $\Delta t = 10$. The chiral condensate was measured using one source on zero temperature lattices and with ten sources on finite temperature lattices. In several cases (mostly for zero temperature ensembles), the autocorrelation function for the light quark chiral condensate is too noisy to extract $C_{\Delta t}$ reliably.

The integrated autocorrelation time,

$$\tau_{int} = 1 + 2 \sum_{\Delta t=1}^{\infty} C(\Delta t), \quad (\text{D2})$$

provides an estimate of the time separation at which measurements can be considered statistically independent. To

β	r_0/a	r_1/a	r_0^{fit}/a	$c(\beta) \cdot r_0$
6.000	2.037(12)	1.410(13)	2.052	-1.622(17)
6.038	2.141(12)	1.473(12)	2.128	-1.678(28)
6.100	2.250(12)	1.544(19)	2.256	-1.834(44)
6.167	2.413(12)	1.659(19)	2.403	-1.965(66)
6.200	2.501(17)	1.722(20)	2.478	-2.008(26)
6.227	2.537(12)	1.745(12)	2.542	-2.094(52)
6.256	2.603(14)	1.798(20)	2.611	-2.124(53)
6.285	2.715(25)	1.813(60)	2.683	-2.167(32)
6.313	2.742(20)	1.848(12)	2.753	-2.274(39)
6.341	2.802(32)	1.910(10)	2.826	-2.299(54)
6.369	2.916(39)	1.983(14)	2.900	-2.331(66)
6.396	2.937(30)	2.016(20)	2.973	-2.420(61)
6.450	3.110(30)	2.132(14)	3.124	-2.546(84)
6.800	4.330(65)	2.962(26)	4.278	-3.458(73)

Table XV: Estimates of the scale setting parameters r_0 , r_1 and the additive renormalization constant $c(\beta)$ in the determination of the potential for the HISQ/tree calculations along the $m_l = 0.2m_s$ LCP. See text for the definition of r_0^{fit} .

β	r_0/a	r_1/a	r_1^{fit}/a	$c(\beta) \cdot r_0$
5.900	1.909(11)	1.23(13)	1.263	-1.441(15)
6.000	2.094(21)	1.386(80)	1.391	-1.639(28)
6.050	2.194(22)	1.440(31)	1.460	-1.748(28)
6.100	2.289(21)	1.522(30)	1.533	-1.828(27)
6.195	2.531(24)	1.670(30)	1.682	-2.072(31)
6.285	2.750(30)	1.822(30)	1.836	-2.257(36)
6.341	2.939(11)	1.935(30)	1.940	-2.440(14)
6.354	2.986(41)	1.959(30)	1.964	-2.498(49)
6.423	3.189(22)	2.096(21)	2.101	-2.653(27)
6.460	3.282(32)	2.165(20)	2.178	-2.706(36)
6.488	3.395(31)	2.235(21)	2.238	-2.808(37)
6.550	3.585(14)	2.369(21)	2.377	-2.946(17)
6.608	3.774(20)	2.518(21)	2.513	-3.070(27)
6.664	3.994(14)	2.644(23)	2.652	-3.251(16)
6.800	4.541(30)	3.025(22)	3.019	-3.675(31)
6.880	4.901(18)	3.246(22)	3.255	-3.896(18)
6.950	5.249(20)	3.478(23)	3.475	-4.077(40)
7.030	5.668(49)	3.728(26)	3.742	-4.439(47)
7.150	6.275(39)	4.177(31)	4.176	-4.791(37)
7.280	6.991(72)	4.705(26)	4.697	-5.210(89)

Table XVI: Estimates of the scale setting parameters r_0 , r_1 and the additive renormalization constant $c(\beta)$ in the determination of the potential for the HISQ/tree calculations along the $m_l = 0.05m_s$ LCP. See the text for the definition of r_1^{fit}/a and fit details.

calculate τ_{int} reliably requires time series substantially longer than generated in this study, so we provide a rough estimate. We assume that the autocorrelation function is dominated by a single exponential, in which case

$$C(\Delta t) = \exp(-\Delta t/\tau_1). \quad (D3)$$

and

$$\tau_1 = -\frac{\Delta t}{\ln C_{\Delta t}}. \quad (D4)$$

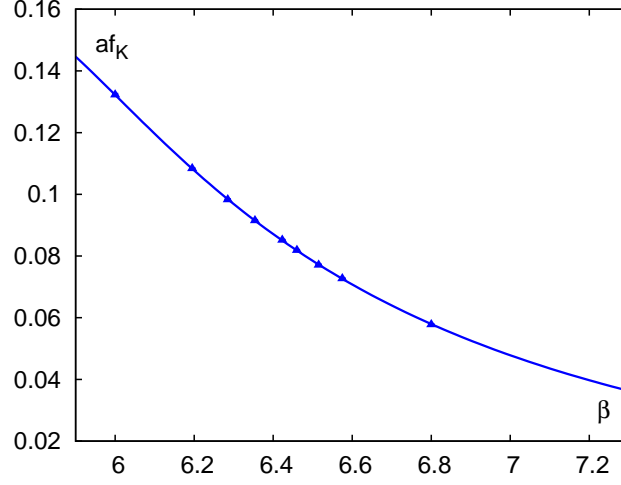


Figure 27: The af_K data together with the smoothing fit for the HISQ/tree action along the LCP defined by $m_l = 0.05m_s$.

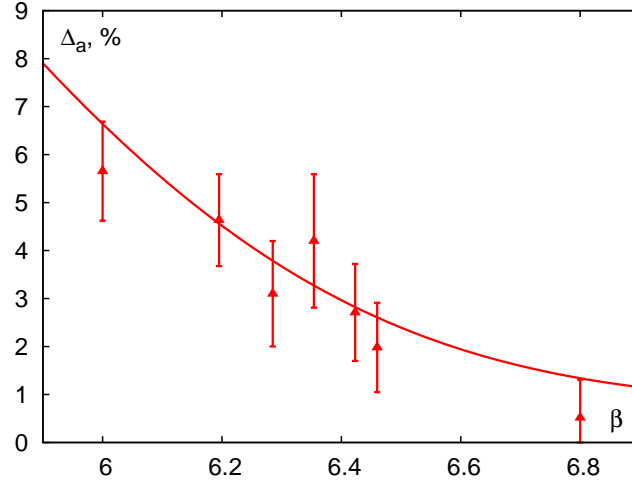


Figure 28: The percentage difference in the lattice spacing determined from r_1 and f_K *vs.* the gauge coupling β for the HISQ/tree action. The line corresponds to the difference calculated from fits to Eqs. (B8) and (B9).

β	aM_π	aM_K	$aM_{\eta_{s\bar{s}}}$
6.000	0.36320(15)	0.61988(19)	0.79730(14)
6.038	0.34838(14)	0.59472(18)	0.76515(15)
6.100	0.32895(16)	0.56187(20)	0.72335(17)
6.167	0.30725(19)	0.52423(23)	0.67508(18)
6.200	0.29711(34)	0.50662(36)	0.65257(32)
6.227	0.28871(21)	0.49280(23)	0.63519(26)
6.256	0.28044(23)	0.47834(26)	0.61653(26)
6.285	0.27332(25)	0.46636(33)	0.60156(33)
6.313	0.26543(26)	0.45313(34)	0.58415(31)
6.341	0.25970(27)	0.44252(31)	0.57037(30)
6.369	0.25313(32)	0.43176(43)	0.55628(35)
6.396	0.24563(32)	0.41907(35)	0.54098(31)
6.450	0.23790(30)	0.40540(50)	0.52240(40)

Table XVII: The pseudoscalar meson masses for the HISQ/tree action along the $m_l = 0.2m_s$ LCP.

β	aM_π	aM_K	$aM_{\eta_{s\bar{s}}}$
5.900	0.20162(09)	0.63407(17)	0.86972(11)
6.000	0.18381(37)	0.57532(51)	0.79046(27)
6.195	0.15143(14)	0.47596(16)	0.65506(11)
6.285	0.13823(50)	0.43501(47)	0.59951(28)
6.354	0.12923(15)	0.40628(20)	0.55982(17)
6.423	0.12022(12)	0.37829(19)	0.52161(17)
6.460	0.11528(21)	0.36272(34)	0.50137(32)
6.488	0.11245(15)	0.35313(27)	0.48716(17)
6.515	0.10975(12)	0.34453(29)	0.47516(29)
6.550	0.10629(16)	0.33322(38)	0.45989(24)
6.575	0.10469(68)	0.32521(55)	0.44869(50)
6.608	0.10001(17)	0.31333(28)	0.43286(29)
6.664	0.09572(18)	0.29837(37)	0.41178(32)
6.800	0.0849(18)	0.26387(99)	0.36257(68)
7.280	0.05399(43)	0.17128(44)	0.23766(30)

Table XVIII: The pseudoscalar meson masses for the HISQ/tree action along the $m_l = 0.05m_s$ LCP.

β	af_π	af_K	$af_{s\bar{s}}$	# sources
6.000	0.11243(21)	0.13224(31)	0.15290(22)	1
6.195	0.09179(21)	0.10835(13)	0.12525(13)	1
6.285	0.08366(22)	0.09826(13)	0.11390(13)	1
6.354	0.07825(40)	0.09146(19)	0.10598(11)	1
6.423	0.07241(18)	0.08515(11)	0.09854(07)	2
6.460	0.06885(11)	0.08185(09)	0.09454(08)	4
6.515	0.06534(18)	0.07707(15)	0.08946(09)	4
6.575	0.06104(49)	0.07265(19)	0.08405(14)	2
6.800	0.04883(83)	0.05774(18)	0.06717(14)	1

Table XIX: Estimates of decay constants of the pseudoscalar mesons in lattice units for the HISQ/tree action along the $m_l = 0.05m_s$ LCP. We use the normalization in which $f_\pi \sim 90$ MeV. In the last column, we list the number of source points used on each configuration to increase the statistics.

β	aM_ρ	aM_{K^*}	aM_ϕ	aM_N
6.000	1.0292(199)	1.1263(82)	1.2363(24)	1.3557(100)
6.038	0.9763(67)	1.0867(40)	1.1907(22)	1.3277(77)
6.100	0.9160(117)	1.0230(34)	1.1211(38)	1.2418(116)
6.167	0.8499(52)	0.9570(41)	1.0491(18)	1.1560(55)
6.200	0.8300(83)	0.9288(48)	1.0133(24)	1.1273(73)
6.227	0.8002(31)	0.9045(37)	0.9907(25)	1.0662(92)
6.256	0.7822(27)	0.8728(48)	0.9548(14)	1.0563(52)
6.285	0.7700(36)	0.8602(33)	0.9386(22)	1.0311(25)
6.313	0.7462(40)	0.8344(35)	0.9089(21)	1.0050(29)
6.341	0.7170(24)	0.8019(30)	0.8780(17)	0.9705(36)
6.369	0.7006(21)	0.7818(23)	0.8572(26)	0.9524(25)
6.396	0.6843(32)	0.7605(20)	0.8311(29)	0.9246(37)
6.450	0.6505(55)	0.7206(43)	0.7962(18)	0.8637(106)

Table XX: The vector meson and the nucleon masses for the HISQ/tree action along the $m_l = 0.2m_s$ LCP.

β	aM_ρ	aM_{K^*}	aM_ϕ	aM_N	aM_Ω
6.000					1.994(13)
6.195	0.7562(36)	0.8842(18)	1.00500(93)	1.0114(56)	1.665(17)
6.285					1.4873(67)
6.354	0.6375(35)	0.7499(26)	0.85234(77)	0.8315(95)	1.374(60)
6.423	0.6047(43)	0.6950(22)	0.79246(83)	0.7899(58)	
6.460	0.578(25)	0.6709(43)	0.7644(22)		
6.488	0.5647(24)	0.6478(22)	0.73630(68)	0.7452(51)	
6.515	0.5452(59)	0.6358(40)	0.7167(10)	0.7247(55)	
6.550	0.5324(24)	0.6118(20)	0.6929(14)	0.7010(90)	
6.608	0.5072(39)	0.57572(84)	0.65227(98)	0.6442(69)	
6.664	0.4732(43)	0.5501(26)	0.6180(10)	0.6048(111)	
6.800					0.8725(42)

Table XXI: Estimates of the vector mesons, the nucleon and the Ω baryon masses in lattice units for the HISQ action along the $m_l = 0.05m_s$ LCP.

The integrated autocorrelation time is then given by

$$\tau_{int} \approx 1 + 2 \sum_{\Delta t=1}^{\infty} \exp(-\Delta t/\tau_1) = 1 + 2 \frac{\exp(-1/\tau_1)}{1 - \exp(-1/\tau_1)} \approx 1 + 2\tau_1. \quad (D5)$$

Our data indicate that Eq. (D3) is a reasonable approximation for the plaquette but not for the chiral condensate and the topological susceptibility. To get a rough estimate of τ_{int} we consider the data for the plaquette given in Table XXII. Estimates of τ_1 vary between 3.4–5.1 and, consequently, for τ_{int} between 7–10. Estimates of τ_{int} for the chiral condensate and the topological susceptibility could be larger due to multiple exponentials contributing long tails even though the $C_{\Delta t}$ are smaller. Based on these rough estimates for the plaquette, we typically save every tenth lattice for further measurements, for example, the quark number susceptibility. We also check for the statistical significance of the data for a given observable by binning to the extent justified by the statistics.

The topological charge Q is calculated on zero-temperature ensembles following the prescription in Ref. [82]. The corresponding time histories are shown in Figs. 29–32. In these figures, the number of TUs examined is set to 1200 (corresponding to the shortest time series at $\beta = 7.280$) to make comparison easier.

β	Δt	\square	$\langle \bar{\psi}\psi \rangle_s$	Q
6.000	5	0.378(42)	0.073(14)	0.361(57)
6.285	5	0.369(29)	0.076(19)	0.262(39)
6.460	5	0.336(28)	0.120(21)	0.397(51)
7.280	6	0.168(34)	0.025(40)	-

Table XXII: Estimates of the autocorrelation coefficient $C_{\Delta t}$ with Δt in TU for a representative set of the HISQ/tree zero-temperature lattices measured using the plaquette, strange quark chiral condensate and the topological charge.

-
- [1] R. Hagedorn, Nuovo Cim. Suppl. **3**, 147 (1965).
 - [2] N. Cabibbo and G. Parisi, Phys. Lett. **B59**, 67 (1975).
 - [3] E. V. Shuryak, Sov. Phys. JETP **47**, 212 (1978).
 - [4] L. D. McLerran and B. Svetitsky, Phys. Rev. **D24**, 450 (1981).
 - [5] J. Kuti, J. Polonyi, and K. Szlachanyi, Phys. Lett. **B98**, 199 (1981).
 - [6] J. Engels, F. Karsch, H. Satz, and I. Montvay, Phys. Lett. **B101**, 89 (1981).
 - [7] J. B. Kogut, M. Stone, H. Wyld, J. Shigemitsu, S. Shenker, et al., Phys. Rev. Lett. **48**, 1140 (1982), revised version.
 - [8] J. B. Kogut, M. Stone, H. Wyld, W. Gibbs, J. Shigemitsu, et al., Phys. Rev. Lett. **50**, 393 (1983).
 - [9] R. D. Pisarski and F. Wilczek, Phys. Rev. **D29**, 338 (1984).
 - [10] C. Bernard et al. (MILC Collaboration), Phys. Rev. **D71**, 034504 (2005), hep-lat/0405029.
 - [11] M. Cheng, N. Christ, S. Datta, J. van der Heide, C. Jung, et al., Phys. Rev. **D74**, 054507 (2006), hep-lat/0608013.

	$N_\tau = 6$			$N_\tau = 8$			$N_\tau = 12$		
β	\square	$\langle\bar{\psi}\psi\rangle_l$	$\langle\bar{\psi}\psi\rangle_s$	\square	$\langle\bar{\psi}\psi\rangle_l$	$\langle\bar{\psi}\psi\rangle_s$	\square	$\langle\bar{\psi}\psi\rangle_l$	$\langle\bar{\psi}\psi\rangle_s$
6.000	0.172(18)	0.119(14)	0.219(22)	—	—	—	—	—	—
6.100	0.158(09)	0.219(06)	0.270(11)	—	—	—	—	—	—
6.195	0.121(16)	0.313(29)	0.371(23)	0.156(19)	0.096(18)	0.226(29)	—	—	—
6.285	—	—	—	0.116(09)	0.163(12)	0.218(15)	—	—	—
6.354	0.085(12)	0.068(18)	0.295(39)	0.168(34)	0.262(33)	0.328(29)	—	—	—
6.460	—	—	—	0.155(09)	0.353(21)	0.413(30)	—	—	—
6.550	0.129(16)	N/A	0.172(21)	0.108(17)	0.238(37)	0.413(36)	—	—	—
6.664	—	—	—	0.132(29)	0.078(20)	0.337(32)	0.117(37)	0.285(34)	0.342(42)
6.800	0.027(17)	N/A	N/A	0.117(13)	0.043(10)	0.209(10)	0.091(22)	0.392(46)	0.298(42)
6.950	—	—	—	0.063(28)	N/A	0.085(14)	0.121(12)	0.355(31)	0.385(41)
7.030	—	—	—	—	—	—	0.116(21)	0.278(32)	0.292(34)
7.150	—	—	—	—	—	—	0.091(04)	0.132(29)	0.177(15)

Table XXIII: Estimates of the autocorrelation coefficient $C_{\Delta t}$ with $\Delta t = 10$ for a representative set of HISQ/tree finite temperature lattices measured using the plaquette, and the light and strange quark chiral condensates. The correlations decrease away from the transition region, therefore in some cases, we were unable to extract the autocorrelation coefficient. Note that the chiral condensate is calculated with stochastic estimators that introduce additional noise in the correlation function.

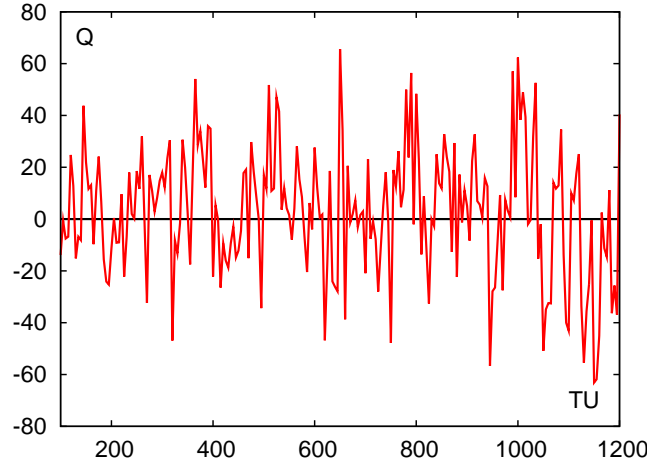


Figure 29: Time history of the topological charge measured every 5 time units on $24^3 \times 32$ configurations at $\beta = 6.000$ with the HISQ/tree action.

- [12] Y. Aoki, G. Endrodi, Z. Fodor, S. Katz, and K. Szabo, Nature **443**, 675 (2006), hep-lat/0611014.
- [13] P. Braun-Munzinger, K. Redlich, and J. Stachel (2003), to appear in Quark Gluon Plasma 3, eds. R.C. Hwa and Xin-Nian Wang, World Scientific Publishing, nucl-th/0304013.
- [14] S. Ejiri et al. (WHOT-QCD Collaboration), Phys. Rev. **D82**, 014508 (2010), 0909.2121.
- [15] V. Bornyakov, R. Horsley, S. Morozov, Y. Nakamura, M. Polikarpov, et al., Phys. Rev. **D82**, 014504 (2010), 0910.2392.
- [16] M. Cheng, N. H. Christ, M. Li, R. D. Mawhinney, D. Renfrew, et al., Phys. Rev. **D81**, 054510 (2010), 0911.3450.
- [17] Y. Aoki, Z. Fodor, S. Katz, and K. Szabo, JHEP **0601**, 089 (2006), hep-lat/0510084.
- [18] C. Bernard, T. Burch, C. E. DeTar, S. Gottlieb, L. Levkova, et al., Phys. Rev. **D75**, 094505 (2007), hep-lat/0611031.
- [19] M. Cheng, N. Christ, S. Datta, J. van der Heide, C. Jung, et al., Phys. Rev. **D77**, 014511 (2008), 0710.0354.
- [20] A. Bazavov, T. Bhattacharya, M. Cheng, N. Christ, C. DeTar, et al., Phys. Rev. **D80**, 014504 (2009), 0903.4379.
- [21] M. Cheng, S. Ejiri, P. Hegde, F. Karsch, O. Kaczmarek, et al., Phys. Rev. **D81**, 054504 (2010), 0911.2215.
- [22] Y. Aoki, Z. Fodor, S. Katz, and K. Szabo, Phys. Lett. **B643**, 46 (2006), hep-lat/0609068.
- [23] Y. Aoki, S. Borsanyi, S. Durr, Z. Fodor, S. D. Katz, et al., JHEP **0906**, 088 (2009), 0903.4155.
- [24] S. Borsanyi et al. (Wuppertal-Budapest Collaboration), JHEP **1009**, 073 (2010), 1005.3508.
- [25] E. Follana et al. (HPQCD Collaboration, UKQCD Collaboration), Phys. Rev. **D75**, 054502 (2007), hep-lat/0610092.
- [26] C. E. Detar and R. Gupta (HotQCD Collaboration), PoS **LAT2007**, 179 (2007), 0710.1655.

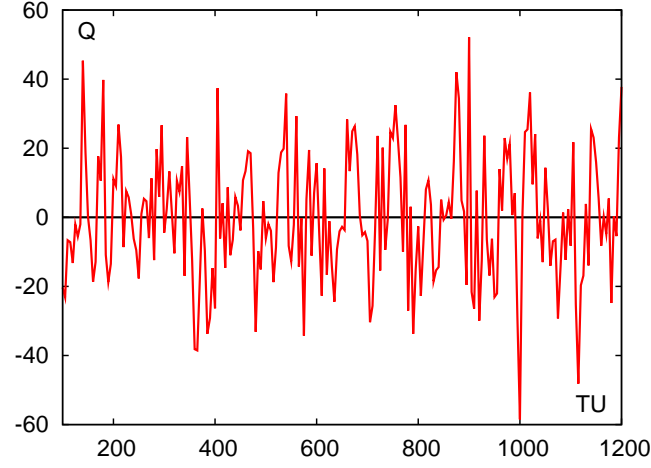


Figure 30: Time history of the topological charge measured every 5 time units on 32^4 configurations at $\beta = 6.285$ with the HISQ/tree action.

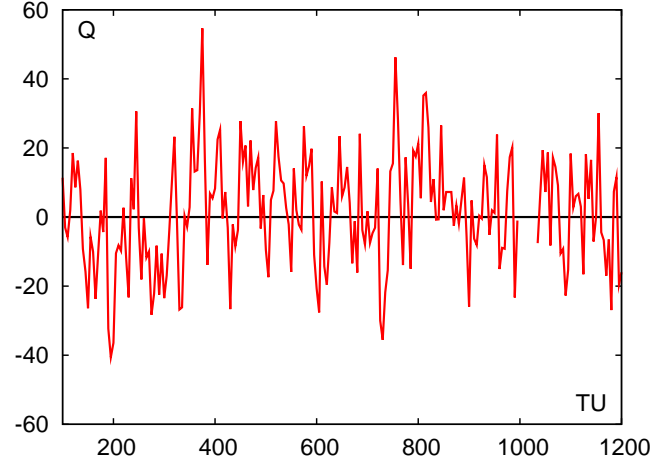


Figure 31: Time history of the topological charge measured every 5 time units on $32^3 \times 64$ configurations on $\beta = 6.460$ with the HISQ/tree action.

- [27] R. Gupta (HotQCD) (2009), 0912.1374.
- [28] A. Bazavov and P. Petreczky (HotQCD Collaboration), PoS **LAT2009**, 163 (2009), 0912.5421.
- [29] A. Bazavov and P. Petreczky (HotQCD collaboration), J.Phys.Conf.Ser. **230**, 012014 (2010), 1005.1131.
- [30] A. Bazavov and P. Petreczky (HotQCD Collaboration) (2010), 1009.4914.
- [31] W. Soldner (HotQCD collaboration), PoS **LATTICE2010**, 215 (2010), 1012.4484.
- [32] A. Bazavov and P. Petreczky (for the HotQCD Collaboration), PoS **LATTICE2010**, 169 (2010), 1012.1257.
- [33] A. Bazavov and P. Petreczky (HotQCD Collaboration) (2011), 1107.5027.
- [34] A. Bazavov and P. Petreczky (2011), * Temporary entry *, 1110.2160.
- [35] F. Karsch, K. Redlich, and A. Tawfik, Eur. Phys. J. **C29**, 549 (2003), dedicated to Rolf Hagedorn, hep-ph/0303108.
- [36] P. Huovinen and P. Petreczky, Nucl. Phys. **A837**, 26 (2010), 0912.2541.
- [37] P. Huovinen and P. Petreczky, J.Phys.Conf.Ser. **230**, 012012 (2010), 1005.0324.
- [38] P. Huovinen and P. Petreczky, J.Phys.G **G38**, 124103 (2011), 1106.6227.
- [39] T. Blum, C. E. Detar, S. A. Gottlieb, K. Rummukainen, U. M. Heller, et al., Phys. Rev. **D55**, 1133 (1997), hep-lat/9609036.
- [40] K. Orginos, D. Toussaint, and R. Sugar (MILC Collaboration), Phys. Rev. **D60**, 054503 (1999), hep-lat/9903032.
- [41] A. Bazavov, D. Toussaint, C. Bernard, J. Laiho, C. DeTar, et al., Rev. Mod. Phys. **82**, 1349 (2010), 0903.3598.
- [42] A. Hasenfratz and F. Knechtli, Phys. Rev. **D64**, 034504 (2001), hep-lat/0103029.
- [43] A. Hasenfratz, Nucl. Phys. Proc. Suppl. **119**, 131 (2003), hep-lat/0211007.
- [44] A. Hasenfratz, R. Hoffmann, and S. Schaefer, JHEP **0705**, 029 (2007), hep-lat/0702028.
- [45] A. Bazavov et al. (MILC Collaboration), PoS **LAT2009**, 123 (2009), 0911.0869.

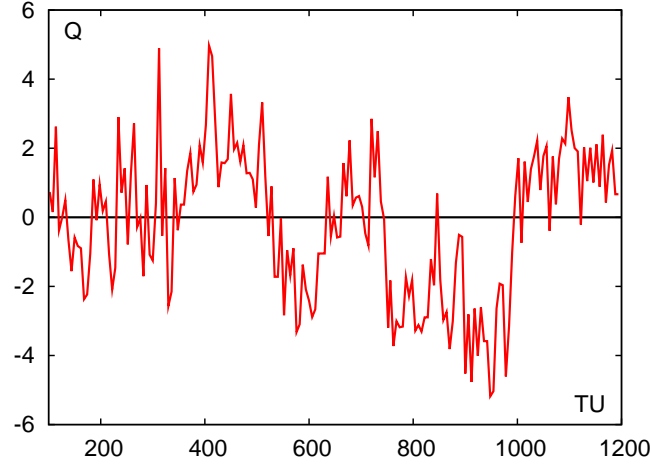


Figure 32: Time history of the topological charge measured every 6 time units on $48^3 \times 64$ configurations at $\beta = 7.280$ with the HISQ/tree action.

- [46] A. Bazavov et al. (MILC collaboration), Phys. Rev. **D82**, 074501 (2010), 1004.0342.
- [47] S. R. Sharpe, PoS **LAT2006**, 022 (2006), hep-lat/0610094.
- [48] M. Creutz, PoS **LAT2007**, 007 (2007), 0708.1295.
- [49] U. M. Heller, F. Karsch, and B. Sturmfels, Phys. Rev. **D60**, 114502 (1999), hep-lat/9901010.
- [50] P. Hegde, F. Karsch, E. Laermann, and S. Shcheredin, Eur. Phys. J. **C55**, 423 (2008), 0801.4883.
- [51] M. Clark, A. Kennedy, and Z. Sroczynski, Nucl. Phys. Proc. Suppl. **140**, 835 (2005), hep-lat/0409133.
- [52] M. Clark, P. de Forcrand, and A. Kennedy, PoS **LAT2005**, 115 (2006), hep-lat/0510004.
- [53] A. Bazavov et al. (MILC Collaboration), PoS **LATTICE2008**, 033 (2008), 0903.0874.
- [54] R. Sommer, Nucl. Phys. **B411**, 839 (1994), hep-lat/9310022.
- [55] C. Aubin, C. Bernard, C. DeTar, J. Osborn, S. Gottlieb, et al., Phys. Rev. **D70**, 094505 (2004), hep-lat/0402030.
- [56] S. Necco and R. Sommer, Nucl. Phys. **B622**, 328 (2002), hep-lat/0108008.
- [57] D. Toussaint, private communications.
- [58] A. Bazavov et al. (MILC Collaboration), PoS **LATTICE2010**, 074 (2010), 1012.0868.
- [59] C. Davies, E. Follana, I. Kendall, G. Lepage, and C. McNeile (HPQCD Collaboration), Phys. Rev. **D81**, 034506 (2010), 0910.1229.
- [60] A. Gray, I. Allison, C. Davies, E. Dalgic, G. Lepage, et al., Phys. Rev. **D72**, 094507 (2005), hep-lat/0507013.
- [61] C. W. Bernard, T. Burch, K. Orginos, D. Toussaint, T. A. DeGrand, et al., Phys. Rev. **D64**, 054506 (2001), hep-lat/0104002.
- [62] W.-J. Lee and S. R. Sharpe, Phys. Rev. **D60**, 114503 (1999), hep-lat/9905023.
- [63] M. Cheng, N. Christ, C. Jung, F. Karsch, R. Mawhinney, et al., Eur. Phys. J. **C51**, 875 (2007), hep-lat/0612030.
- [64] S. Ejiri, F. Karsch, E. Laermann, C. Miao, S. Mukherjee, et al., Phys. Rev. **D80**, 094505 (2009), 0909.5122.
- [65] J. Engels, S. Holtmann, T. Mendes, and T. Schulze, Phys. Lett. **B492**, 219 (2000), hep-lat/0006023.
- [66] D. Toussaint, Phys. Rev. **D55**, 362 (1997), hep-lat/9607084.
- [67] J. Engels and T. Mendes, Nucl. Phys. **B572**, 289 (2000), hep-lat/9911028.
- [68] J. Engels, S. Holtmann, T. Mendes, and T. Schulze, Phys. Lett. **B514**, 299 (2001), hep-lat/0105028.
- [69] O. Kaczmarek, F. Karsch, E. Laermann, C. Miao, S. Mukherjee, et al., Phys. Rev. **D83**, 014504 (2011), 1011.3130.
- [70] A. Cucchieri, J. Engels, S. Holtmann, T. Mendes, and T. Schulze, J. Phys. **A35**, 6517 (2002), cond-mat/0202017.
- [71] D. Wallace and R. Zia, Phys. Rev. **B12**, 5340 (1975).
- [72] P. Hasenfratz and H. Leutwyler, Nucl. Phys. **B343**, 241 (1990).
- [73] A. V. Smilga and J. Stern, Phys. Lett. **B318**, 531 (1993).
- [74] A. V. Smilga and J. Verbaarschot, Phys. Rev. **D54**, 1087 (1996), hep-ph/9511471.
- [75] M. Cheng, S. Datta, A. Francis, J. van der Heide, C. Jung, et al., Eur. Phys. J. **C71**, 1564 (2011), 1010.1216.
- [76] RBC-Bielefeld Collaboration work in progress.
- [77] O. Kaczmarek, F. Karsch, P. Petreczky, and F. Zantow, Phys. Lett. **B543**, 41 (2002), hep-lat/0207002.
- [78] S. Digal, S. Fortunato, and P. Petreczky, Phys. Rev. **D68**, 034008 (2003), hep-lat/0304017.
- [79] O. Kaczmarek and F. Zantow, Phys. Rev. **D71**, 114510 (2005), hep-lat/0503017.
- [80] P. Petreczky and K. Petrov, Phys. Rev. **D70**, 054503 (2004), hep-lat/0405009.
- [81] C. Bernard, C. E. DeTar, L. Levkova, S. Gottlieb, U. Heller, et al., PoS **LAT2007**, 090 (2007), 0710.1118.
- [82] A. Bazavov et al. (MILC collaboration), Phys. Rev. **D81**, 114501 (2010), 1003.5695.